Design and Testing of a Miniaturized Photon Counting Laser Altimeter for Topographic Mapping

Vincent Affatato

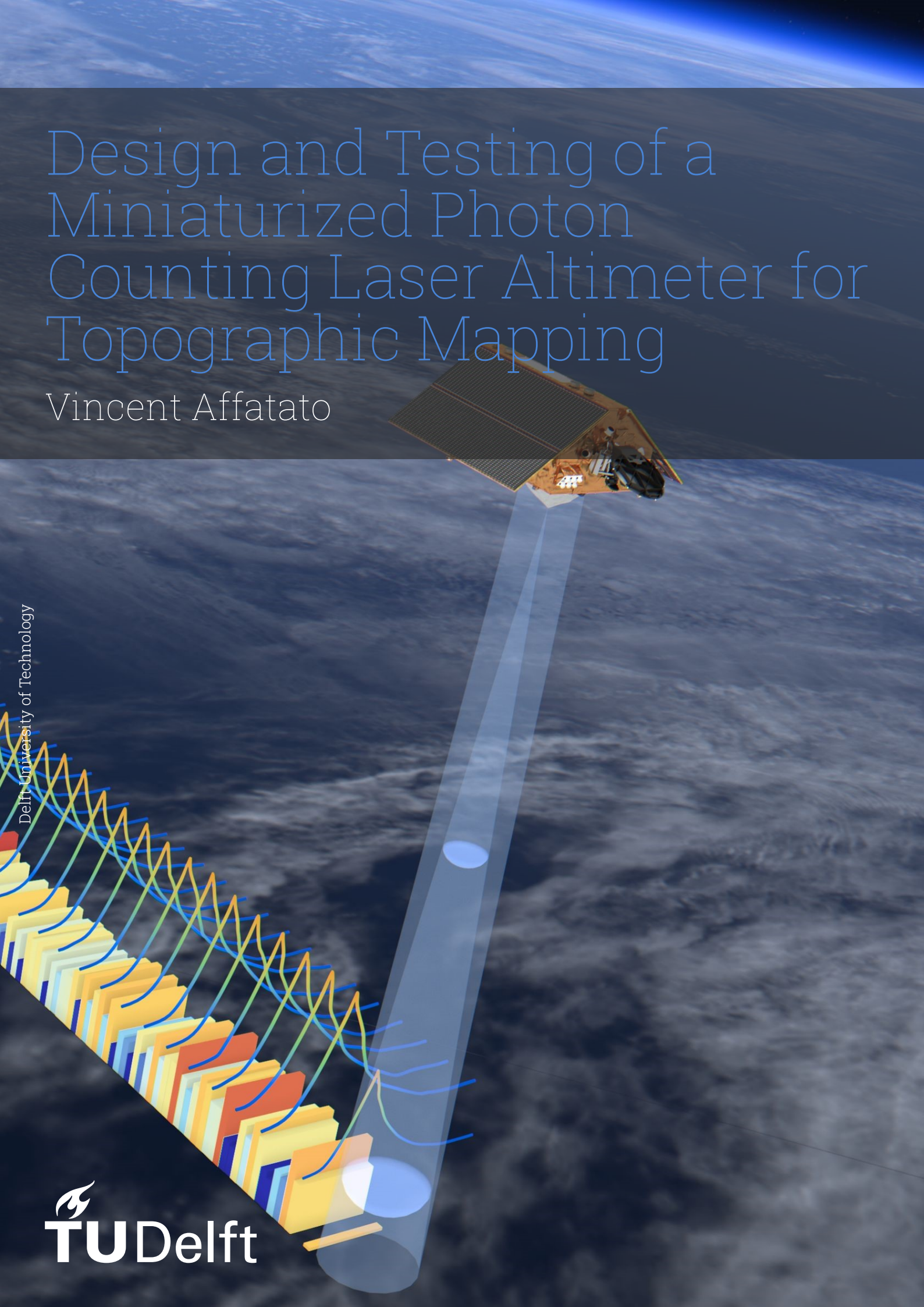

Delft University of Technology

TU Delft

Design and Testing of a Miniaturized Photon Counting Laser Altimeter for Topographic Mapping

by

Vincent Affatato

to obtain the degree of Master of Science
at the Delft University of Technology,
to be defended publicly on Monday October 15th, 2024 at 8:45.

Student number:	5692687	
Project duration:	January 8, 2024 – September 30, 2024	
Thesis committee:	Dr. ir. R. Saathof,	TU Delft, Supervisor
	Dr. S.J.M. Potin,	TU Delft, Supervisor
	Dr. M. Grott ,	DLR Institute of Planetary Research, Supervisor
	Dipl.-Ing. C. Althaus,	DLR Institute of Planetary Research, Supervisor
	Dr. J.J.D. Loicq,	TU Delft, Chair
	M.S. Uludag,	TU Delft, External Member

Cover:	Artistic representation of the Sentinel-6 satellite by ESA
Style:	TU Delft Report Style, with modifications by Daan Zwaneveld

An electronic version of this thesis is available at http://repository.tudelft.nl/.

TU Delft

Acknowledgement

In this space, I should use a few words to thank all those who contributed to completing this thesis. Although the project lasted nine months, I believe it all started two years ago, when my arrival in Delft turned my life upside down. I met mentors, students, and friends who accompanied me through a challenging yet stimulating journey unlike anything before. There were many difficult moments, but the awareness that I never had to face them alone is something I will always hold dear. For the first time, I witnessed the kind of collaboration that fascinates me so much about humanity's race to space. In facing a challenge so far beyond our reach, we set aside (almost) all the grudges that belong to this world and immerse ourselves in an unparalleled spirit of brotherhood. I am proud of the future colleagues I've met, and I'm sure there will be many more opportunities to share these moments.

At the same time, nothing would have been the same without the constant presence of those who have always been in my life: my family and friends in Italy, who, despite the distance and the commitments of our hectic lives, always made time for a call, a message, or a trip to show their support to me. Knowing I always had a solid rock to lean on was sometimes the only motivation to give my best in every moment, and I will forever be grateful to you all for being so present in my life. I hope you're at least a little as proud of me as I am of you.

Finally, I cannot fail to mention all those who made this past year unforgettable: my supervisors at DLR for placing enormous trust in me, even though I had to Google 'oscilloscope' on my first day in the lab; my supervisors in Delft for their constant and impeccable remote support throughout a long and winding project; and all the people I met around the world for the countless moments of inspiration and mutual support.

Thanks to all of this, I can see a bright future ahead of me, and I am happier than ever to dedicate myself entirely to advancing this species of bipedal apes towards new horizons of the universe. I've learned how incredibly fortunate I am to have had you and this opportunity in my life, and for this reason, I face every moment with a huge smile on my face, sharing with everyone just how wonderful it is to be a space engineer.

Vincent Affatato
Delft, September 2024

Executive Summary

Since their first use during the Apollo 15, 16, and 17 missions, laser altimeters have become indispensable for planetary exploration, enabling topographic mapping of rocky bodies throughout the solar system. The latest European contributions in this field are represented by the BepiColombo Laser Altimeter (BELA) and the Ganymede Laser Altimeter (GALA), developed by the DLR Institute of Planetary Research and currently en route to Mercury and the Jovian moons, respectively. However, to date, such instruments have only been deployed on large satellites, failing to meet the SWaP (Size, Weight, and Power) requirements of miniaturized systems.

This thesis investigates the adaptation of laser altimeter technology for smaller platforms, focusing on the NLA (New Laser Altimeter) developed for the SER3NE (Selene's Explorer for Roughness, Regolith, Resources, Neutrons, and Elements) mission proposal. The instrument aims to improve the precision of Lunar topographic data to support the characterization of future landing sites for crewed missions from a 12 U microsatellite. To meet the stringent SWaP constraints, the design will feature a transceiver and a single-photon detection system — an approach never previously applied to topographic altimeters.

This thesis aims to develop an optical design that fits the instrument within a 3 U volume. Given the innovative nature of the design, a trade-off analysis was conducted to evaluate several configurations based on their compactness, cross-coupling between the laser source and detector, footprint size at the target, co-alignment between the transmitter and receiver, and transmission losses. The selected design stood out in providing a footprint size in the range allowed by the requirements, reducing the probability of damage to the detector due to internal reflections from the laser, and guaranteeing a more stable co-alignment between the transmitter and receiver paths. It includes a transmitter with two 45° folding mirrors, a borehole mirror that allows the laser to pass while deflecting the returning signal, and a shared telescope.

A test campaign is then conducted on a dedicated optomechanical design to assess 1) its compliance with some trade-off criteria and 2) its functionality. The expansion performance is demonstrated as predictable and reliable, guaranteeing the desired divergence and footprint at the target. On the other hand, the transmittance is increased above the constraints by varying the angle of incidence of the light on the band-pass filter. For the functional tests, the quality of the wavefront is first evaluated, resulting in an aberration-free transmitter and a slightly worse receiver, but still acceptable for altimetry applications. Finally, the prototype is aligned thoroughly and tested for timing measurements with single-pixel detectors, successfully providing the range to the target.

In the next instrument development phase, throughout the pre-phase A studies in collaboration with ESA (European Space Agency) and relevant companies, the prototype will be enhanced to verify the performance in the other criteria and test its functionality in a relevant environment with a flight campaign.

Contents

List of Figures

List of Tables

Nomenclature

Abbreviations

ALADIN	Atmospheric LAser Doppler Instrument
AOI	Angle of Incidence
APD	Avalanche Photo Diode
ATLAS	Advanced Topographic Laser Altimeter System
AWSL	Adaptive Wavelength Scanning LiDAR
BELA	BepiColombo Laser Altimeter
CAD	Computer-Aided Design
CATIA	Computer-Aided Three-dimensional Interactive Application
CHEOPS	CHaracterising ExOPlanet Satellite
CMOS	Complementary Metal Oxide Semiconductor
CNC	Computer Numerical Control
COTS	Commercial Off-The-Shelf
CubeISL	Cube Inter-Satellite Link
CubeLST	Cube Laser Communication Terminal
CWL	Central Wavelength
DLR	Deutsches Zentrum für Luft- und Raumfahrt
ESA	European Space Agency
FoV	Field of View
FPGA	Field-Programmable Gate Array
FWHM	Full Width at Half Maximum
GALA	Ganymede Laser Altimeter
GLAS	Geoscience Laser Altimeter System
Gm	Geiger mode
GUI	Graphical User Interface
H	Lens Principal Plane
ICESat	Ice, Cloud, and land Elevation Satellite
IMS	Institute for Microelectronic Circuits and Systems
JUICE	Jupiter Icy Moons Explorer
LASER	Light Amplification by Stimulated Emission of Radiation
LALT	Laser ALTimeter (Kaguya mission)
LiDAR	Light Detection And Ranging
LLRI	Lunar Laser Ranging Instrument
LOLA	Lunar Orbiter Laser Altimeter
MGS	Mars Global Surveyor
MLA	Mercury Laser Altimeter
MOLA	Mars Orbiter Laser Altimeter
MTT	Main Telescope Tube
NASA	National Aeronautics and Space Administration
NEAR	Near Earth Asteroids Rendezvous
NLA	New Laser Altimeter
NLR	NEAR Laser Rangefinder
OLA	OSIRIS-REx Laser Altimeter
OSIP	Open Space Innovation Platform
OSIRIS-REx	Origins Spectral Interpretation Resource Identification Security-Regolith Explorer
PALT	Planetary ALTimeter
PCB	Printed Circuit Board
PCM	Power Converter Module
RMS	Root-Mean Square
RT	Receiver Tube
Rx	Receiver
SER3NE	Selene's Explorer for Roughness, Regolith, Resources, Neutrons and Elements
SNR	Signal-to-Noise Ratio
SPAD	Single Photon Avalanche Diode
SWaP / SWP	Size, Weight, and Power
TB	Transceiver Box
TEM	Transverse Electromagnetic Mode
TOF	Time Of Flight
TRL	Technology Readiness Level
Tx	Transmitter
U	CubeSat Unit

Latin Symbols

ad_T	Receiver aperture diameter [m]
c	Speed of light [m/s^2]
d	Lens Glass Substrate Thickness [m]
d_σ	Beam Section Diameter [m]
$D4\sigma$	Standardised Beam Section Diameter [m]
f	focal length [m]
E	Energy of a photon [J]
E_R	Received laser pulse energy [J]
E_T	Emitted laser pulse energy [J]
h	Planck's constant [J · s]
H	Range [m]
I	Intensity of laser beam [W/m^2]
m	Magnification [-]
M^2	Propagation constant [-]
M	Mass [kg]
n	Refractive Index [-]
P_P	Laser Peak Power [W]
Q_e	Quantum efficiency [-]
R	Radius of curvature of a laser beam [m]
R_R	Radius of curvature of a real laser beam [m]
s	Object Distance [m]
s''	Image Distance [m]
S	Strehl Ratio [-]
t	Time [s]
t_p	Pulse duration at FWHM [s]
T_a	Atmospheric attenuation loss fraction [-]
V	Voltage [V]
V_A	Bias Supply Voltage [V]
V_B	Breakdown Voltage [V]
V_E	Excess Bias Voltage [V]
w	Beam Radius [m]
w_0	Initial Beam Waist Radius [m]
w_{0R}	Initial Beam Waist Radius for real laser [m]
w_R	Beam Radius for real laser [m]
X	Conversion Factor for Expanding Beams [-]
z	Propagation range of a laser beam [m]
z_R	Rayleigh range [m]
z_{RR}	Rayleigh range for real laser [m]

Greek Symbols

ζ_P	Power factor [-]
ζ_S	Size Factor [m/kg]
θ	Divergence [rad]
θ_R	Divergence for real laser [rad]
λ	Wavelength [m]
ξ_R	Transmittance loss in receiver optics [-]
ξ_T	Transmittance loss in transmitter optics [-]
τ	Transmittance through lens glass substrate [-]
ϕ	Angle of Incidence of the light [deg]
ω	RMS Wavefront Error [-]

1

Introduction

Laser altimetry has been a fruitful expedient for space applications in the past decades, becoming an essential payload on almost every flown spacecraft [1] [2]. The reasons for this success lay in the relative simplicity of their working principle and the flexibility of such instruments in fitting diverse applications. Indeed, by exposing a defined target with a laser pulse, a laser altimeter permits measuring the time of flight of the returning signals and, consequently, calculating the distance of the spacecraft from which the pulse was emitted.

This simple principle permitted Apollo 15, 16, and 17 missions to fulfil an essential mission requirement. For the first time, it was possible to monitor the spacecraft's distance from the Lunar ground during the descent phases [2]. Moreover, the measured data, combined with information about gravity and moment of inertia, were immediately exploited by scholars to produce scientific models about the interior structure of the Moon, constraining parameters such as mean radius, mean density, and core dimensions [3]. Since then, the use of laser altimeters in space has grown and branched into various purposes.

Inheriting the achievements of the Apollo program, many altimeters have been launched to scan the topographical features of planetary bodies. Keeping the focus on the Moon, the first instrument to provide a global map of the surface was the Clementine Light Detection And Ranging (LiDAR) [1994] [4], followed by the Laser ALTimeter (LALT) on the Kaguya mission [2007] [5], the Lunar Laser Ranging

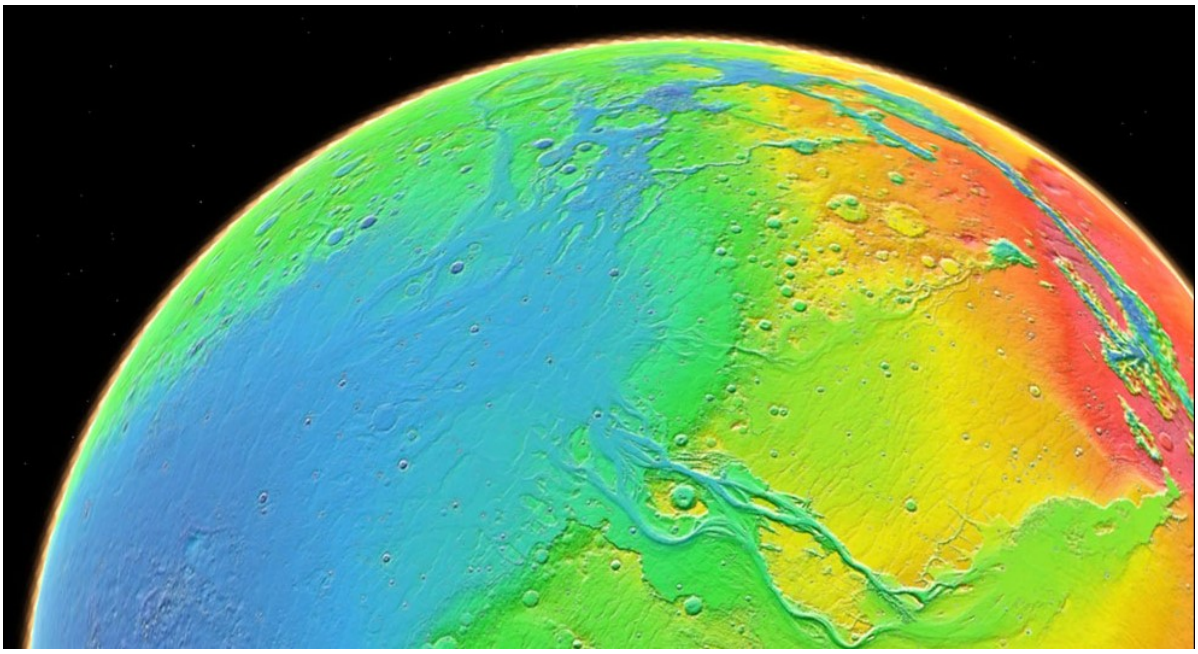

Figure 1.1: Detail of a topographic map of Mars created thanks to the data from MOLA [6].

Instrument (LLRI) [2008] [7], and the Lunar Orbiter Laser Altimeter (LOLA) [2009] [8]. The latter is still in operation and represents the last endeavour to enhance the precision of ranging measurement of the lunar surface. By implementing a Diffractive Optical Element (DOE), the instrument splits its laser beam into five independent spots that are singularly evaluated to ensure a high precision level while providing extensive along and cross-track coverage to permit the characterisation of safe future landing sites. Nevertheless, technological developments have pushed the boundaries of space exploration, providing the capability to reach other rocky planets. Mercury, for example, has been investigated by the Mercury Laser Altimeter (MLA) [2004] [9] and will soon be the target of the BepiColombo Laser Altimeter (BELA) [2018] [10], the first long-range laser altimeter for interplanetary flight developed in Europe. Other missions have reached Mars, like the Mars Global Surveyor (MGS) with the Mars Orbiter Laser Altimeter (MOLA) [1996] [11], still now the reference point for the topography of the red planet (Figure 1.1). Recently, the increasing interest in icy moons and their supposed capability to host life conditions have driven the commitment to reach the Jovian system with the Jupiter Icy Moons Explorer (JUICE), carrying the Ganymede Laser Altimeter (GALA) [2023] [12].

At the same time, the interest in small bodies as primordial leftovers of the Solar System has rapidly grown. Coherently, laser altimeter design started to morph toward more complex applications, still involving mapping but also including navigation and landing on the surface of asteroids, sometimes for sample return purposes. The achievements in this sense have been enormous, starting with the Near Earth Asteroids Rendezvous (NEAR) Laser Rangefinder (NLR) [1996] [13] that explored and landed on the asteroid Eros. The HAYABUSA 1 LiDAR [2003] [14] [2] to Itokawa and the HAYABUSA 2 LiDAR [2014] [15] to Ryugu asteroids were the first altimeters contributing to successfully bringing back samples to Earth, followed by the Origins, Spectral Interpretation, Resource Identification, Security-Regolith Explorer (OSIRIS-REx) Laser Altimeter (OLA) [2016] [16] to asteroid Bennu. Lastly, the Planetary Altimeter (PALT) [planned 2025] [17] on board the European Space Agency (ESA) mission HERA will study, for the first time, the effect of a planetary defence mission on the trajectory and shape of the asteroid Didymos.

However, in other cases, laser altimeters didn't need to reach remote bodies of the solar system to demonstrate themselves as a powerful tool for Earth observation, helping to monitor glaciers, vegetation, clouds, and winds. They evolved from airborne applications, such as uncovering archaeological remnants of past civilisations (Figure 1.2), to global monitoring of ice sheets, fires, and relevant events related to climate changes with the Geoscience Laser Altimeter System (GLAS) [2003] [18] and the Advanced Topographic Laser Altimeter System (ATLAS) [2018] [19] from the Ice, Cloud, and land Elevation Satellites (ICESat-1 and 2). With the same goal but aimed at studying wind evolution for climate models, the Atmospheric LAser Doppler Instrument (ALADIN) [2018] [20] on board the ESA Aeolus mission has provided invaluable insight into the ecosystem of the Earth for the past five years.

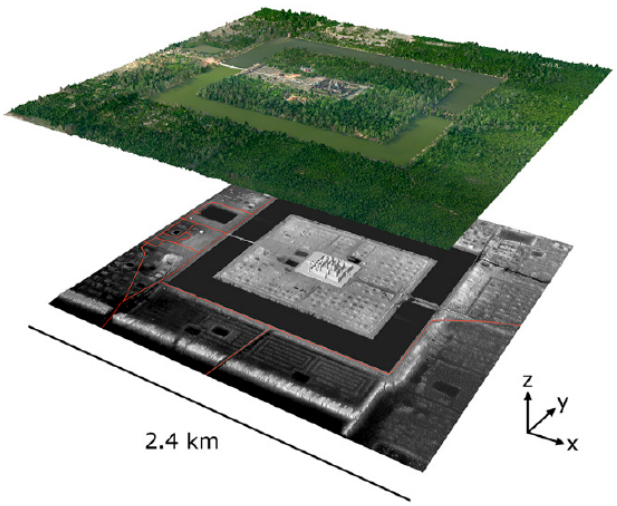

Figure 1.2: LiDAR data (on the bottom) of the Angkor archaeological site in Cambodia that helped in the discovery of urban sites underneath the vegetation (on the top) [21].

This list is far from an exhaustive overview of the development of spaceborne laser altimeters. Still, it represents some of the benchmarks that have contributed to the development of this technology over the past decades. It is possible to see a variegated scenario: these instruments differentiated their scopes, reaching distant bodies or orbiting the Earth closely, specialising in particular applications or supporting different operations simultaneously. Tables 1.1, 1.2, and 1.3 provide a summary of the technical specifics of some of those missions, the ones that were considered more relevant for this project for their application, detection techniques, dimensions, and heritage. All the presented figures of merit will be introduced in the thesis and will help to understand the working principles of altimeters better.

While laser altimeters have been unveiling precious information about the primordial ages of our cosmic neighbourhood, the internal processes of other rocky planets, and daily changes in the ecosystem of the Earth, space technology has started exploring new frontiers. Many private companies have developed innovative space launchers, making the market more competitive for smaller satellites [22]. This trend, also visible in the number of small satellites launched in the past ten years (Figure 1.3), shows that the trust in this new miniaturisation level is exponentially growing and will be the main focus for the following years of space utilisation.

Table 1.1: Summary table for the main characteristics of the studied laser altimeters for Earth observation. For the GLAS instrument, the information comes from the atmospheric observation measurements. The pulse energy of the ATLAS instrument presents two values because the six generated laser beams had two different intensities [23].

Characteristics		**GLAS**	**ATLAS**
Laser Specifications	N. of beams	1 [2]	6 [2]
	Wavelength [nm]	532 [23]	532 [2]
	Pulse Energy [mJ]	35 [18]	0.25-0.9 [23]
	Divergence [μrad]	110 [18]	20 [23]
	Vertical Accuracy [cm]	5 [18]	*
	Repetition Rate [Hz]	40 [2]	10000 [2]
Telescope Diameter [m]		1 [23]	0.8 [23]
Mass [kg]		298 [24]	470 [23]
Temperature Range (nom/surv) [°C]		+10 to + 35 0 to +50 [18]	*
Orbit [km]		600 [24]	500 [25]
Power Consumption [W]		330 [24]	420 [23]

Table 1.2: Summary table for the main characteristics of the studied laser altimeters for topographic mapping.

Characteristics		**BELA**	**GALA**	**LOLA**	**LALT**
Laser Specifications	N. of beams	1 [2]	1 [2]	5 [2]	1 [2]
	Wavelength [nm]	1064 [2]	1064 [26]	1064 [2]	1064 [2]
	Pulse Energy [mJ]	50 [1]	17 [1]	2.7 [2]	100 [2]
	Divergence [μrad]	200 [2]	100 [27]	100 [2]	400 [2]
	Vertical Accuracy [cm]	10 to 30 [28]	10 [26]	9 [29]	400 [30]
	Repetition Rate [Hz]	10 [1]	30 [26]	28 [2]	1 [2]
Telescope Diameter [m]		0.2 [1]	0.25 [26]	0.14 [29]	0.1 [31]
Mass [kg]		15 [1]	25 [1]	12.6 [29]	20 [5]
Temperature Range (nom/surv) [°C]		-20 to +65 [28]	-25 to +50 -35 to +65 [32]	+5 to +28 -20 to +40 [33]	*
Orbit [km]		400 to 1000 [1]	500 [1]	50 [29]	100 [30]
Power Consumption [W]		43 [28]	50 [1]	34 [29]	44 [34]

Table 1.3: Summary table for the main characteristics of the studied laser altimeters for navigation and landing.

Characteristics		HAYA 1	HAYA 2	OLA	PALT
Laser Specifications	N. of beams	1 [14]	1 [2]	1 [2]	1 [2]
	Wavelength [nm]	1064 [14]	1064 [2]	1064 [2]	1535 [35]
	Pulse Energy [mJ]	10 [14]	15 [2]	0.01-0.07 [16]	0.1 [35]
	Divergence [μrad]	1700 [14]	2400 [2]	100-200 [16]	1100 [35]
	Vertical Accuracy [cm]	1000 [14]	550 [15]	6-31 [16]	50 [35]
	Repetition Rate [Hz]	1 [14]	1 [15][2]	10000-100 [16]	10 [36]
Telescope Diameter [m]		0.126 [14]	0.11 [15]	0.075 [16]	0.1 [37]
Mass [kg]		3.7 [14]	3.5 [15]	21.4 [16]	4.92 [35]
Temperature Range (nom/surv) [°C]		*	+10 to +40 -30 to +60 [15]	*	-40 to + 60 [36]
Orbit [km]		0.5 to 50 [14]	0.03 to 25 [15]	7 [16]	0.5 to 14 [35]
Power Consumption [W]		17 [14]	18 [15]	59 [16]	9.6 [35]

Despite this pattern being strongly biased by commercial satellites, even scientific missions have started exploiting the adaptability of microsatellites, e.g. CubeSats, for technology demonstration or as piggyback on bigger spacecraft for large missions [38]. This effort can ultimately lead to promising results: on the one hand, it could reduce the budget of future space missions in terms of Size, Weight, and Power (SWaP), enabling the exploration of remote frontiers of the solar system, not reachable with the current technology; on the other hand, it could permit the implementation of innovative approaches, like satellite swarms and formations.

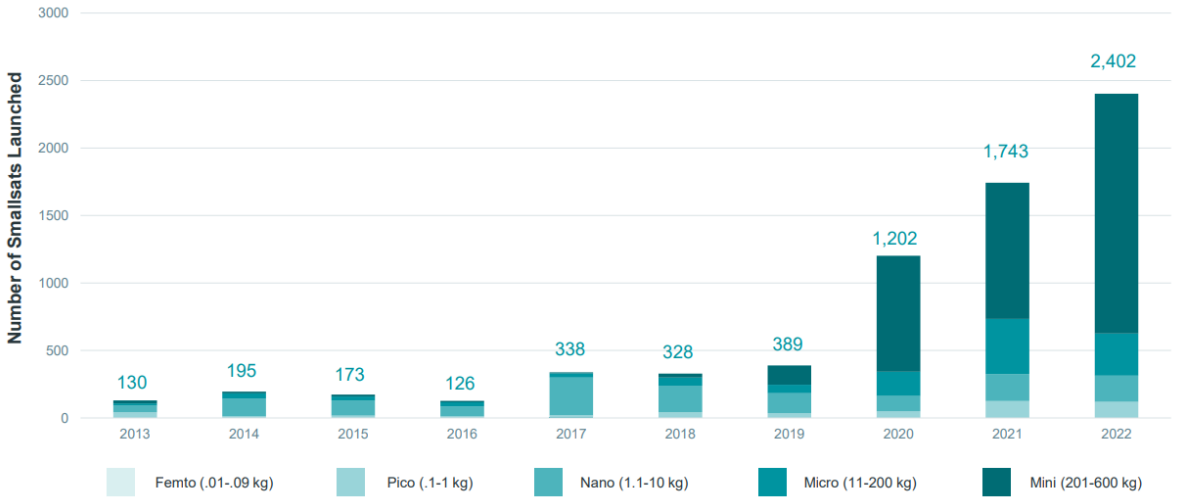

Figure 1.3: Number of Small Satellites (mass $<$ 600 kg) launched annually between 2013 and 2022, divided by mass categories. Figure from Bryce Tech [39].

Consequently, altimetry technology must adapt to the new state-of-the-art to maintain the continuity of the achievements made in the past. Some steps have been taken recently toward advancing miniaturised technology. Solutions deemed infeasible a decade ago due to their incompatibility with the energy levels produced by small satellites [40] are now gaining ground in strategic applications thanks to innovative technologies and the use of Commercial Off-The-Shelf (COTS) components. Technology

demonstrators like the navigation assistant prototype CLA (Compact Laser Altimeter) [41], the Cube Laser Communication Terminal (CubeLST) [2021] [42] or the Lunar Flashlight [2022] [43] have been developed to explore, respectively, the feasibility of navigation assistance, satellite telecommunications and scientific measurements using laser technology on CubeSats. Other concepts are still in the development phase, like the Cube Inter-Satellite Link (CubeISL) [42], a two-way evolution of the CubeLST, the Adaptive Wavelength Scanning LiDAR (AWSL) [44], the heir of NASA Earth observation legacy paved by GLAS and ATLAS, and the customised solutions offered by the American company Fibertek [45].

Nevertheless, at this point in time, no missions have successfully conducted topographic mapping through a CubeSat laser altimeter while providing an accuracy comparable to that of flagship missions of the past. What is still missing to guarantee miniaturised laser altimeters a spot in the future of space exploration?

This thesis will address this point through the design study of a miniaturised laser altimeter in development at the Deutsches Zentrum für Luft- und Raumfahrt (DLR) Institute of Planetary Research in Berlin. The preliminary concept of this technology demonstrator, conceived in the context of an ESA OSIP (Open Space Innovation Platform) call for mission proposals, is shown in Figure 1.4. It aims to employ state-of-the-art technologies to adapt the legacy the institute has derived from BELA and GALA instruments to the new miniaturised domain explored by the space industry. This thesis focuses on the optimisation of the optical design of the system while respecting the constraints dictated by the mission scenario outlined in the OSIP proposal. In the meantime, such technology's scientific relevance and applicability will be investigated and assessed through a test campaign.

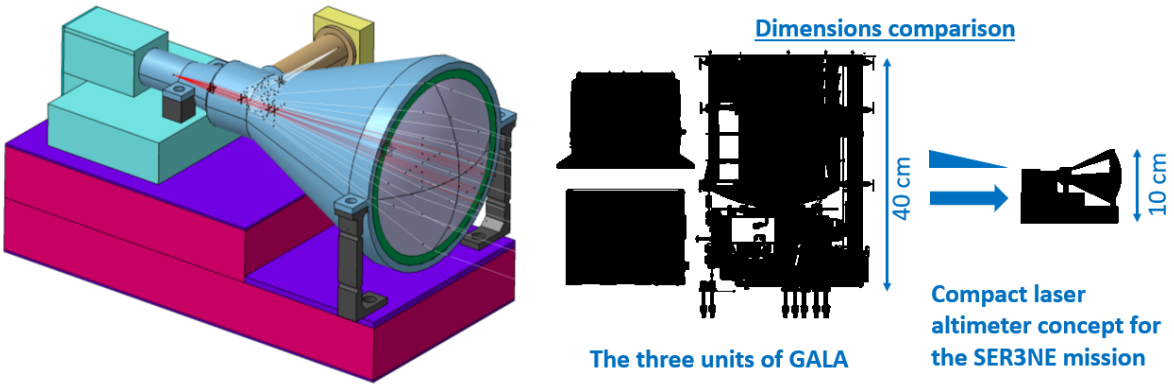

Figure 1.4: On the left, the conceptual design for the laser altimeter will be studied in this thesis developed by the German Aerospace Center (DLR) Institute of Planetary Research for the SER3NE (Selene's Explorer for Roughness, Regolith, Resources, Neutrons and Elements) mission proposal. On the right, a size comparison between GALA and the miniaturised laser altimeter. Figures from Lingenauber et al. [46].

Resuming the research goal of this thesis in one question:

To what extent can a Laser Altimeter be miniaturised for use in CubeSat missions aimed at topographic mapping?

Specifically, the project will address this main research question by emphasising the following sub-questions:

1. *Which technologies are necessary to adapt classical laser altimetry techniques to CubeSats?*
   This question is addressed in Chapters 2 and 3 of this thesis. Evaluating laser specifications, detection techniques, and the performance of past instruments, the focus is pointed toward the criticality of the transition to miniaturised altimeters. Limitations and benefits are identified, and a recommendation to practically fill the gap between past and future technology is provided.
2. *Which can be a functional optical design choice for a miniaturised laser altimeter for topographic mapping?*
   Starting from the study for the first question, a design exercise is carried out to select an optimum optical configuration for the miniaturised laser altimeter. The choice, based on a trade-off analysis

(Chapter 3) and numerical simulations (Chapter 4) using the optical design software Zemax, is then manufactured and implemented in-house through CAD design using the software CATIA (Chapter 5).

3. *What are the preliminary performance parameters of such a design choice?*
   This last question is addressed through a laboratory test campaign. The instrument is mounted in an elegant breadboard configuration and tested for alignment, beam quality, and optical performance (Chapter 6). The results will allow for quantifying the quality of the work done, establishing which limits persist in the adaptation to a space-qualified level and which capabilities have been demonstrated.

2

Background

This chapter delves into the theoretical background of laser altimetry in space. The subject is divided into the main aspects characterising this type of instrument: the transmission of the laser beam from the satellite to the target and the implemented techniques to collect it through a detector.

2.1. Transmission

2.1.1. Laser beams propagation

A LASER, an abbreviation of light amplification by the stimulated emission of radiation, is a highly coherent light source. This peculiar device, consisting of an active medium and a cavity that amplifies only selected wavelengths and directions, permits the generation of a light beam with a well-defined frequency that can, therefore, be controlled and implemented in specific applications [47]. The development and implementation of this technology were deemed so crucial that it merited a Nobel Prize in Physics in 1964. However, the attempt to implement it in practical uses passes through understanding the pattern of the light expelled by the source.

As a first approximation, the intensity profile of the fundamental Transverse Electromagnetic Mode TEM_{00} of a laser beam wavefront resembles a Gaussian distribution, described by the formula 2.1 [47] and shown in Figure 2.1.

$$I(x, y) \propto e^{-k(x^2+y^2)} \tag{2.1}$$

Here, x and y represent the transversal coordinates on the propagation plane, respectively, while k is a constant dependent on the laser generator's internal features.

It is possible to identify two characteristic sections on this wave: the Full Width at Half Maximum, or FWHM, identified as the beam size at 50 % of the maximum intensity, and the waist, defined as the width at which the intensity falls to $1/e^2$, corresponding to 13.5 % of its maximum. This last feature is also shown in Figure 2.1 and will be used as a reference for the rest of this description of the laser beam. However, these parameters are defined at the generation of the laser, where they are minimised and tend to increase while the beam propagates.

Keeping track of the beam cross-section makes it possible to trace the longitudinal profile of the laser beam. During propagation, the laser wavefront acquires curvature along its path due to diffraction [48]. To account for this deformation, the system is studied using specific parameters: the radius of curvature R and the cited beam cross-section w, both evaluated along the longitudinal direction of propagation z. The following formulae describe the cited variables:

$$R(z) = z\left[1 + \left(\frac{\pi w_0^2}{\lambda z}\right)^2\right] \tag{2.2}$$

$$w(z) = w_0\left[1 + \left(\frac{\lambda z}{\pi w_0^2}\right)^2\right]^{1/2} \tag{2.3}$$

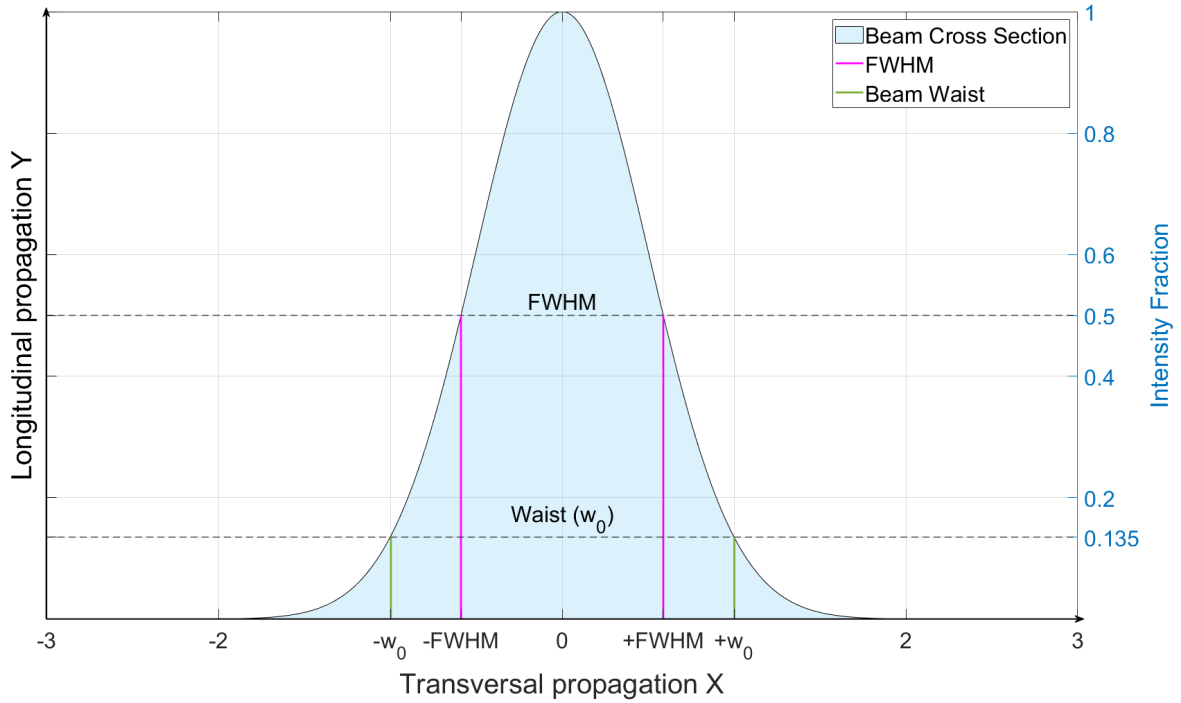

Figure 2.1: Intensity profile of a Gaussian laser beam. On the z-axis, representing the longitudinal direction of propagation of the beam, there is the fraction of intensity transmitted at each cross-section point. On the x-axis, the transversal propagation with respect to the centre of the beam. The y-axis is not visible here, but it would be going inside the sheet. 'w_0', namely the beam waist radius, is defined as the section corresponding to 13.5% of the maximum intensity at the flat wavefront plane.

where w_0 is the $1/e^2$ contour at the flat wavefront plane, i.e. the beam waist, and λ is the laser wavelength. This change in the shape of the section of the laser beam does not modify the Gaussian distribution of the intensity assumed at the flat wavefront plane, which remains unchanged until the end of the propagation. Consequently, one can rewrite the intensity equation in terms of the just introduced variables:

$$I(R,z) = I_0 \left(\frac{w_0}{w(z)}\right)^2 \exp\left(-\frac{2R^2}{w(z)^2}\right) \tag{2.4}$$

Here, the first term, I_0, accounts for the original irradiance at source and the parentheses for longitudinal and transversal direction variations, respectively [49]. Studying Equation 2.2, it is possible to reconstruct the behaviour of the beam's cross-section through the direction of propagation. When z=0, the radius of curvature tends to be infinite, meaning that the wavefront is flat and section $2w$ coincides with the beam waist diameter, $2w_0$. Moving forward, the radius of curvature passes through a minimum before approaching asymptotically the value of z itself.
This pattern is visible in Figure 2.2, where it is compared to the trend of the section radius. The latter keeps increasing for the entire propagation, resembling the shape of a cone of angular radius θ, where:

$$\frac{\theta}{2} = \frac{w(z)}{z} = \frac{\lambda}{\pi w_0} \tag{2.5}$$

The angle θ is an essential parameter for characterising a laser beam and, eventually, an instrument performance. Indeed, its double, called the laser beam divergence, permits the determination of the expansion of the beam and the prediction of the area covered by the laser footprint once it reaches the target.

However, the radius of curvature and section radius are not independent. As visible from the Equations 2.2 and 2.3, with the beam waist defined, both of them are fully specified by the same two variables: the distance from the flat wavefront and the wavelength of the laser. Consequently, the minimum of the curvature radius coincides with the distance where the beam waist assumes a precise value, $\sqrt{2}w_0$.

This specific distance, called the Rayleigh range, can be computed as:

$$z_R = \frac{\pi w_0^2}{\lambda} \tag{2.6}$$

This point delimits the passage from the Near-Field, where the beam is still irregular and may assume complex intensity and phase patterns, to the Far-Field, a much more stable region. Indeed, the measurement of mission parameters like the divergence must be performed very far away from the Rayleigh range, usually at distances ten times bigger, to get reasonable results for the parameters of interest[48].

Figure 2.3 summarises the details and features of laser beam propagations.

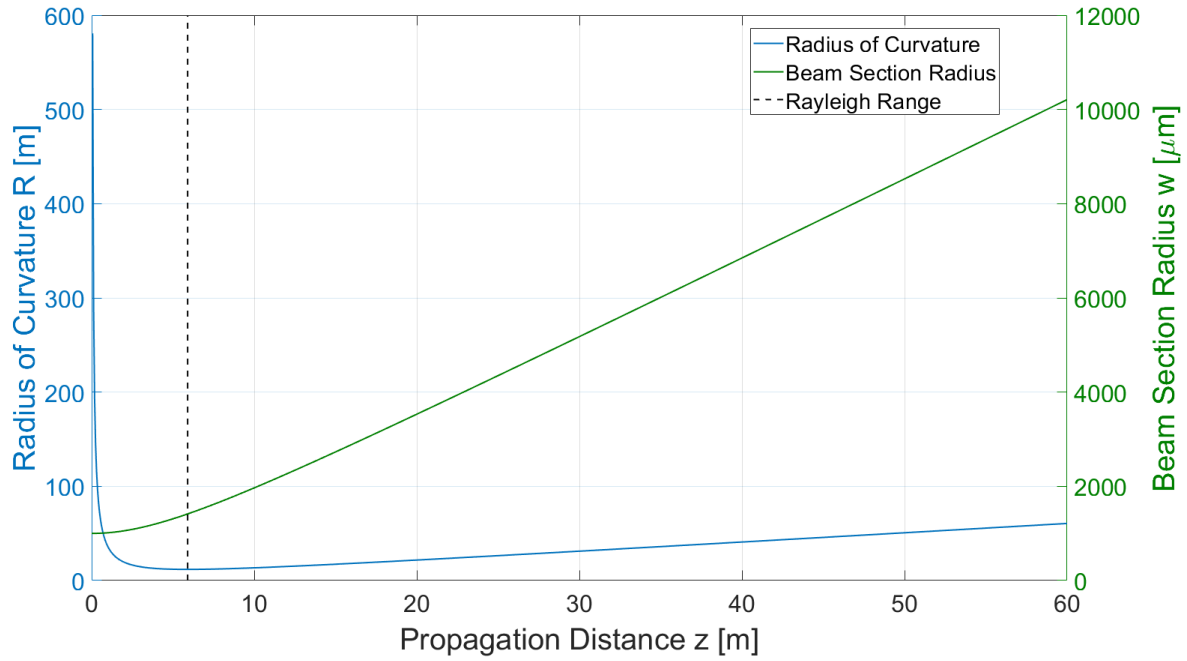

Figure 2.2: The radius of curvature (R) and the beam section radius (w) as a function of propagation distance (z). The radius of curvature presents a minimum at a specific distance, the Rayleigh range (dotted line), where the waist radius is increased by a factor $\sqrt{2}$. In this graph, the initial waist value, w_0, was set to 1000 μm, while the wavelength was set to 532 nm.

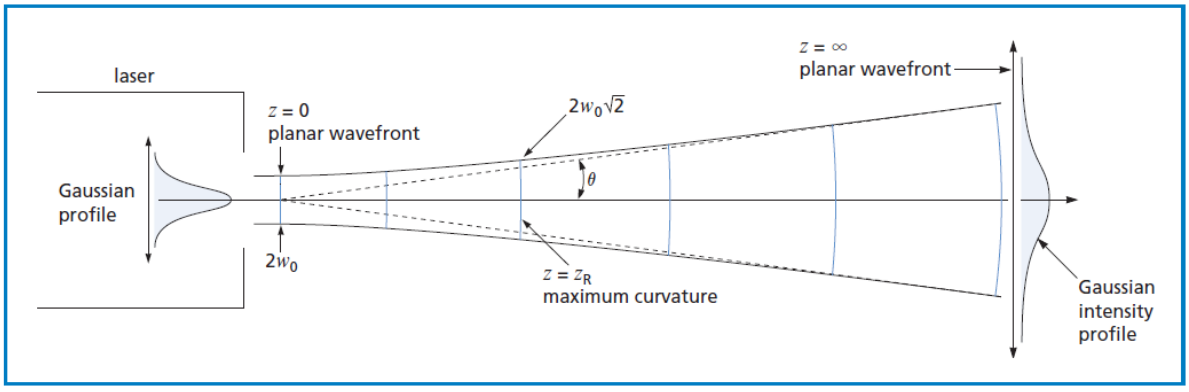

Figure 2.3: Summarising scheme of laser beam propagation, highlighting the evolution of w and R along the longitudinal direction of propagation z. Figure from CVI Melles Griot [48].

2.1.2. Ideal vs. real lasers

The cited instability of the Near-Field conflicts with the assumption of a perfect Gaussian distribution, and indeed, it is one example of the non-ideal behaviour of laser beams in reality. This occurs because the mechanism of light excitation induces the emergence of higher orders of resonance in the optical

cavity, leading to the formation of a mixed laser beam. As one might expect, the more significant the contribution of these higher orders, the more critical the deviation from the ideal Gaussian beam will be. A quality factor must be introduced to account for this: the so-called M^2 factor or propagation constant. Its definition is based on the fact that two of the main geometrical parameters of a laser beam, namely the waist radius and the Far-Field divergence, keep their product constant over the entire length of the beam [48], as visible also from Equation 2.5. Hence, the quality of an actual laser in approaching an ideal one is evaluated according to:

$$M^2 = \frac{w_{0R}\theta_R}{w_0\theta} \tag{2.7}$$

corresponding to the ratio between real and ideal behaviour. M^2=1, for example, defines a perfect Gaussian beam. The presence of deviations from the ideal pattern has an echo in the shape of the beam, as is evident when comparing the propagations of a real and a perfect laser (Figure 2.4), and in the formulation of the two principal coordinates: since a factor M increases both the waist radius and the divergence, the final corrections for Equation 2.2 and 2.3 in case of real laser beams are:

$$R_R(z) = z\left[1 + \left(\frac{\pi w_{0R}^2}{\lambda z M^2}\right)^2\right] \tag{2.8}$$

$$w_R = w_{0R}\left[1 + \left(\frac{\lambda z M^2}{\pi w_{0R}^2}\right)^2\right]^{1/2} \tag{2.9}$$

In addition, also the Rayleigh range is affected by this correction:

$$z_{RR} = \frac{\pi w_0 R^2}{M^2\lambda} \tag{2.10}$$

From now on, this thesis will consider only real laser beams, and the M^2 factor will play a role in the presented design process.

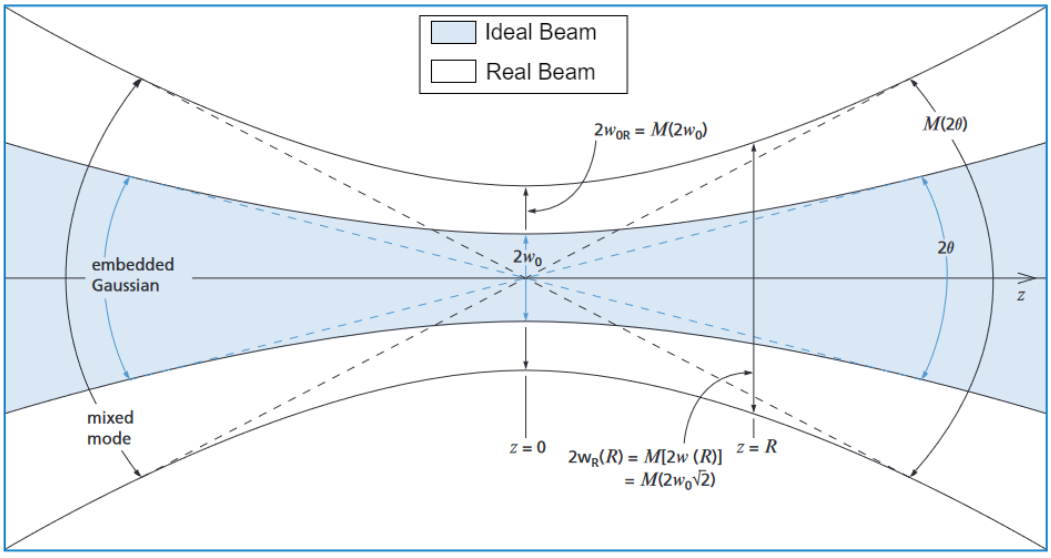

Figure 2.4: Comparison between real and ideal laser beam geometries at the beam waist radius. The divergence and the waist increase by M in the real beam (see text for details). Figure from CVI Melles Griot [48].

2.1.3. Interaction with optical systems

When a laser passes through lenses, it undergoes a transformation that changes its geometry and invalidates the continuity of the above fundamental equations. Therefore, each section must be evaluated singularly in dependence on the effects of the just-crossed lens and the direction of propagation. To design an optimised optical system, one must consider the rules governing the physics of

this phenomenon: the lens equation adapted to laser systems (Equation 2.11, from Self [50]) and the magnification m (Equation 2.12 [48]).

$$\frac{1}{(s/f)+(z_R/M^2 f)^2/(s/f-1)}+\frac{1}{(s"/f)}=1 \tag{2.11}$$

$$m=\frac{f_2}{f_1} \tag{2.12}$$

The first one accounts for the dimensions of the principal actors of a lens, namely its focal length f, the object distance s, and the image distance s", and their relationship with laser parameters like the Rayleigh range and the M^2 factor; the second one establishes the transformation of the transversal section of the beam when passing through a double lenses system characterised by the focal lengths f_2 and f_1. Both are useful for determining the distances between optical elements and the resulting size of the output laser footprint. However, most optical systems also need more than two lenses to focus a laser beam. In those cases, the total magnification of the system is computed as the product of all magnifications.

During the design, the previous discussion translates into selecting optical elements and establishing their relative positions to obtain the desired footprint on the target. Selecting one of the two most popular configurations, namely the Keplerian or Galilean configurations presented in Figure 2.5, is common practice for expanding a laser beam.

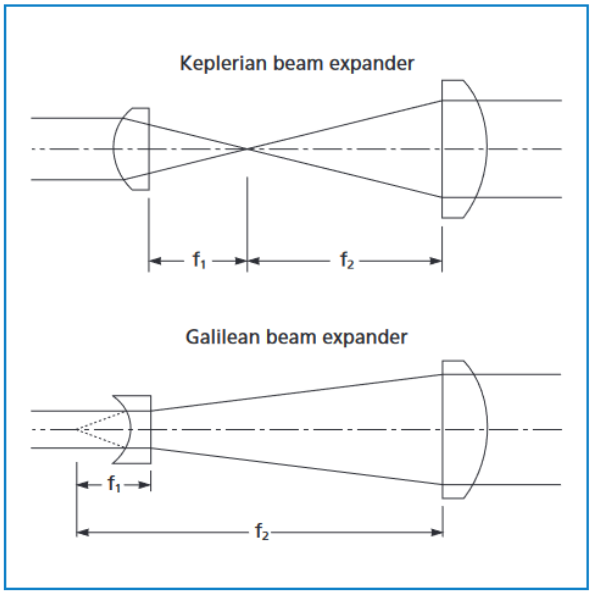

Figure 2.5: Comparison between Keplerian and Galilean beam expanders. Figure from CVI Melles Griot [48].

In a Keplerian beam expander, both lenses are converging and confocal. This configuration permits accurate control of the laser beam geometry because the common focal point allows for the introduction of spatial filters, which can clean the beam profile. In the Galilean beam expander, instead, the first lens is diverging. This means the laser only expands after the first lens without inversion points. It is then impossible to set a control point for the beam, but the design can benefit from a shorter length. This is often preferable for space applications, so Galilean expanders are most widespread in space instrumentation.

Once the expansion takes place, it is also paramount to verify the optical configuration's compliance in inducing the correct magnification of the beam, achieving the desired divergence values for free propagation up to the target. This check is also essential to verify that the optical system does not worsen the M^2 quality factor or provoke unforeseen modifications in the beam that can jeopardise the measurements during the mission.

The test procedure for the induced expansion is described in the ISO Standard 11146-1 [51]. To analyse the geometrical characteristics of the laser beam after its passage in the tube, one should find

the position of the new waist and measure its size. However, this location is not known a priori, and most of the time, it's a virtual beam feature that does not manifest in reality. Therefore, the solution is to induce an artificial waist in the beam by inserting a focusing lens after the examined component, as shown in Figure 2.6.

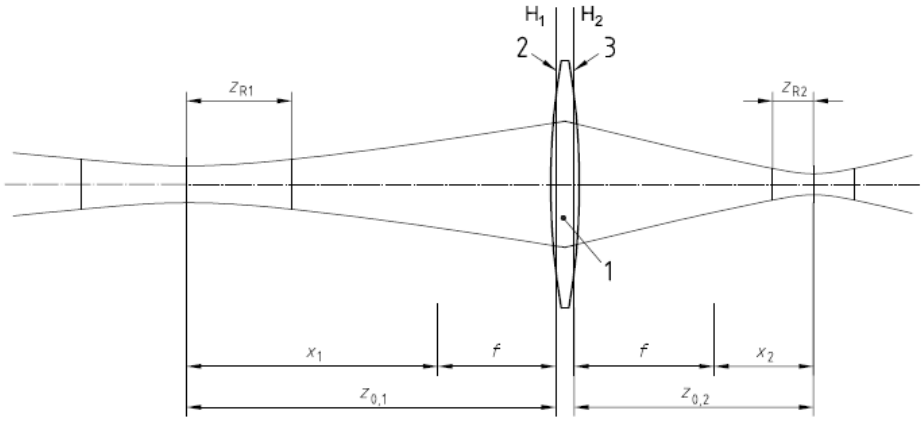

Figure 2.6: Sketch of the physical behaviour of the laser beam after passing through the focusing lens. By knowing the position of the artificial waist $z_{0,2}$ and the focal length f of the lens, it's possible to reconstruct specifics of the initial beam as M^2 factor and divergence. Other geometrical features, like the Rayleigh ranges z_R and the distances between the waist and the focal points x, can also be assessed for both beams. The reference points for all of them are the lens's principal planes H. Figure from ISO 11146-1.

The new waist is close to the lens, usually a bit more distant than its focal length. By measuring the size of the beam section at least ten times around the position of the waist, five inside the Rayleigh range and five outside, it is possible to find a hyperbolic fit resembling the longitudinal section of the beam. The parametric equation, to be iterated minimising the sum of the squared deviations of the diameters, is the following:

$$d_\sigma = \sqrt{a + bz + cz^2} \tag{2.13}$$

where d_σ is the measured diameter, equivalent to double the radius w introduced before, z is the distance along the direction of propagation, and a, b, and c are the polynomial coefficient to be found. Since, in reality, laser beams are usually far from being axial-symmetric, x and y propagations differ and may require different coefficients.

The geometric specifics of the beam after and before the lens are a function of these coefficients, as shown in the following formulae, where subscript 2 refers to the parameters after the lens and subscript 1 to the parameters before the lens. For example, the distance of the waist from the lens is equal to:

$$z_{0,2} = \frac{-b}{2c} \tag{2.14}$$

While its size:

$$d_{\sigma 0,2} = \frac{1}{2\sqrt{c}}\sqrt{4ac - b^2} \tag{2.15}$$

For the Rayleigh range z_R, divergence θ, and M^2 factor, the following parameterisation apply respectively:

$$z_{R,2} = \frac{1}{2c}\sqrt{4ac - b^2} \tag{2.16}$$

$$\theta_2 = \sqrt{c} \tag{2.17}$$

$$M^2 = \frac{\pi}{8\lambda}\sqrt{4ac - b^2} \tag{2.18}$$

Now, it is possible to compute a conversion factor, X, that permits characterising the beam before the lens by knowing the just computed parameters after the lens.

$$X = \frac{f}{\sqrt{z_{R,2}^2 + x_2^2}} \tag{2.19}$$

where x_2, as visible in Figure 2.6, is the difference between $z_{0,2}$ and f. Once it is available, the properties of the beam on the other side of the lens are computable by applying:

$$z_{0,1} = X^2 \cdot x_2 + f \tag{2.20}$$

$$d_{\sigma 0,1} = X \cdot d_{\sigma 0,2} \tag{2.21}$$

$$z_{R,1} = X^2 \cdot z_{R,2} \tag{2.22}$$

$$\theta_1 = \frac{\theta_2}{X} \tag{2.23}$$

Having demonstrated that the footprint size at the target will match the mission constraints, assessing possible distortions induced on the signal by the optical components is now essential. Indeed, in laser altimeter applications, the lateral variations detected on the returning signal are supposed to provide helpful information about the characteristics of the target, as explained later in this section. These features can be faint signals on the Gaussian pulse distribution, which are already challenging to detect. In an ideal world, they would be the only feature embedded in the signal, and it would be easy to attribute them to interesting topographic properties. But in reality, aberrations occur. This effect is an inevitable consequence of the attempt to handle light through a lens system that presents curved surfaces, alignment errors, and manufacturing imperfections. When the light arrives with a high AOI (Angle of Incidence) from the boresight optical axis, its path will differ from the one of a ray passing precisely through it enough to distort the signal and create artefacts that could be misinterpreted as geological information.

A possible way to evaluate the wavefront's global quality implies studying the wavefront RMS error. Indeed, several empiric parameterisations relate the RMS error with the Strehl Ratio. This powerful index compares the maximum irradiance of an optical system with the maximum ideal irradiance of the diffraction-limited version of the same system. By calculating the value of the Strehl ratio, it is possible to understand how much energy the system dissipates due to intrinsic aberrations. One of the cited relationships is the Mahajan approximation [52] (Figure 2.7):

$$S \sim e^{-(2\pi\omega)^2} \tag{2.24}$$

Where S is the Strehl Ratio and ω is the RMS wavefront error.

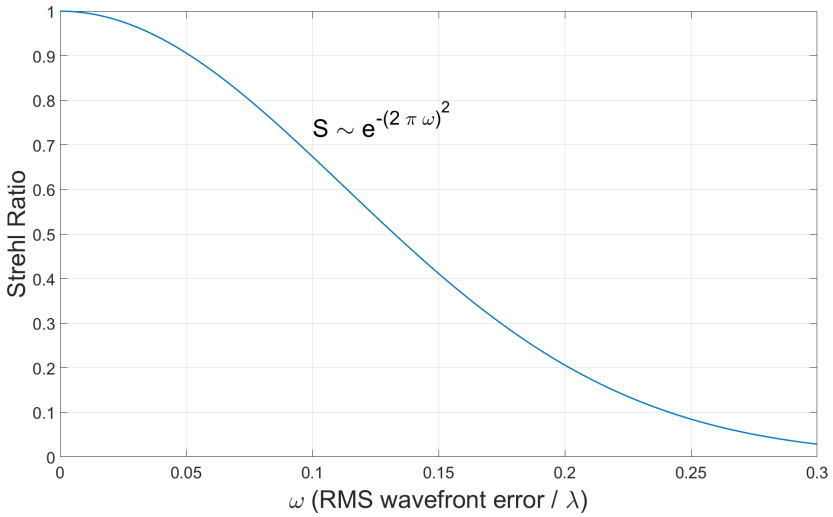

Figure 2.7: Trend of the Mahajan approximation relating the Strehl Ratio to the RMS wavefront error (weighted over the operating wavelength).

This expression is helpful for straightforward analyses because it avoids relating the Strehl ratio with the phase variance of the wavefront error, from which it is dependent. Instead, the Mahajan approximation overcomes the mathematical complexity of such studies with an empirical relationship that keeps accurate to 2% with RMS errors up to 0.1. A good practice in optics is to consider an optical

system diffraction-limited or aberration-free when its Strehl Ratio is above 0.8, corresponding to an RMS wavefront error around 0.075 according to the approximation.

Aberrations are intrinsic in optical systems and cannot be avoided. However, it is still possible to reduce the contribution of alignment errors by making the laser beam pass as much as possible through the centre of the lenses. A specific tool, the autocollimator, is used for this procedure.

Its working principle is explained in Figure 2.8. As the first step, it sends a light signal with a peculiar shape to the optical element that needs to be aligned. This signal is reflected to the autocollimator, where a dedicated detector captures it. For the second step, the laser beam is let pass through the lens, aiming at the autocollimator, where the detector again captures it. By tuning the lens tilting, it is possible to make the centre of the two signals overlapping. This means that the laser beam correctly passes through the centre of the lens perpendicularly, with a 0° AOI, minimising this contribution to the aberrations.

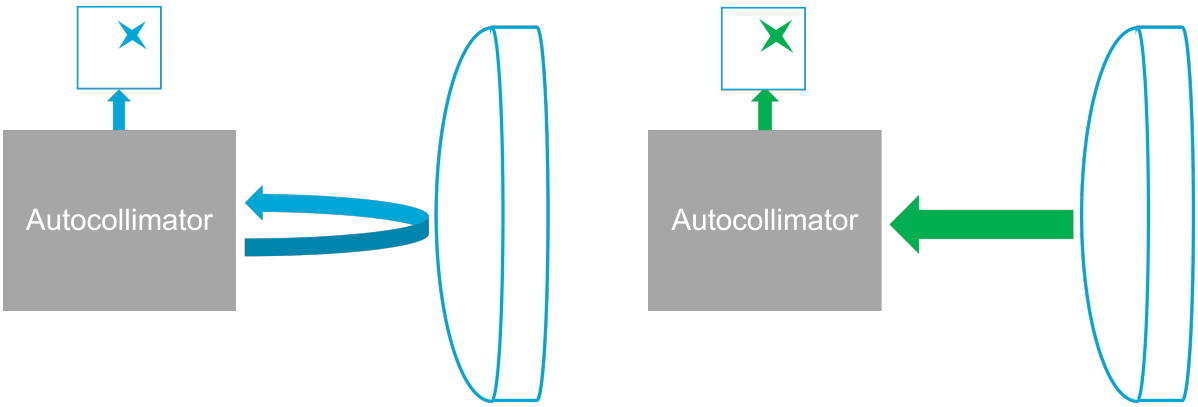

Figure 2.8: Working principle of the autocollimator.

2.1.4. Other relevant factors

However, laser beams are characterised not only by their geometry. Several parameters intervene from diverse domains and affect both the laser itself and many mission parameters. The main variables that usually influence the mission design process of laser instrumentation are as follows:

- *Wavelength*. The wavelength of the laser depends on the type of mechanism used to generate the beam and the possible implementation of additional components, such as crystals, capable of modulating the frequency according to precise proportions. The choice, especially for space applications, relies on the availability of space-qualified components and the suitability of the wavelength for both the target and the detector's performance. The amplification of the light intensity can happen in a solid-state medium, such as the most popular neodymium-doped yttrium aluminium garnet (Nd:YAG), a gas-state medium, a semiconductor diode, or an optical fibre. The resulting wavelengths are extremely specific for each generation process. Still, in general, the most popular ones in space missions are 1550 nm, 1064 nm, 532 nm, and tailored wavelengths in the case of laser spectroscopy.
- *Link Budget*. The link budget permits an estimate of the amount of energy received back by the instrument as a function of the amount of energy transmitted by the laser and the loss sources in the path. Using Equation 2.25 rearranged from Lingenauber et al. [1], one can properly design the light source to achieve the desired optical power at the detector:

$$E_R = \frac{E_T \xi_T \xi_R a d_T^2 T_A^2 Q_e c}{4H^2 \lambda^2} \tag{2.25}$$

where E_R is the received energy, E_T is the emitted energy, ξ_T and ξ_R are the transmittance losses in the transmitter and the receiver optics respectively, ad_T is the receiver aperture diameter, T_A is the fraction of optical power loss due to atmospheric attenuation (if present), Q_e is the quantum efficiency of the sensor (the effectiveness of the device to convert a photon into an electron), λ is

the wavelength, and c is the speed of light. Note that Planck's law was applied to determine E, the energy of a single photon:

$$E = h\frac{c}{\lambda} \tag{2.26}$$

with h as the Planck's constant ($6.63 \cdot 10^{-34}$ J $\cdot$ s).

The energy values can be translated into the power domain:

$$P_P = 0.94\frac{E_T}{t_p} \tag{2.27}$$

where P_P is the peak power of the laser pulse, E_T is the emitted energy, t_p is the pulse duration at the FWHM, and 0.94 is a corrective factor to convert from a squared pulse approximation to Gaussian pulses.

- *Repetition Rate*. A satellite will have a variable orbital velocity depending on its distance from the ground and the type of orbit it follows. Since the main goal of a laser altimeter is to cover as much surface as possible on the target, the repetition rate, namely the speed with which laser pulses are sent to the target, becomes a crucial parameter for mission design. The closer the satellite approaches the target, the faster the laser must be to avoid empty spaces on its swath.
  However, other aspects play a role in selecting the best repetition rate. As explained later in this report, depending on the type of detection approach implemented in the mission, multiple scans of the same region may be required to collect enough statistical data to characterise the topography. This is the case of single photon-counting approaches.
- *Pulse Width*. The width of a laser pulse determines the time frame in which the light coming from the laser is contained. In laser ranging applications, this quantity should be as short as possible to condense the energy and reach a better temporal resolution. By doing so, the probability of detecting noise during the reception of the signal is also reduced.
- *Number of beams*. In laser applications, generating multiple beams at once is possible by implementing multiple generators or a beamsplitter. This choice is not dependent on the laser performance. Still, it may be implemented for particular applications, like when it is necessary to increase the instrument coverage without stressing too much on the beam expansion and keeping the capability to detect spatial variations on the target accurately. Examples of this approach are the missions ATLAS and LOLA.
- *Clipping*. When expanding a laser beam, it may happen to have wanted or unwanted apertures on the path. Clipping happens when the section of the beam is bigger than the aperture. This phenomenon is a source of dissipation in the link budget of a laser link because the generated diffraction tends to increase the beam's divergence and, consequently, the area on which the laser's energy is distributed. This section will not go deep into clipping details, but the design exercise will consider it to reduce possible error sources in the calculations.

2.2. Detection

2.2.1. Detection principle

The physical concept behind laser altimeters' working principle relies on knowing the spacecraft's operative range from the target body's mean radius, from which one can subtract H, or the range of the spacecraft from the surface:

$$H = \frac{c\Delta t}{2} \tag{2.28}$$

To estimate the altitude of the topography. Here c is the speed of light ($3.00 \cdot 10^8\ m/s$), and Δt is the period between the emission and the reception of the laser pulse. Factor 2 in the division considers both legs of the signal's round trip.

Additionally, by implementing a bidimensional pixel array and reducing the effects of the aberrations mentioned before, it is possible to obtain additional information from the lateral variations in the Gaussian intensity distribution regarding the terrain slope, roughness, and albedo (or fraction of reflected

intensity) by analysing the variations in pulse spread for the first two parameters and intensity for the last one [28].

The receiver optics must be designed such that the Field of View (FoV) of the instrument, intended as the angular extension reachable by the instrument for a given orientation, matches the desired footprint size of the laser beam on the ground at a given altitude. The geometrical problem can be assessed as follows:

$$FoV = \frac{Footprint\ size}{H} = \frac{Detector\ Size}{f} \tag{2.29}$$

Where H is again the distance from the surface and f is the focal length of the receiver optics. The focal length is the key design parameter because the detector size is usually constrained by manufacturing limitations in fitting the electronics in a small space. Still, the dimension of the pixels affects the spatial resolution achievable by the system, namely the minimum resolving distance between two points on the target.

2.2.2. Working principle of photon detectors

The photodiode is the essential component that permits the collection of the photons composing the laser pulse for the measurements. It exploits a p-n junction, an overposition of positively and negatively doped semiconductor material, as visible in Figure 2.9. Applying a constant negative voltage, the device accumulates the vacancies and the electrons at the opposite ends, creating a middle zone called the depletion zone, where the atomic structure is densely populated. When the photodiode is exposed to light, this region catches photons and absorbs their energy. As a result, due to the so-called photoelectric effect, electron/hole pairs are generated, with the former promoted from the valence band, where the material behaves as an insulator, to the conduction band, where the material allows the presence of internal currents and permits them to follow the external electrical field generated by the voltage.

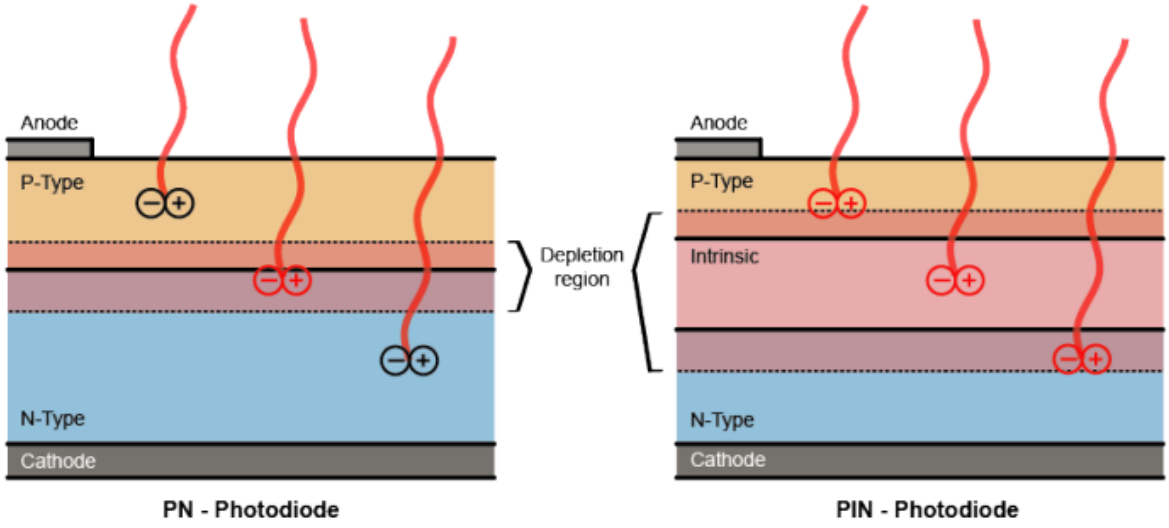

Figure 2.9: On the left: p-n junction photodiode scheme, where it is possible to see the differentiation between p-doped, n-doped, and depletion layers. The electrons stopped far from the latter are not detected by the device. On the right: a p-i-n junction photodiode scheme, where the depletion zone is thickened thanks to including a non-doped region. In this case, a broader swath of wavelengths can interact with the atomic structure, but the electrons will take longer to exit from the region. Figure from Gualani [53].

The generated current, converted into a voltage and amplified to appreciable levels, feeds a signal that can be considered proportional, for a first approximation, to the number of photons hitting the material with enough energy to excite its electrons. The linearity range persists until a specific limit, called saturation, where the photodiodes hit their maximum capacity and start slowing the photon-electron conversion. If a photodiode is oversaturated with enormous intensities in a very short period, as could be the case for direct exposure to a laser beam, it can be irremediably damaged. The specific

value at which this phenomenon happens is called the damage threshold and is extremely important for laser applications, thus will be also investigated in this project.

The challenge in detecting laser pulses with this kind of device is that the detector generates a signal every time it's triggered by a photon coming from the background, internal reflections, or its own electrical noise. These sources of noise make the isolation of the scientific signal more complex.

Over the past years, several approaches have been applied to compute the time of flight of the returning laser pulse and reduce false detection. The most basic principle is represented by leading-edge timing. In this application, a portion of the transmitted signal is sent to the detector to establish the beginning of the measurement. The timing system detects the point on the pulse rising edge where the signal exceeds a predetermined threshold; then, it waits for the detection of another signal with enough energy to surpass the threshold again and computes the difference in time between the two [2]. In this way, the differential measurement roughly estimates the time of flight of the laser pulse.

This principle works because the quasi-Gaussian distribution of the laser pulse is coherent over time, even if the interaction with topographic features provokes the alterations mentioned before in the spread and intensity of the pulse. However, the method presents two main technical threats [54]:

- Although the Gaussian distribution is preserved, its shape proportions change over time. As visible in Figure 2.10, the returning pulse shape will differ from the original one, usually presenting a more flattened and wavy energy distribution. Hence, the moments when the threshold is exceeded do not correspond to the same point on the signals. This error source is attributable to the range walk.
- In addition to the previous point, the electronic jitter of the signal is not entirely predictable. It adds uncertainty in determining the precise moment the threshold is crossed.

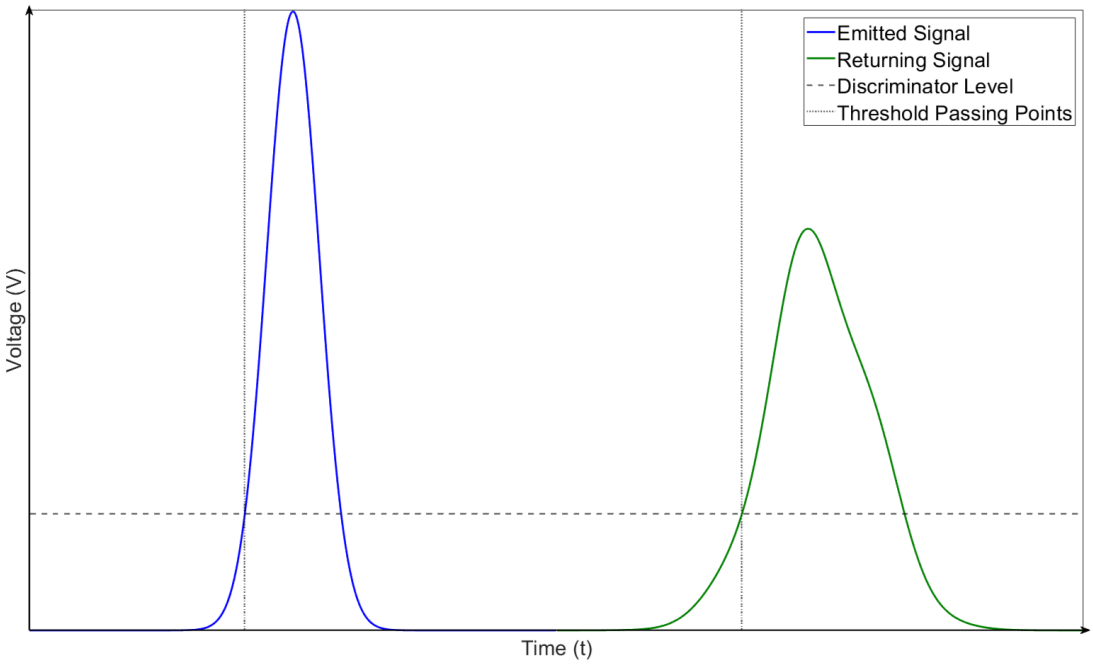

Figure 2.10: Simple scheme to explain the leading-edge method. On the y-axis, the voltage of the converted signal on the detector. On the x-axis, the timeline of the measurement. The discriminator level, corresponding to the predetermined threshold, crosses the emitted signal (in blue) and the returning signal (in green) at two different points but still ensures the cut-off of the noise. Computing the time difference between the two detections permits estimating the time of flight of the pulse.

Both of these parameters generate errors in the vertical accuracy of the instrument. Nowadays, innovative strategies permit the increase of the capabilities of LiDAR system by allowing for the discretisation and sample of the entire wavefront. The intrinsic features can be processed with high precision thanks to extremely fast counter-clocks, enhancing the mission's scientific return. Nonetheless, this approach costs in the power consumption required to operate the electronics and the onboard computer, and in the data rate for the transmission to the ground segments [55].

2.2.3. Avalanche photodiodes and single-photon sensitivity

A possible solution to the problem comes from the bias voltage at which the photodiodes are operated. When it is increased beyond a specific value, namely the impact ionisation threshold [56], the carriers gain enough energy to induce the formation of additional electron/hole pairs [57] and generate an avalanche multiplication. With minor adjustments in the structure of the photodiodes, one can deploy this strategy to amplify a few photons into a current already in the silicon structure and then convert it into appreciable voltage levels in the external electronics.

The technological translation of the mentioned approach is the Avalanche PhotoDiode (APD) visible in Figure 2.11. It resembles a p-i-n junction with an additional p-doped layer after the intrinsic region. Due to the high voltage level in the new layer, the electrons can induce an avalanche effect and multiply the carriers in the silicon.

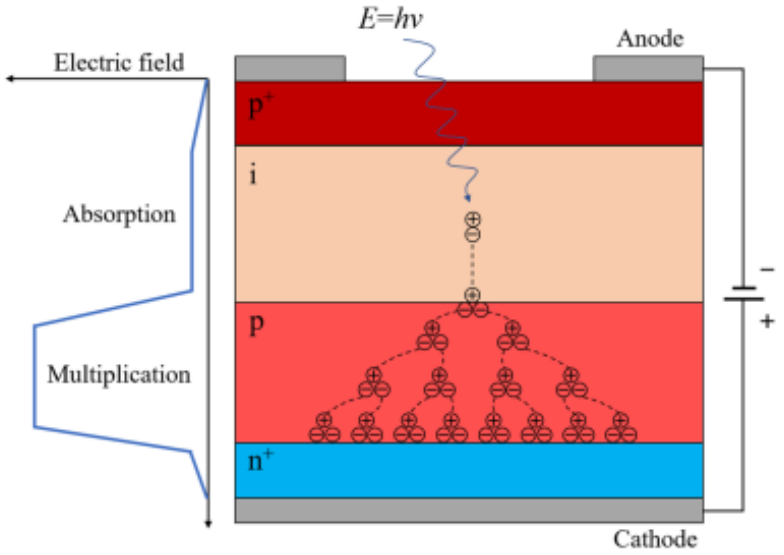

Figure 2.11: APD structure. Along with the classical p-i-n configuration, another layer of p-doped material is added after the intrinsic zone. In this region, where the higher electric field is generated according to the graph on the left, the avalanche process proliferates the formation of electron/hole pairs. Figure from Wang and Mu [56].

But it is possible to go further. Applying even higher voltages to the photodiode, one can reach and exceed the so-called breakdown voltage. Operating under this condition, the photodiode enters a metastable phase called Geiger mode, and until a photon reaches the device, it remains stable and behaves like an insulator. When even a single photon strikes the sensor in the depletion zone, the intense electric field charges it enough to generate a self-sustaining avalanche, transforming the photodiode into a proper conductor [58]. The performance of this configuration is evaluated based on the excess bias voltage V_E, as shown by Equation 2.30:

$$V_E = V_A - V_B \tag{2.30}$$

where V_A is the bias supply voltage, and V_B is the aforementioned breakdown voltage.
Again, it is a matter of compromises. Having a high V_E increases the photon detection probability and the time resolution of the photodiode, but also the dark count rate generated by the electronics [58] and the possibility that previously generated electrons provoke an avalanche with some delay, referred to as afterpulsing noise [59]. This choice is reflected in the system's recovery after the detection event. Indeed, once the photon triggers the junction, the transition it experiences does not reverse automatically, and the diode keeps operating as a conductor. The system can be restored to Geiger mode only by using a quenching circuit. The operative steps, illustrated by Figure 2.12, are the following [58] [59]:

- A high-speed comparator senses the rising edge of the current generated by the avalanche (1→2);
- An output, synchronised with the avalanche, is generated to define a time tag for the event;
- V_A is lowered at the same level or even below the V_B (2→3);

- After a precise period called the hold-off time, the photodiode is set again to the nominal operational bias (3→1).

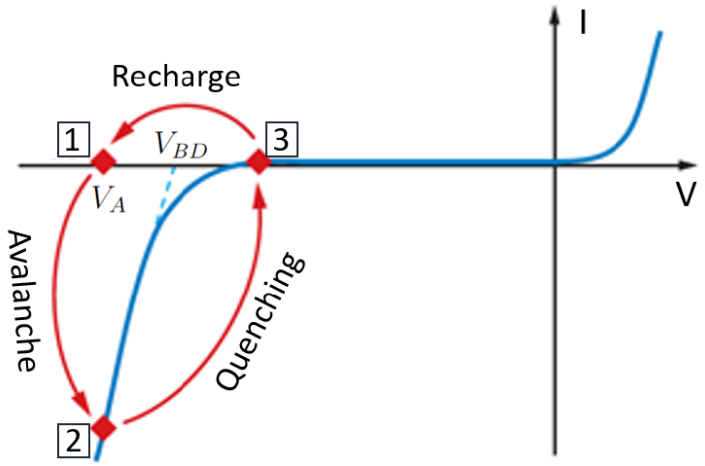

Figure 2.12: Voltage (x-axis) vs. Current (y-axis) graph for a SPAD. The operations can be divided into three main tasks: Avalanche (1→2), where the junction is excited by a photon and generates current; Quenching (2→3), where the quenching circuit intervenes to set the operational voltage below the breakdown voltage; Recharge (3→1), where the system rests for a defined hold-off time and then is set again to the operational bias level. Meantime, the generation of the avalanche is recorded with a time tag. Figure from Meiré [59].

This limitation implies that the continuous acquisition of the signal to perform a wavefront analysis as in normal altimeter approaches is no longer possible. Therefore, a new technique must be introduced: it involves the statistical reconstruction of the laser pulse from the number of detection events and their distribution in time. However, to fit in the same operational time frame as the classical approach, this detection scheme demands higher repetition rates to collect a large enough sample of photon detection on which to perform the statistics.

Since time constraints are so severe, it is paramount to account for a pixel array so that lateral variations in two dimensions can still be measured. Indeed, choosing a single pixel would lead to the implementation of scanning techniques, where the scene is divided into portions that are investigated in a defined order and then reconstructed to recreate the original image. However, this process would limit the time allocated for collecting the sample and the consequent number of photons, reducing the interpretable information about the target.

3

Requirements Specification and Trade-off Criteria

After introducing the context of the instrument at the centre of this project, this chapter explores the system engineering approach applied to identify the most suitable optical design. The strategy involves evaluating and defining the driving requirements for a trade-off analysis and studying possible design choices. In the end, the best candidates for further studies are identified.

3.1. General Mission Overview

Combining the two main physical aspects explored in the previous chapter, namely laser optics and photosensitive detectors, it is possible to design many different laser altimeters, adapting them to each mission's dimension, goal, and target constraints. This heterogeneity is evident in the examples listed in Chapter 1, with a summary of almost all the milestone instruments developed by space agencies in the past decades.

Indeed, the same applies to the development of the instrument at the centre of this research. It is based on the mission scenario identified in the SER3NE mission proposal, imagined for an ESA call regarding small missions, with a total cost of up to 50 M€, aimed to "address primarily exploration and science aspects" of the Moon such as [60]:

- "Understanding environments in deep space and at the Moon and the effects on technology and biology of exposure to these environments";
- "Observing, predicting and mitigating changes that human activity will introduce to these environments";
- "Finding, characterising and quantifying potential resources and understanding how local environments affect resource-extraction processes";
- "Providing improved/higher resolution mapping of potential landing sites and locations of high interest for exploration".

In particular, the scientific goal expected for the instrument is to enhance the precision of vertical and lateral variation measurements on the Moon topography (dated back to LOLA) to:

- Study the composition and abundance of water ice reservoirs on the Moon, addressing their origin and correlation with other bodies in the Solar System;
- Estimate the shape of shaded regions more correctly, constraining the environmental conditions that permit the presence of volatile elements of interest for future human activities;
- Identify the presence of minerals in the regolith, giving insight into the geological and seasonal evolution of the body;
- Assess the tidal variations along the lunar orbit, putting constraints on numerical interior models predicting the long-term orbital evolution of the body.

These achievements do not come with any effort. Indeed, the main source of engineering challenges for the instrument design is represented by:

- *Miniaturization of the system*: the instrument will be carried on a 6-12 U (or CubeSat unit, corresponding to a volume of 10x10x10 cm^3). To permit the implementation of the rest of the payload and the onboard systems, the miniaturized altimeter will be constrained to a small volume of 3 U, a domain never undertaken before for topographic mapping laser altimeter.
- *Transceiver Design*: considering the previous point, the instrument's optical design must exploit as little space as possible. In the past, flagship missions could allocate different modules for transmitter and receiver units. This was permitted by the size, weight, and power (SWaP) available in the satellite budget, usually in direct proportionality with the funding granted to the project. All these indicators are limited for microsatellites, implying the necessity to share some elements of transmitter and receiver optical paths. By doing so, size can be minimized, and optical alignment between receiver and transmitter elements can be simplified, but at the cost of increased design complexity in the cross-coupling between the two sections [61].
- *Single-photon counting detection*: so far, laser altimeters have consistently implemented linear LiDAR detection techniques. This approach allowed for a more holistic study of the conformation of planetary surfaces, implementing at the same time a very reliable technology. However, as demonstrated previously, fitting it into miniaturized instruments is impossible. Geiger mode SPAD can overcome this technological gap, guaranteeing scientific data acquisition without prohibitive powers or data rates. Nonetheless, the limited heritage in this field represents an obstacle to their implementation.

Table 3.1 provides the expected specifications of the studied New Laser Altimeter (NLA). It is then possible to compare them with the reference missions reported in Tables 1.1, 1.2, and 1.3 to understand the perspective of the NLA in comparison with relevant missions. Indeed, some of them had the same topographic application, having the Moon as a target (LOLA, LALT) or being a heritage of the department at the nstitute of Planetary Research (BELA, GALA). Others are important because of their comparable size (HAYABUSA 1 and 2 LiDAR, OLA, and PALT) or their single photon-counting approach (GLAS, ATLAS).

Table 3.1: Resuming table for the main characteristics of the miniaturized laser altimeters studied in this project.

Characteristics		**New Laser Altimeter (NLA)**
Laser Specifications	N. of beams	1
	Wavelength [nm]	532
	Pulse Energy [mJ]	0.5-2
	Divergence [urad]	300
	Vertical Accuracy [cm]	5
	Repetition Rate [Hz]	275-135
Telescope Diameter [m]		0.075
Detector Type		SPAD
Detection Approach		Photon Counting
Mass [kg]		<4
Temperature Range (nom/surv) [°C]		-10 to + 40 -30 to +50
Orbit [km]		20-40
Power Consumption [W]		27
Length [cm]		<30

The result of this comparison is visualised in Figure 3.1, which shows a performance characterization of the instruments. In the specific, two quality factors are introduced. The first one is the Power Factor, representing the amount of power transmitted through the laser pulse at the front of the total power provided to the instrument. Resuming in one expression:

$$\zeta_P = \frac{E_T \cdot r}{P} \tag{3.1}$$

where ζ_P is the power factor, E_T the emitted pulse energy, r the repetition rate, and P the supplied power. This parameter measures the system's efficiency in distributing the supplied power to the laser source to perform the scientific measurements. Moreover, it helps evaluate other correlated factors. For example, the pulse shot energy is tailored to each mission depending on the link budget, considering altitude, receiver aperture, transmittance losses, quantum efficiency, atmospheric attenuations (if present), and operative wavelength. Furthermore, the repetition rate also accounts for the spatial

coverage of the target, propagating the effect of the altitude and the footprint size. Finally, the total power tells about the cost sustained by the entire instrument to match the asked performance.

The second one, instead, is the Size Factor, representing a ratio between the instrument's optical and mass performance. Resuming in one expression:

$$\zeta_S = \frac{ad_T}{M} \tag{3.2}$$

where ζ_S is the size factor, ad_T the receiver aperture and M the mass of the instrument.

Watching the graph, the distinction between the different types of missions is evident and polarized: navigation and landing missions favour efficiency in size, sacrificing more on the power side; Earth observation missions work with an opposite strategy, while topographic mapping seems to be oriented more on a balance between the two aspects. One possible explanation for this behaviour relates to each mission design's different purposes. If, for Earth observation, the close distance reduces the launch cost and permits more powerful instruments, navigation and landing missions are often long and must get close to a small target, which requires costly deep space manoeuvres. Moreover, those laser altimeters approaching asteroids are often multi-purpose instruments used for topographic measurements and close-up operations, meaning they are not optimised in power consumption for a specific duty.
Lastly, topographic instruments compromise the two approaches because of the distance to be travelled before reaching the target and the required high precision in the measurements.

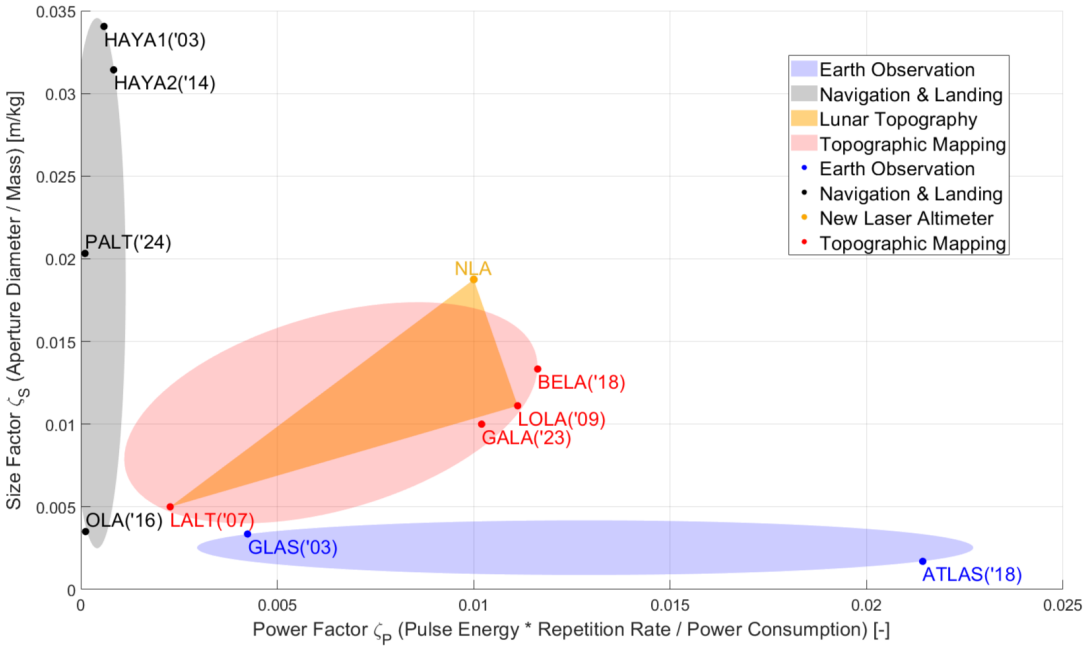

Figure 3.1: Scatter Plot of Power vs Size quality factors. When applicable, the power factor was multiplied by the number of beams emitted by the instrument.

Naturally, some outliers are present. The point is that each mission is unique and tailored to specific needs, making it extremely difficult to find perfect correlations, even for missions with the same target body or the same measurement goals. For example, in the navigation and landing cluster, OLA performs poorly size-wise. However, its mission duration is very long, including operations around two different asteroids, and probably, the mass is affected by contingencies and redundancies in this sense. An opposite explanation can be given for LALT. The Kaguya mission lasted slightly more than one year, avoiding the need to optimise the power consumption or the instrument's size performance. Compared to LOLA, still flying at the moment after 15 years of operations, the deficit in performance sounds reasonable.

Refocusing on this project, it is unfortunate that the plot does not reveal any correlation between the single-photon sensitivity of Earth observation instruments and NLA, leaving the investigation of

potential connections to future studies. Nonetheless, the initial predictions for the miniaturized instrument are promising. It appears well-balanced overall: it maintains the power efficiency of previous topographic instruments while approaching the exceptional size efficiency of navigation and landing altimeters, pushing into unexplored frontiers for planetary missions.

The proposed new engineering approaches for the instrument are the key drivers behind this anticipated improvement. Demonstrating their applicability and functionality is crucial to making it a reality. The first step in this extensive qualification process involves identifying an optical design for the instrument that incorporates these innovations while simultaneously meeting the mission's critical requirements.

3.2. Requirements

The SER3NE mission proposal is based on a thorough case study that cannot be exposed in the reduced context of this thesis. However, it is still possible to extrapolate the critical drivers for the instrument's optical design by studying the engineering requirements developed from the science case for NLA, which was partly resumed previously.

These requirements can be organised in a hierarchy (Figure 3.2), composed of:

- *Top-Level Mission & Instrument Requirements*, referring to the generic constraints imposed by the mission on the entire instrument due to environmental, SWaP, and orbit requirements;
- *Optical System Requirements*, referring to the system of the instrument that will be analyzed in detail through this project;
- *Detector and Laser Subsystem Requirements*, referring to the main subsystems of the optical system that will also be characterized as a consequence of the work done during this project;

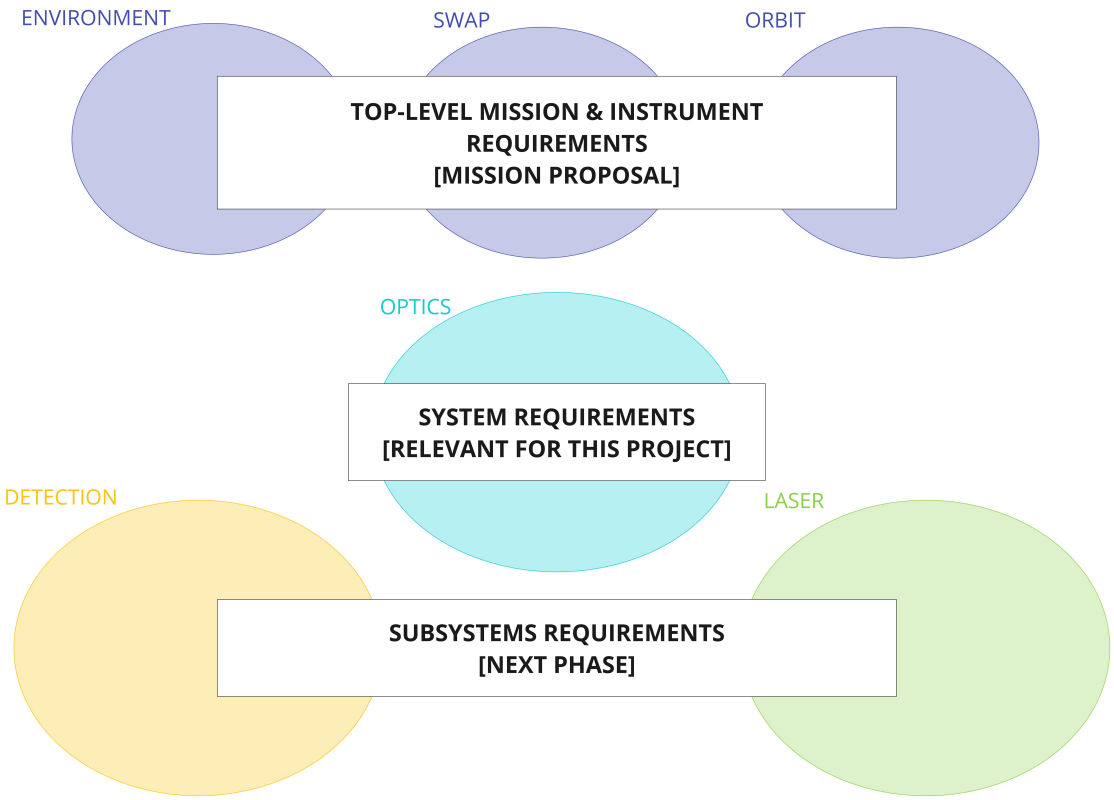

Figure 3.2: Design Level Hierarchy for the current project. 1) Top-Level Mission & Instrument Requirements, specified by the science case for the current project; 2) System Requirements, constraining the development of the optical system at the centre of the project; Subsystem Requirements, providing recommendations for the future characterization of detector and laser sections.

In particular, going into more detail in the middle section, the following five requirements have been identified as paramount to drive the design selection of the optical system:

- NLA-1:
  The Optical Unit shall fit in a total size of 2 U.
  RATIONALE: The NLA will be accommodated in a total space of 3 U. Constraining the instrument's optical system in 2 U would permit the fitting of:

  – the laser modules, including the laser head and the other components required to generate and control the pulses;
  – the fibre, to couple the laser source with the optics;
  – the detector plane, hosting the photon sensor;
  – the electronics modules, hosting the FPGA (Field-Programmable Gate Array) commanding and coordinating the laser generation and the detector acquisition, and the PCM (Power Converter Module).

  Figure 3.3 shows a preliminary schematic of this arrangement as suggested by the department. The different modules' precise shapes depend on the final design identified for the telescope and the other optical sections and, therefore, are not final.

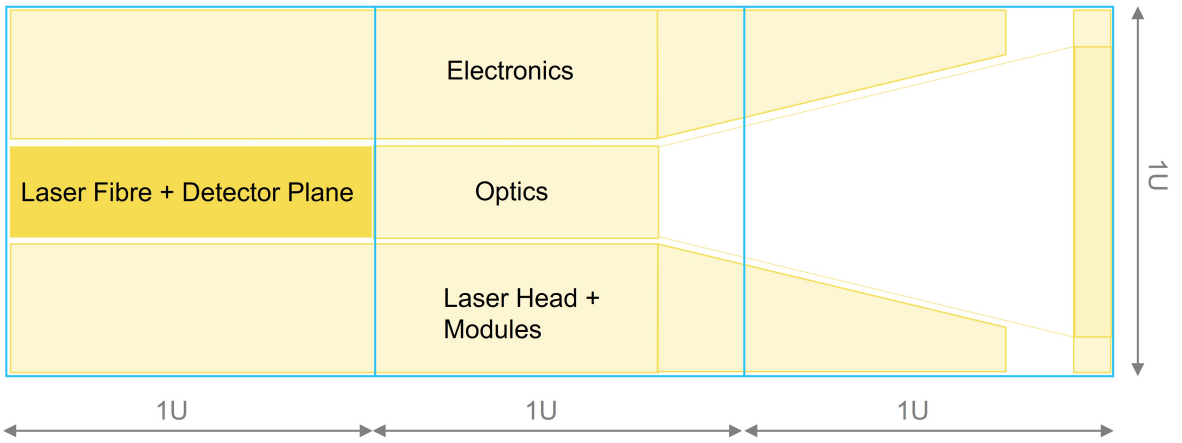

Figure 3.3: Side View schematic of the arrangement of the different subsystems in a three U volume.

- NLA-2:
  The Laser Altimeter shall implement a transceiver design.
  RATIONALE: Given the constraints of the satellite's volume, the receiver aperture size is a critical factor in the performance of the laser altimeter. The spacecraft allows for a maximum aperture of 10 cm, determined by the 12 adjacent U available. Maximizing this aperture is essential, as it directly influences the energy of the returning signal, as explained by the Link Budget Equation 2.25. Increasing the aperture size can enhance the received signal without demanding more power-intensive laser sources, thus optimizing the system's performance under power constraints.

  At the same time, the available power for the spacecraft, based on mission analysis studies, is 120 W for an average orbit, with only 35 W allocated for the laser altimeter. This limitation arises due to the simultaneous use of other payloads, platform maintenance, and the communication link with ground segments. Since detailed power allocation for each subsystem is still undefined, minimising power consumption by refining design parameters, such as the mentioned receiver aperture, is essential to improve the instrument's efficiency. Adopting a transceiver design, rather than using separate apertures for transmission and reception, maximises the aperture within the limited volume and reduces the overall demand on the system.

  Another important point comes from the alignment of the optics. In a differentiated design, one should check for the proper alignment of two independent optical systems, meaning that the receiver and transmitter should be finely co-aligned during the instrument's integration. Such a procedure is time-consuming and delicate, increasing the contingencies one should consider

during the instrument's design. With a shared optical design, the exit surfaces of the instrument are the same for both paths, meaning that only a few other optical elements still need to be aligned, speeding up the integration process of the instrument. Considering the limited time frame available for the mission before the launch, this aspect can demonstrate fundamental for the mission's success.

- NLA-3.1:
The cross-coupling between the laser source and the detector shall permit the detection of starting and returning pulses.
NLA-3.2:
The cross-coupling between the laser source and the detector shall avoid damage to the SPADs.

RATIONALE: Exploiting the lack of optical insulation between the transmitter and the receiver, the detection strategy implemented by the instrument follows the scheme represented in Figure 3.4. The detector is first activated and commands the laser generator to switch on. The laser emits pulses, which the detector identifies through their internal reflections. The SPAD gives back electronic feedback, used as reference time for the rest of the measurement. Then, the detector is switched off for a tailored amount of time based on a prediction of the TOF required by the light to travel a round trip back to the spacecraft. Once switched on again, a score of photons will hit the detector closely and provoke an electrical signal that is successively time-tagged with respect to the initial reference time.

This strategy avoids implementing specific optical elements to channel a fraction of the starting pulse to the detector, reducing the instrument's complexity and the required space. Nonetheless, the internal reflections must be: 1) not too faint to allow for the detection of the starting pulse; 2) not too strong to avoid the damage threshold of the pixels. While the former requires the capture of a few photons, considering the type of detector implemented in the system, the latter is more complicated to address. Indeed, no information is available about the damage threshold for SPAD, neither from the manufacturer nor the literature. A reference value of 200 kW/mm^2 [62] can be considered as a survival requirement. Still, it's coming from testing on traditional detectors, which implement the same CMOS (Complementary Metal Oxide Semiconductor) technology but with different operative voltages.

Considering these uncertainties at this point in the instrument's development, the strategy for this research will be to minimise the power density levels reaching the detector; the identification of the actual damage threshold will be left to future studies.

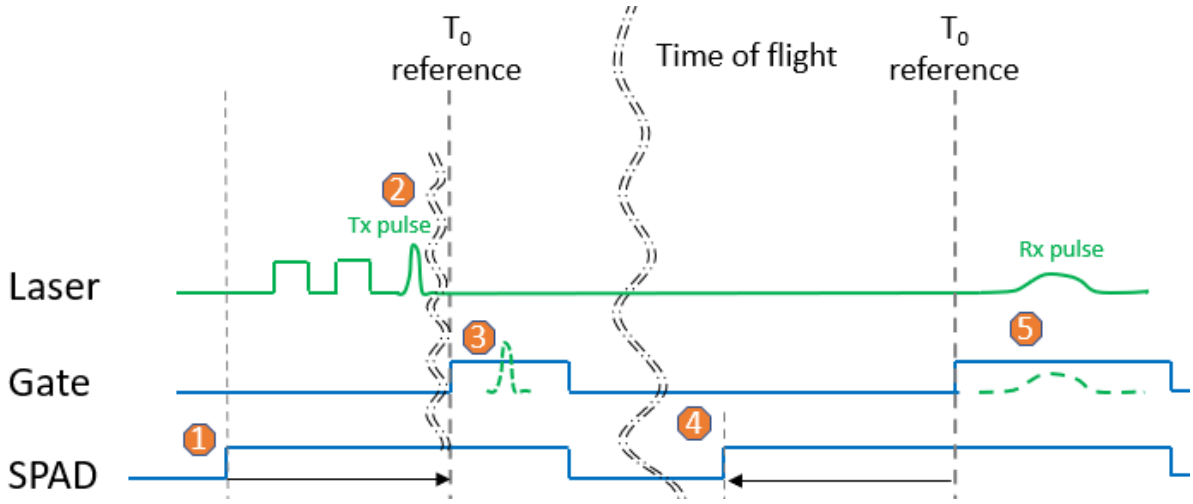

Figure 3.4: Detection principle for a SPAD. 1) The detector is activated; 2) The laser pulse is transmitted through the instrument; 3) The detector receives (a reflection of) the transmitted pulse and produces a voltage output, sampled by the gate to estimate the reference time; 4) After a predefined waiting time based on the TOF, the detector is again switched on; 5) According to the sampled reference time, the gate is activated and detect the returning pulse.

- NLA-4:

The laser footprint shall have a $1/e^2$ diameter in the range of 12.0 – 13.2 m from an altitude of 40 km.

RATIONALE: The optical design must expand the laser beam to reach the desired coverage on the ground, namely a 12 m diameter circle from a distance of 40 km. This parameter drives the FoV of the receiver, which is designed to match the size of the whole circle. By doing so, it is large enough to contain the entire illuminated scene, simultaneously minimising the background noise from non-illuminated regions.

In this context, the optical design must guarantee that the footprint size consistently exceeds the nominal value to compensate for potential misalignment in the optics not shared between the transmitter and receiver. This ensures that the minimum required area is constantly illuminated with enough margin to catch the detector and distribute the returning signal across as many SPAD as possible, increasing the likelihood of detection and capturing lateral variations.

This approach differs from the traditional one used for classical altimeters, e.g. BELA [28], where the APD continuously samples the footprint, which must remain entirely within the FoV to perform as many measurements as possible.

On the other hand, limiting the maximum footprint size is also crucial to minimising energy losses and, consequently, the laser source's power consumption. For this reason, a margin of 10% is accounted for.

- NLA-5:
  The transmittance of the transmitter and receiver paths shall be higher than 80%.
  RATIONALE: Although some optical components are shared due to the transceiver design, each option presents a particular arrangement that may affect the amount of light transmitted to the target and reaching back the detector. Again, the transmittance of the two optical paths affects the link budget equation and directly influences the required laser source's power level. Hence, assessing this aspect of the optical design is crucial to reducing the instrument's power consumption and increasing its capability for implementation in the CubeSat bus.

The following trade-off criteria, resumed in Table 3.2, have been derived from the listed requirements. They represent the concrete means to evaluate the different design options. The following list defines an explanation for the choice of the assigned weight and an outline of the verification strategy to quantify the performance of each design in each category.

Table 3.2: Trade-off criteria, originating requirements, and respective weight.

N.	CRITERION	REQ. CODE	WEIGHT
1	Compactness of the Arrangement	NLA-1 NLA-2	10
2	Tx-Rx Cross-Coupling	NLA-3.1 NLA-3.2	9
3	Footprint Size	NLA-4.1	8
4	Tx-Rx Coalignment	NLA-2.1 NLA-4.1	7
5	Transmittance Losses	NLA-5	6

- **Compactness of the Arrangement**
  - *Weight (10):* The project's primary goal is to prove the adaptability of traditional laser altimeters to miniaturised domains and the current limitations in this process. Consequently, the most suitable optical design must address this aspect.
  - *Verification strategy:* The evaluation of the compactness of the arrangement covers different details about the implementation of the optical elements and the interfaces between the optical system and other subsystems. In particular, the score is based on 1) the number of implemented optical elements, 2) the provisional surface extension of the optical system, including the mounting, 3) the total lateral margin between the optical system and the instrument's envelope, and 4) the minimum distance between the optical elements.

- **Tx-Rx Cross-Coupling**
  - *Weight (9):* Considering the novelty of SPAD in space applications, the determination of the amount of power density at the detector is paramount to demonstrate the survivability of the mission, as well as to guarantee the correct triggering of the pixels at the beginning of the measurements.
  - *Verification strategy:* The criterion will be assessed by numerical simulations of the laser beam's reflection from the lenses of the telescope to the detector, examining: 1) the shape of the reflection; 2) the power density level; 3) the possible overlapping with the detector.
- **Footprint Size**
  - *Weight (8):* As for the cross-coupling, determining the compliance of the footprint size with the desired requirements at the target is crucial to demonstrate the measurement's feasibility.
  - *Measurement strategy:* The criterion will be assessed by simulating the footprint size at 40 km for each design, checking: 1) whether each design exceeds the nominal value and 2) the design with lower energy losses.
- **Tx-Rx Coalignment**
  - *Weight (7):* Errors on the tilting, decentering, and distancing of the optical elements negatively affect the capability of the transmitter to illuminate the same FoV of the receiver. This can translate into signal power losses at the sensor, reducing the efficiency of the measurements. Nevertheless, this aspect is intrinsic in every optical design and affects only the quality of the measurement, not its success.
  - *Measurement strategy:* The criterion will be assessed by statistical analyses of the total fraction of energy lost due to possible offsets in the pointing of the transmitter and receiver.
- **Transmittance Losses**
  - *Weight (6):* Similar to the errors in the coalignment, the transmittance losses are ubiquitous in optical design and their impact will, therefore, be limited.
  - *Measurement strategy:* The criterion will be assessed by retrieving the transmittance of each optical element and computing the losses accumulated through the full optics.

3.3. Design Option Choices

3.3.1. Candidates

In a trade-off analysis, finding a candidate design that fully satisfies all the demands is impossible. For one reason or another, at least one detail will always deviate from the best-case scenario.

Hence, the strategy is to propose multiple design options that are not biased by the mission requirements but can still address the main problem. By doing so, creative solutions can arise and, even if not fitting with the current purpose of the project, be useful for further iterations of the same design or utterly new design development. Then, one needs to find and evaluate the most suitable candidates, based on their fit with the mission and the project constraints, and score the final solutions depending on their performance in the weighted criteria. Eventually, the option with the overall best fit is selected as the final design.

This process was also applied here, and the design options tree, presented in Figure 3.5, lists the possible solutions identified for providing a miniaturised laser altimeter.

The numbered boxes identify the investigated design choices. Simple sketches, presented in Figure 3.6, accompany the descriptions of each candidate. The legend is **L** - Laser; **D** - Detector; **RxM** - Receiver Mirror; **TxM** - Transmitter Mirror; **t** - Minor lens of the telescope; **T** - Major lens of the telescope; **m** - Minor mirror of the telescope; **M** - Major mirror of the telescope.

- Option 1: Transceiver, Direct Receiver
  This option is the most straightforward. Implementing a transceiver design, the laser beam (red) is pointed straight in front of the target, passing through a borehole mirror (RxM) and two diverging lenses (t and T). The same lenses focus the returning signal (blue) on the detector through the available surface of the deflected mirror.

- Option 2: Transceiver, Direct Laser Beam
  Option 2 iterates the previous design, modifying the arrangement of the receiver path. Indeed, an additional tilted mirror induces a second 90° deflection in the returning signal, making it again parallel to the initial direction.
- Option 3: Transceiver, 90° Deflection, Single Optical Plane
  The design is almost identical, but the laser beam is now deflected by 90° (TxM) during the expansion. This option attempts to save some length by allocating the laser accommodation transversely to the main optical path of the instrument.
- Option 4: Transceiver, 90° Deflection, Multiple Optical Plane
  It is the same case as Option 3, but here, the laser collimator is orthogonal to the main optical plane of the instrument. The laser beam is, therefore, exiting or entering the sheet.
- Option 5: Transceiver, 60° Deflection
  In this option, the laser beam is deflected by 60° (TxM), allowing the laser accommodation to be allocated to less of the instrument's width.
- Option 6: Transceiver, 45° Double Deflection
  This option implements two mirrors (TxM) to redirect the laser beam with a double 45° deflection. By doing so, it is possible to save a portion of the length of the instrument and better control the alignment of the laser beam.
- Option 7 and 8: Transceiver, Cassegrain and Gregorian Telescope
  This is still a transceiver design, but the main telescope is reflective and implements a primary and a secondary mirror. The difference between the two solutions lies in the geometry of the reflection generated by the two mirrors, but generally speaking, the overall arrangement is similar.
- Option 9: Differentiated, Lens telescope
  This option is the first to implement a differentiated optical path for the transmitter and the receiver subsystems. It has been the most common solution for laser altimeters in the past decades.
- Option 10: Differentiated, Two-mirror Telescope
  Similarly, this option presents two differentiated subsystems. In this case, the received signal is focused on the detector using a reflective telescope, like a Cassegrain or a Gregorian configuration.
- Option 11: Differentiated, Single-mirror telescope
  This last option implements a single-mirror telescope to collect the returning signal. The position of the detector is innovative concerning the previous cases because it interposes between the scene and a likely paraboloidal mirror.

The iteration of the transmitter design in options 2 to 6 could, in principle, be applied to the receiver design presented in option 1. However, a more robust iteration of transmitter configurations was preferred to profound changes in receiver configurations because of 1) the novelty of single-photon technology in this kind of application, which induces to avoid overcomplicated solutions, and 2) the more significant effort required to variate the receiver path, where the change in one single lens also propagates to the others, translating in a completely new combination.

3.3.2. Preliminary trade-off analysis

As mentioned, the listed design options encompass a branch of possibilities for the instrument that does not necessarily consider the mission's requirements. They are just possible solutions for the evaluated problem, but many of them are not compatible with the current scope of the instrument.
Consequently, further screening permitted the adaption of the design options to the studied case and the restriction of the candidates list. As visible in Figure 3.7, the process took two steps.

In the first one, the eliminated candidates were deemed unfeasible for the objectives of the current mission. According to requirements `NLA-1` and `NLA-2`, all differentiated options are incompatible with the possibility of being miniaturised within such a small volume while still meeting the desired performance and were subsequently rejected.

Instead, in the second step, the rejected candidates were considered not developable in the timeframe of this project, meaning that they may be able to address the problem but not in the desired amount of time or with the available resources. For example, Option 4 cannot advance to the next

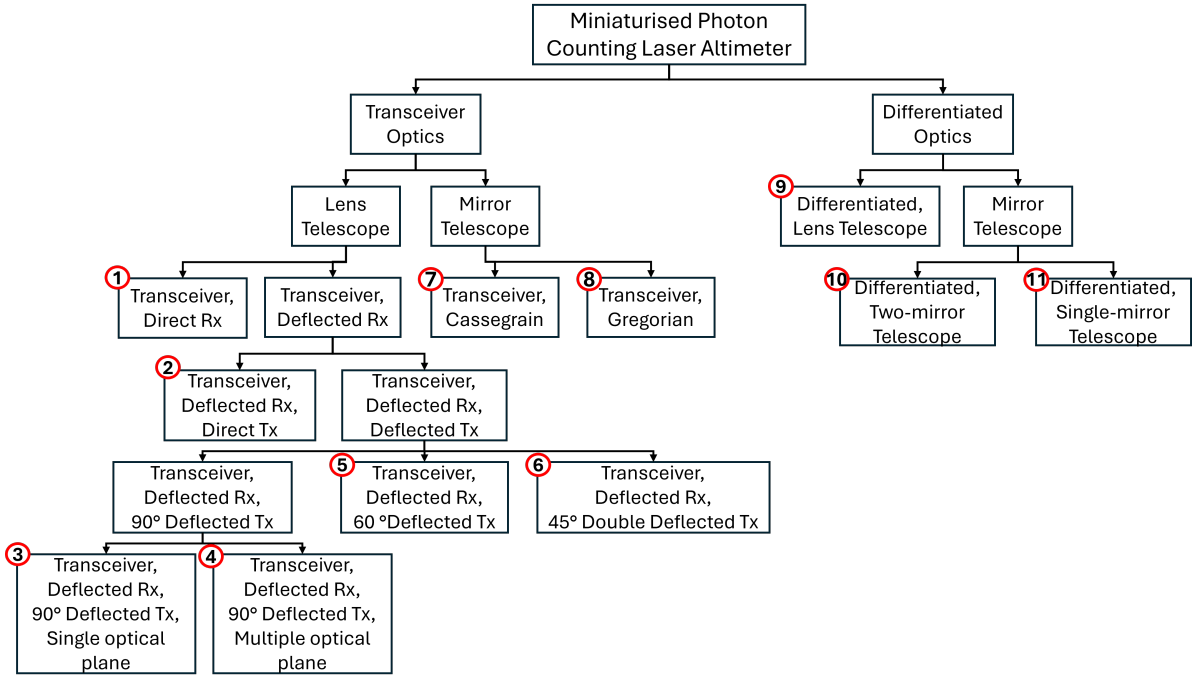

Figure 3.5: Design option tree for the miniaturized single-photon counting laser altimeter. The scheme breaks down from the generic concept into specific proposals encompassing different approaches. The numbered boxes represent the preliminary solutions that will be further analyzed.

phase because the arrangement of the other modules inside the instrument is still not detailed, meaning it is impossible to predict their exact position. A transversal laser source could conflict with their future adjustments; therefore, it can be adopted only at a further stage. On the other hand, Options 7 and 8 involve a complex optical system of two mirrors, which would require dedicated development and a meticulous manufacturing process, which does not fit in the time frame of this thesis. For Option 1, instead, the problem was identified while setting the optical simulations: with the available COTS described in Chapter 4, such a design would leave no room for the electronic interfaces of the sensor, due to the required distance between the lenses to focus the signal on the detector. Introducing tailored lenses may solve the problem, but this would exceed the time limits again.
Further iterations of the design exercise will determine whether these options could be reconsidered for the final instrument.

At the end, the remaining candidates that will be part of the final trade-off analysis are:

- Option 2: Transceiver design, direct laser beam
- Option 3: Transceiver design, 90° deflected laser beam, single optical plane
- Option 5: Transceiver design, 60° deflected laser beam
- Option 6: Transceiver design, 45° double deflected laser beam

The following section will detail the numerical models adopted to score the different design options and the results from the trade-off analysis.

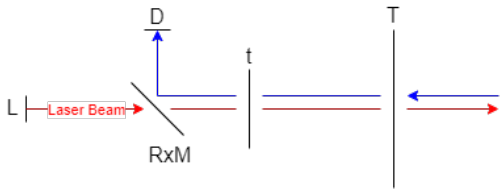

(a) Option 1: Transceiver, Direct Receiver

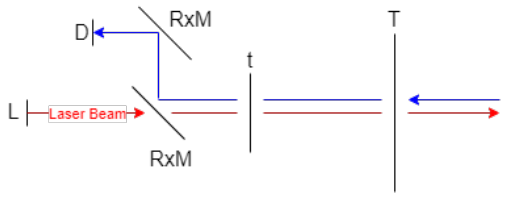

(b) Option 2: Transceiver, Direct Laser Beam

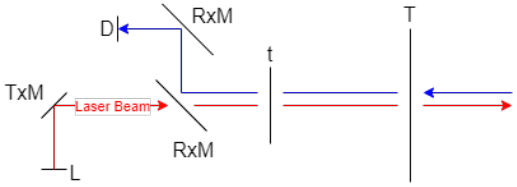

(c) Option 3: Transceiver, 90° Deflection, Single Optical Plane

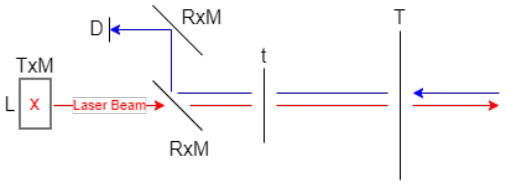

(d) Option 4: Transceiver, 90° Deflection, Multiple Optical Plane

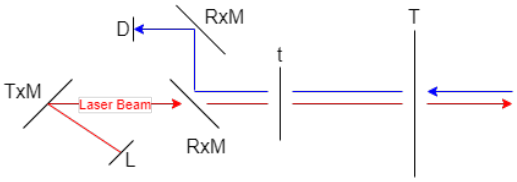

(e) Option 5: Transceiver, 60° Deflection

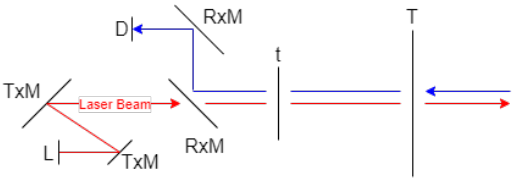

(f) Option 6: Transceiver, 45° Double Deflection

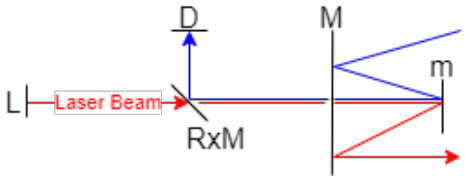

(g) Option 7 and 8: Transceiver, Cassegrain and Gregorian Telescope

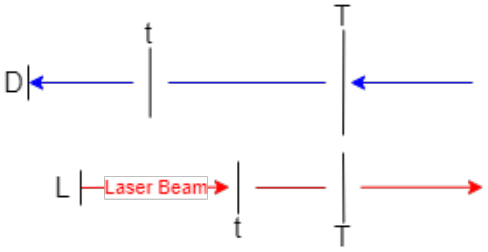

(h) Option 9: Differentiated, Lens telescope

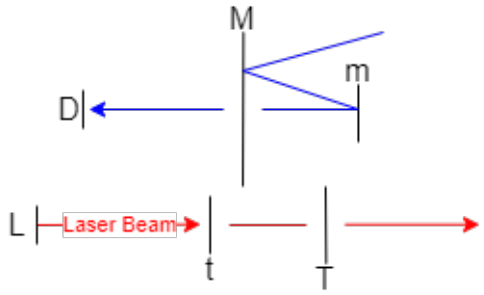

(i) Option 10: Differentiated, Two-mirror Telescope

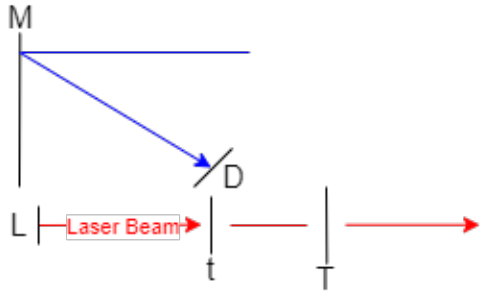

(j) Option 11: Differentiated, Single-mirror telescope

Figure 3.6: Sketches illustrating each design option. The red lines and arrows belong to the transmitter section, while the blue ones to the receiver section.

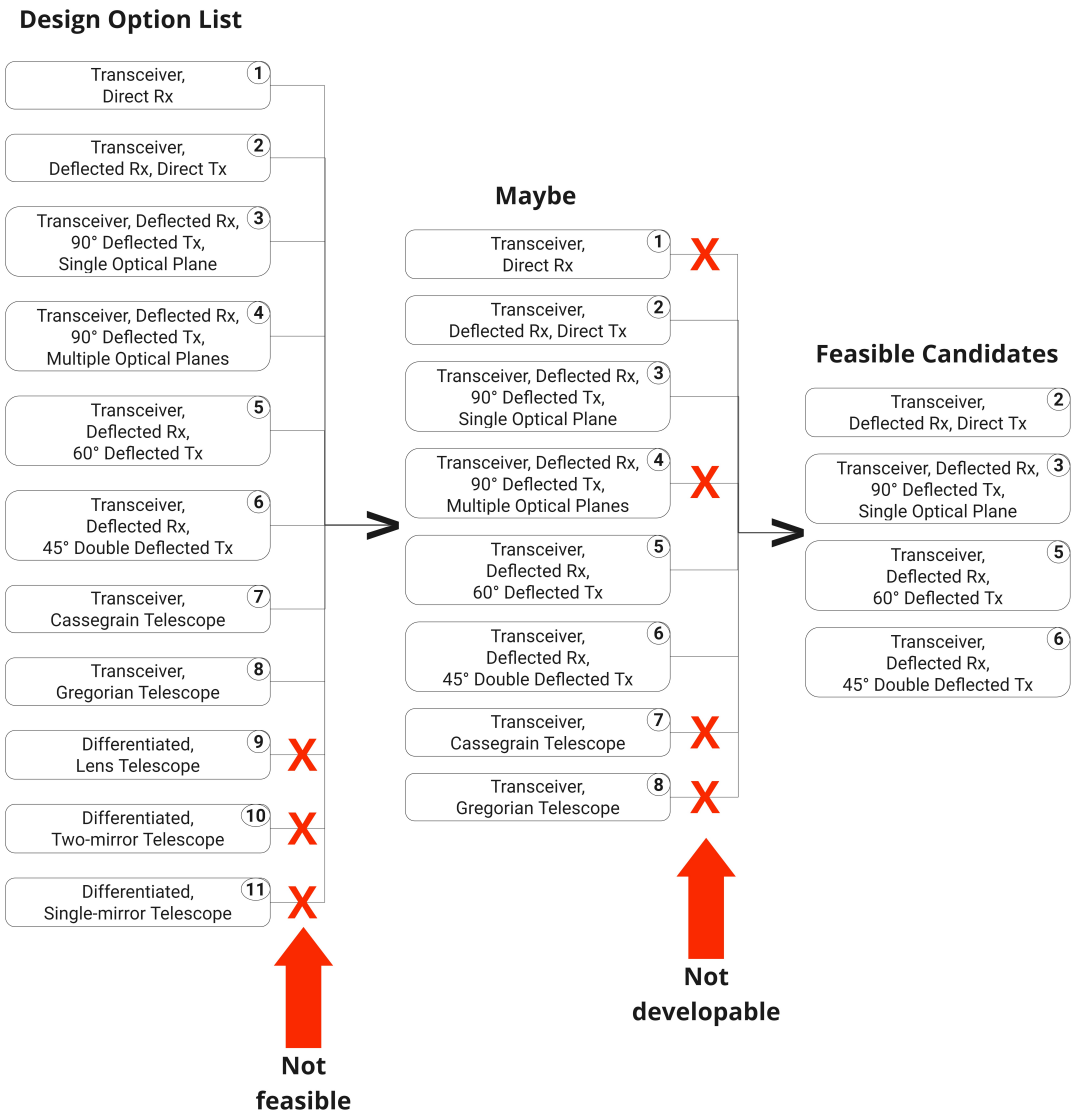

Figure 3.7: Initial trade-off process for selecting the best design candidates. The first screening process identified the not feasible options, namely options that are not compatible with the constraints of the current project. The second screening process identified the not developable options, namely options that are still valid but not fully explorable in the timeframe of the current project.

4

Trade-Off Analysis

This chapter details the scoring strategies applied to find the best candidate from the trade-off analysis introduced in the previous section. Using numerical simulations on the optical design software *Zemax*, the performance of the design options are assessed in each criterion. Eventually, the trade-off results delineate the instrument's final design.

4.1. Zemax Implementation

The first step to determining which optical design better suits this application's needs is implementing a standard benchmark in a simulation environment and successively iterating for each transmitter option. In this case, the more reasonable approach involved first optimising the shared receiver side to achieve the desired signal size at the detector and consequently branching the model according to the specifications of each candidate.
Considering that the lenses are picked from the catalogue of Thorlabs, Inc., their predefined geometrical and optical characteristics must compromise with size and optical constraints, requiring tuning the possible combinations of optical elements and their relative distance without forgetting to satisfy the instrument's desired performance.

Table 4.1: Resuming table for the receiver optical elements, listed in the order with which the received light passes through them. Note that the '-A' code stands for the type of anti-reflective coating applied to the lenses, which, in this case, acts over a 350-700 nm waveband that fits well with the 532 nm nominal wavelength of the laser.

Element	Diameter [mm]	Clear Aperture [mm]	Focal Length [mm]	Max. Thickness [mm]	Element Type	Material
AL75150-A	75	138	150	15	Asphere Lens	N-BK7
LD2297-A	25.4	>90%	-25	7.2	Bi-Concave Lens	N-SF11
PF07-03-P01	19	>17.1	[-]	6	Silver-Coated Mirror	Fused Silica
AL2550G-A	25	21.3	50	5.8	Asphere Lens	N-BK7
LB1014-A	12.7	>90%	25	3.4	Bi-Convex Lens	N-BK7

Going into the specifics of each component, the selection of the lenses was driven by different necessities. The telescope's main lens aimed to fit within the 10 x 10 mm^2 face of the instrument and, in the meantime, make the received light converge while occupying as little axial space as possible. Evaluated the alternatives, the choice fell on the first aspheric lens mentioned in Table 4.1, the AL75150-A. Its diameter of 75 mm and its positive focal length of 150 mm fit well with the mentioned needs. However, before reaching the detector, the light must be deflected by two folding mirrors, as shown in

the final design options. To have a more controlled reflection, it is common practice to collimate the incoming rays, namely making them parallel to the main optical axis of the instrument, and this was the main purpose of the bi-concave LD2297-A, the second lens. Its negative focal length, indeed, allows the rays to diverge and reach the first mirror almost orthogonally.
Once the beam is redirected, AL2550G-A and LB1014-A combine their focus capability to fit the spot size within the desired detector, a 3x3 SPAD squared array of 150x150 μm^2.

Figure 4.1 presents the resulting optical design for the receiver, for a total length of 172.346 mm, a total height of 80 mm, and an effective focal length of 154.542 mm.

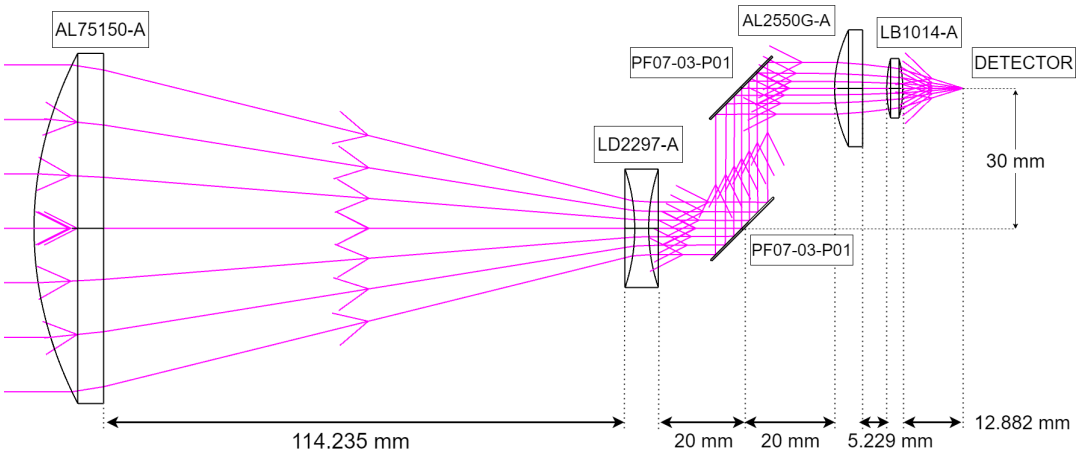

Figure 4.1: Receiver design resulting from the optical optimisation. The distance between each element is traced from its centre.

Nonetheless, the implementation of the lenses didn't come without drawbacks. Indeed, as visible on the left of Figure 4.2, the spot of the signal is too small with respect to the nominal size of the detector. By applying Equation 2.29, the current optical configuration would cover a squared surface at the ground with a size of roughly 19.5 m from 40 km of altitude, unsuitable to efficiently spread the signal across all the SPAD. Lenses with longer focal lengths were available from the manufacturer, but their diameter didn't fit in the space allocated for the receiver path.

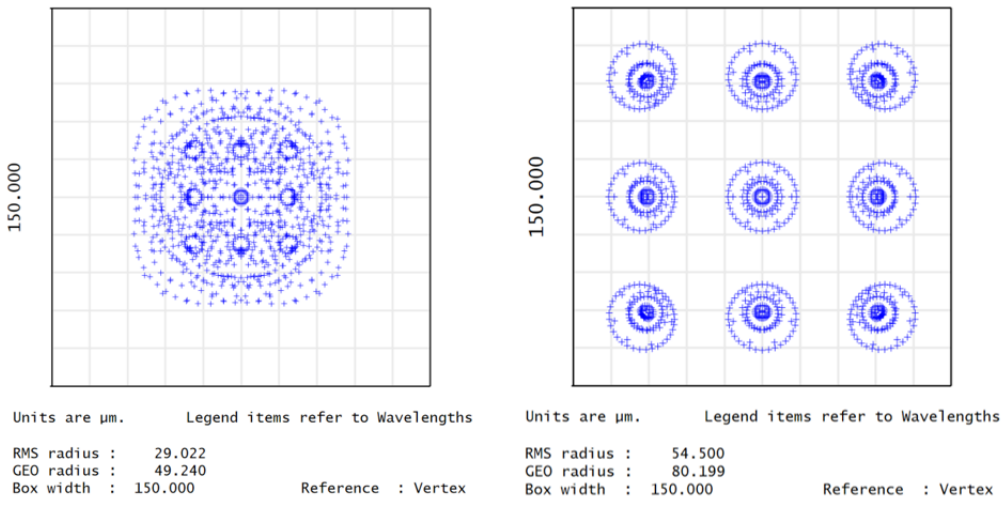

Figure 4.2: On the left: spot diagram for the optical configuration that will be tested during this project. On the right: spot diagram for an ideal configuration for the mission case. Definitions of relevant parameters: 1) Box width: the size of the detector that will fly on the mission; 2) Root-Mean Square (RMS) Radius: the square root of the distance between each ray and the central reference point squared and averaged over all the rays; 3) Geometrical (GEO) Radius: the distance from the reference point to the ray that is the farthest away from the reference point.

Despite this problem, the current configuration was still approved for further testing in the rest of the project because the mentioned detector is still in development and, therefore, will not be used for this thesis. At the moment of implementation in a flight model, the identified solution, which minimizes the number of changes to the design, implies the procurement of customised lenses to replace just the last two lenses of the receiver. By doing so, the rest of the optical design, shared by the transmitter as well, will stay untouched and valid for the nominal mission.

Using Zemax again, the specifics for these components were found through optimisation and are reported in Table 4.2, while the final spot size at the detector for the mission would resemble the right side of Figure 4.2. It's clear that the customisation of the lenses allows for a more uniform distribution over the sensor's active area, enhancing the clearness of the wavefront. However, in both cases, it's worth mentioning that the receiver was not designed to have diffraction-limited optics. The detection approach of SPAD, indeed, inhibits the possibility of recognising multiple events simultaneously, meaning that unresolved photons due to airy disks overlapping do not play a crucial role.

Table 4.2: Customised lens features divided by front and end surface. Note that in the case of ending surfaces, the thickness refers to the distance between that surface and the closest point of the following optical elements: the front surface of the last lens and the detector plane.

Lens	Surface	Type	Curvature Radius [mm]	Thickness [mm]	Material	Diameter [mm]	Conic constant
1	Front	Even Asphere	-225.615	4.000	N-BK7	14.000	-7094
	End	Standard	-6.216	6.370			-2.043
2	Front	Standard	-7.148	2.000	N-BK7	6.000	-0.741
	End	Standard	7.418	15.000			

Except for this aspect, the selected receiver design seems to have an acceptable optical performance. As evident from the left of Figure 4.3, indeed, even the enclosed energy at the detector presents a good distribution, reaching 100% well before the boundaries. Compared to the performance of the customised lenses on the right, the only difference is that the tailored lenses guarantee more uniformity over the FoV. In contrast, COTS lenses are more sensitive to the light coming from the edge.

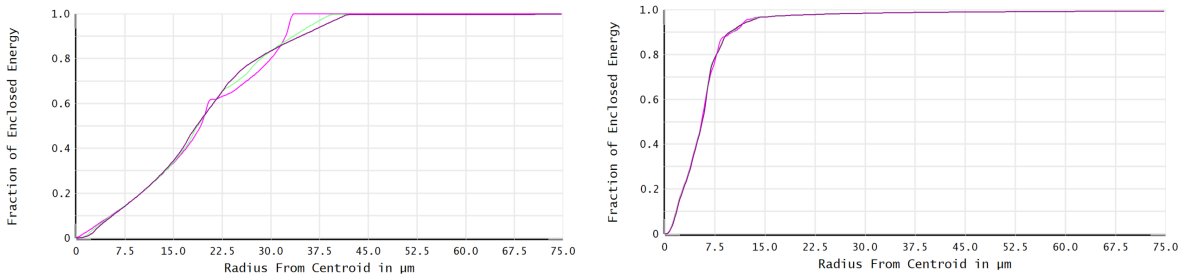

Figure 4.3: Distribution of the optical energy with respect to the distance from the centre of the detector. On the left, results from the COTS design that will be studied in this project. On the right, from the customised receiver setup for the mission. The different colour lines refer to different angular positions in the instrument's field of view.

About the transmitter designs, each of them was first arranged in a separate simulation environment and then integrated with the receiver. Figure 4.4 presents the sketches of the arrangements, including the distances between the optical elements.

In each case, it was assumed a 4x1 cm^2 surface for the laser fibre coupling, an initial laser beam waist radius, divergence, and quality factor of 0.15 mm, 2.6 mrad, and 1.3, respectively (according to the current capabilities of the main laser supplier of the institute, the Fraunhofer Institute for Microelectronic Circuits and Systems (IMS)), and a borehole in the shared mirror of the receiver that let the laser beam pass through the element while deflecting the returning signal toward the detector. Each design option fits in the 2 U allocated to the optics.

Regarding the expansion performance of the design options, Figure 4.5 shows the footprints of the laser beam as they would appear on a 40 km away target. Moreover, according to the mission proposal, the laser shots' initial energy is 2 mJ. This can be translated into an initial peak power of 376 kW using Equation 2.27, which was used as input to evaluate the power density of each candidate at the target.

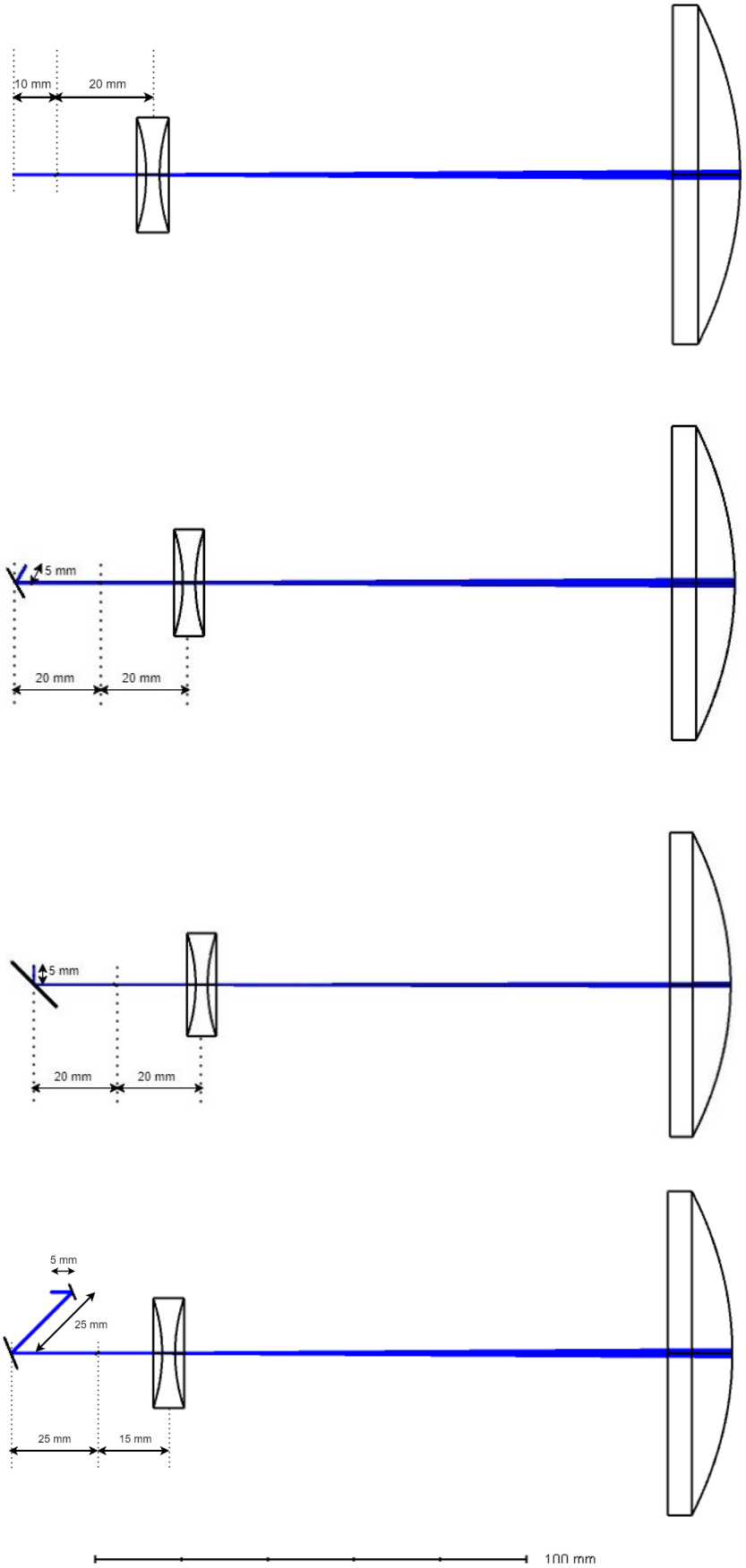

Figure 4.4: Transmitter design options implemented in Zemax with relative positions of the secondary optical elements. From the top to the bottom: direct laser beam, 90° deflected laser beam with single optical plane, 60° deflected laser beam, 45° double deflected laser beam. Please note that possible variations in the dimensions of lenses and mirrors are just due to visualisation and export formatting. The element on the left of the telescope's second lens, not clearly visible from the sketches, is the borehole mirror.

Table 4.3 resumes the data in Figure 4.5. Naturally, the peak in power density increases when the footprint size decreases since the energy is distributed over a smaller area. This confirms the urge to keep the footprint as close as possible to the required value, as mentioned by requirement NLA-4.

Table 4.3: Resuming table of the footprint specifics of the different design options.

Candidate	Footprint Radius [m]	Max. Power Density [mW/mm2]
Direct	6.9231	4.99
60°	6.7209	5.39
90°	6.6206	5.39
45° d.d.	6.1290	6.29

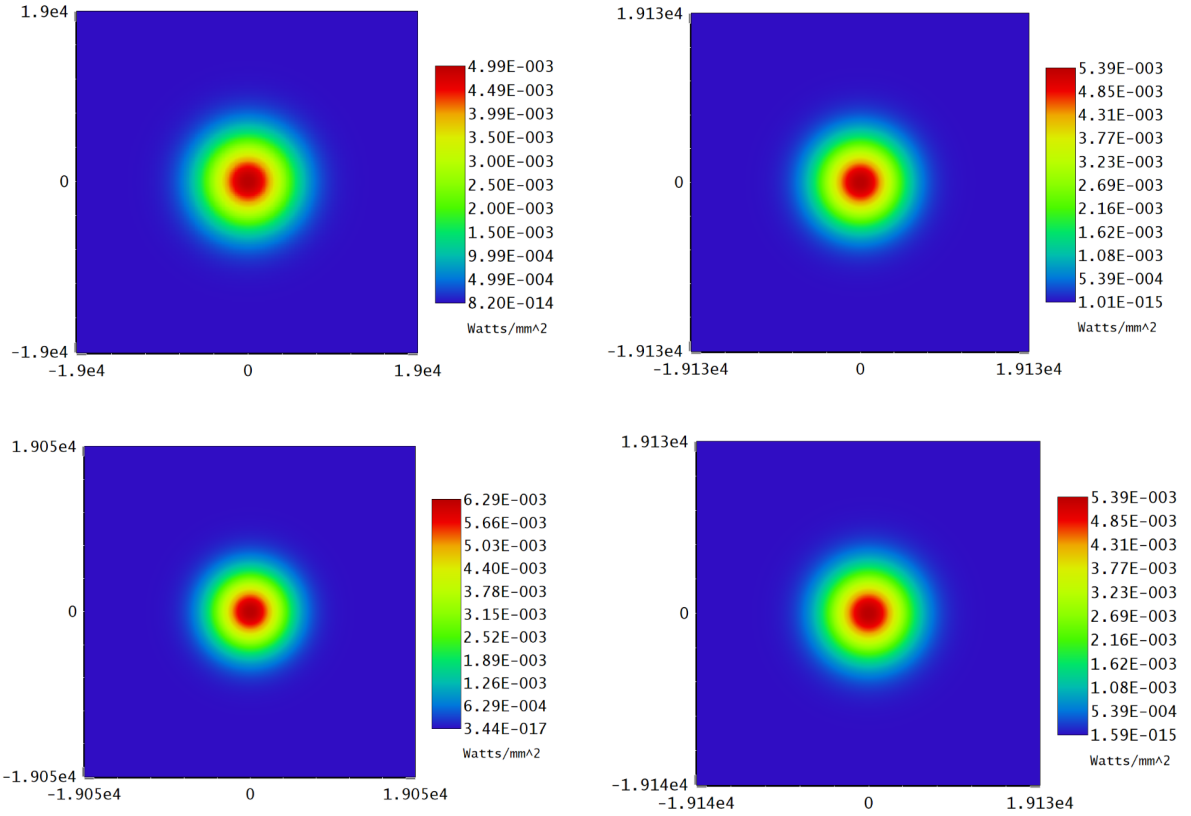

Figure 4.5: Footprint size and intensity at 40 km for each transmitter design, considering a 2 mJ laser beam. The axes of every plot are in mm. From the top left, in an anticlockwise order: direct laser beam, 60° deflected laser beam, 90° deflected laser beam with single optical plane, 45° double deflected laser beam.

The scoring process for each candidate in each trade-off criterion and the results from the trade-off analysis will be presented in the next sections.

4.2. Trade-Off Analysis

4.2.1. Compactness of the arrangement

Since each candidate is expected to fit within the 2 U defined by the requirement, the evaluation of this criterion is based on predicting the implementation easiness for the optical elements. This encompasses a few variables: 1) the number of optical elements, which increases the complexity of the system; 2) the provisional covered surface, which reduces the space available for other subsystems; 3) the total lateral margin from the instrument's case, which reduces the possibility to increase the distance between optical elements in case of required adjustments; 4) the minimum distance between

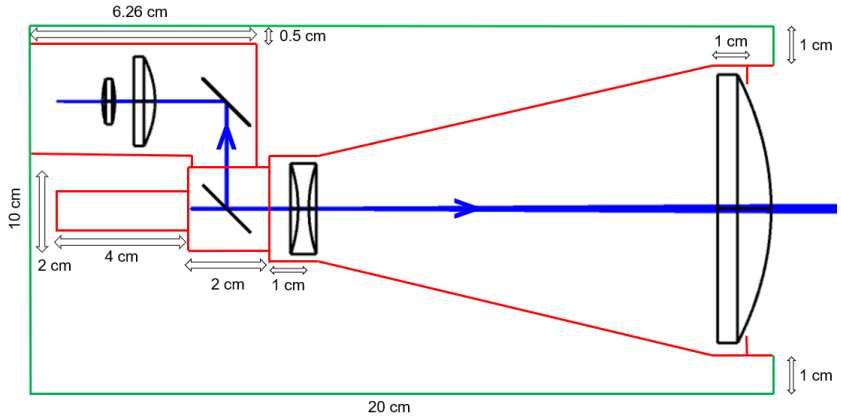

(a) Option 1: Direct laser beam

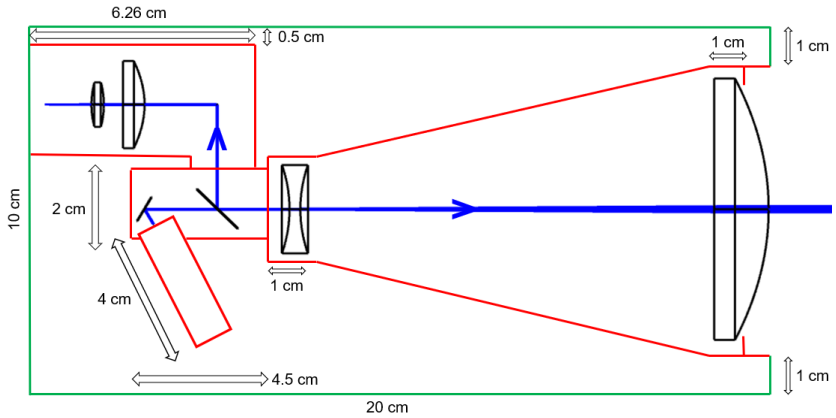

(b) Option 2: 60° deflected laser beam

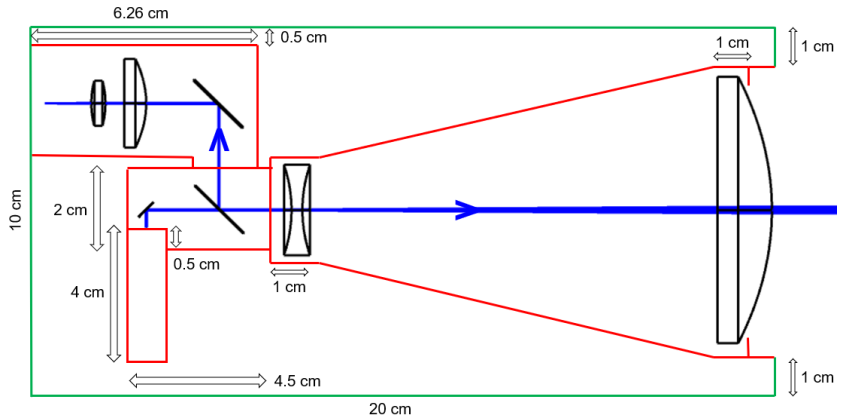

(c) Option 3: 90° deflected laser beam with single optical plane

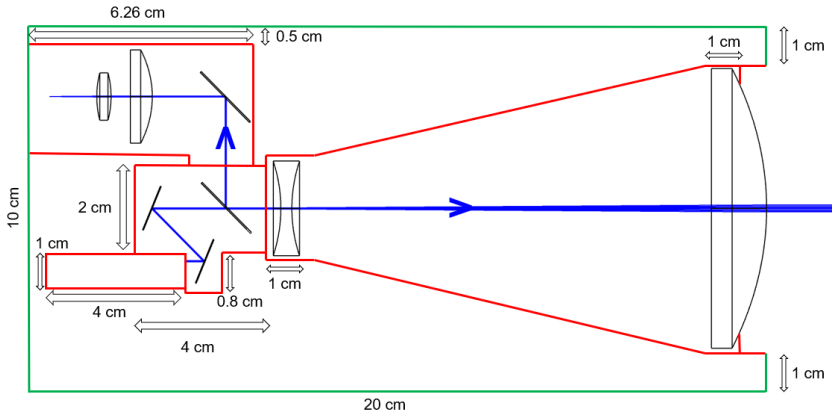

(d) Option 4: 45° double deflected laser beam

Figure 4.6: Sketches for plausible mounting dimensions for each of the final candidates.

optical elements, which determines the complexity in the mounting process. Figure 4.6 shows each design option's approximated definition of the mounting dimensions.

The final assessment of the criterion is reported in Table 4.4. The direct laser beam implements fewer elements and covers less surface, gaining the highest score for this criterion. On the other hand, the 45° double-deflected laser beam performs worse in almost every category. The 60° candidate does not excel in any of the cases, while the 90° has the lower lateral margins. However, all the options were graded above the sufficiency because, as mentioned before, they did not fail to match the size requirements for the optical system.

Table 4.4: Assessment for the criterion: Compactness of the Arrangement. The green boxes highlight the better-performing candidate in each category only in the cases without ex aequo. The yellow boxes, instead, highlight the worst-performing candidates in each category.

Design Option	Number of optical elements	Covered Surface [cm2]	Total lateral margin [cm]	Minimum distance between opt. elements	Score
Direct	7	91.02	1.5	2.0	10
60°	8	96.02	1.5	2.0	9
90°	8	96.02	1.0	2.0	8
45° d.d.	9	97.66	1.5	1.5	7

4.2.2. Tx-Rx cross-coupling

Two dedicated numerical models were developed in Zemax to simulate the coupling between the laser shots and their reflection on the detector. Figure 4.7 reports their main features.

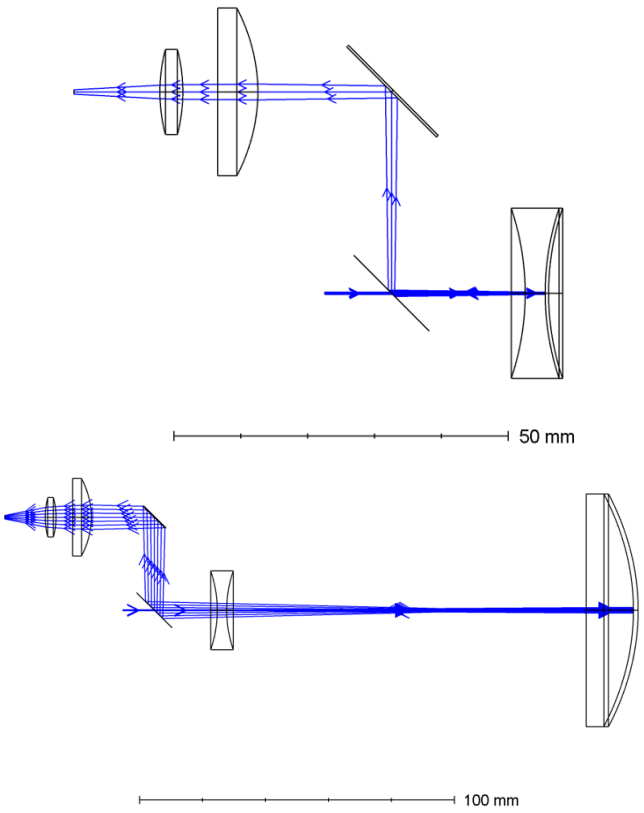

Figure 4.7: Stray light models to reproduce the reflection from the front surfaces of lens LD2297-A (on the top) and lens AL75150-A (on the bottom). In this case, the direct laser beam candidate is represented.

For each design option, a fictitious mirror surface was introduced at the same position and with the same reflection properties as the evaluated lens surfaces. Thorlabs does not publicly disclose the

properties of the optical coatings applied to the lens. Still, they are available in Zemax and are used for the current simulations, making the results valid and close to reality.

In building these numerical models, the rear surfaces of the lenses (meant as the back surface of the lenses for the light entering the telescope from outside) were not evaluated as contributing to reflections because this scattering is uniformly dissipated in all directions. On the contrary, the reflections on the front surfaces are focused from the lenses to the detector, becoming relevant for the assessment. Similarly, the reflections on the mounting walls are not implemented in these models because they were considered to be of a lower, negligible order of magnitude.

In this context, another factor was the size of the borehole in the receiver's first mirror. For the direct, 60° deflected, and 90° deflected configurations, the hole has an elliptical shape (as seen from the same point of view of the laser beam) of 0.9 mm x 1.3 mm. In the other case, i.e. the 45° double deflected configuration, the size of the hole is slightly increased to 1.0 x 1.4 mm. These dimensions are not optimised for each specific case but were iteratively changed until the symmetry of the beam footprint at the target was granted up to millimetres.

Figures 4.8 and 4.9 show the irradiance pattern derived from the reflection on lenses LD2297-A and AL75150-A, respectively. The irradiance levels derive again from the initial laser power of 376 kW calculated using Equation 2.27. The highlighted squares in each plot define the nominal size and position of the detector (red squares, Figure 4.8) or the maximum extension reachable by the detector in the case of implementation of active shifting techniques for the detector's position (black squares, Figure 4.9). In the latter case, the red square still defines the nominal position.

Additional information about this will follow in Section 4.2.4.

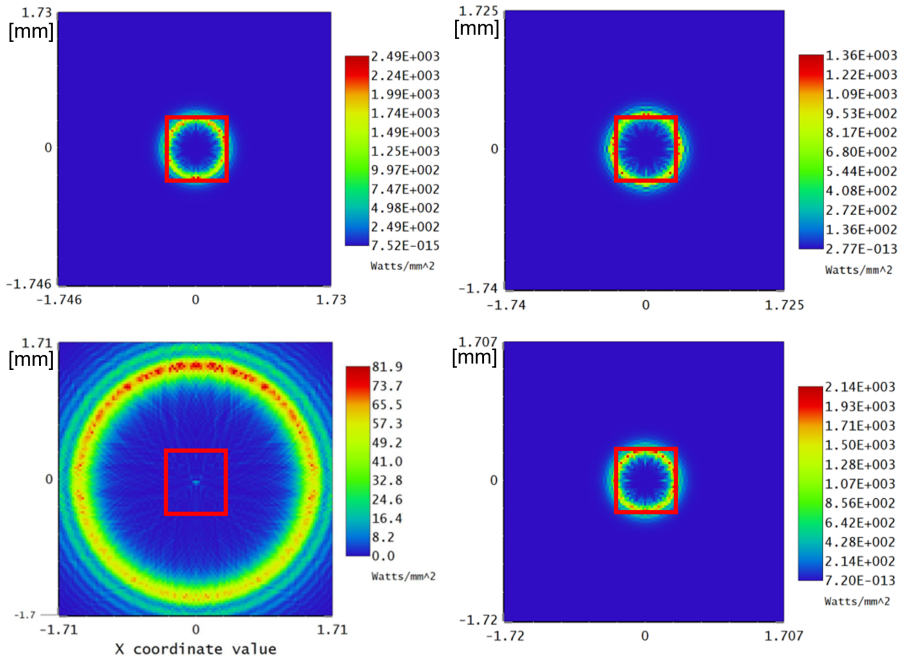

Figure 4.8: Irradiance distribution of laser pulses reflected from the first lens of the telescope (LD2297-A) on the detector. The red squares represent the maximum extension of the pixel array in the case of active position adjustment for misalignment correction. From the top left, in an anticlockwise order: direct laser beam, 60° deflected laser beam, 90° deflected laser beam with single optical plane, 45° double deflected laser beam.

The peak irradiance values at each simulation's nominal and boundary positions are reported in Tables 4.5 and 4.6. Compared to the threshold cited by requirements NLA-3.1 and NLA-3.2, which is 200 kW/mm^2, the power density levels are well below the survival threshold. Nevertheless, since this value comes from a standard CMOS technology that is not operated with single photon sensitivity and seen the lack of official values from the manufacturer, the scoring process rewards the candidates with the relatively lowest radiation levels. Although highly conservative, this strategy prevents damage from accumulated exposure in the instrument's one-year operations.

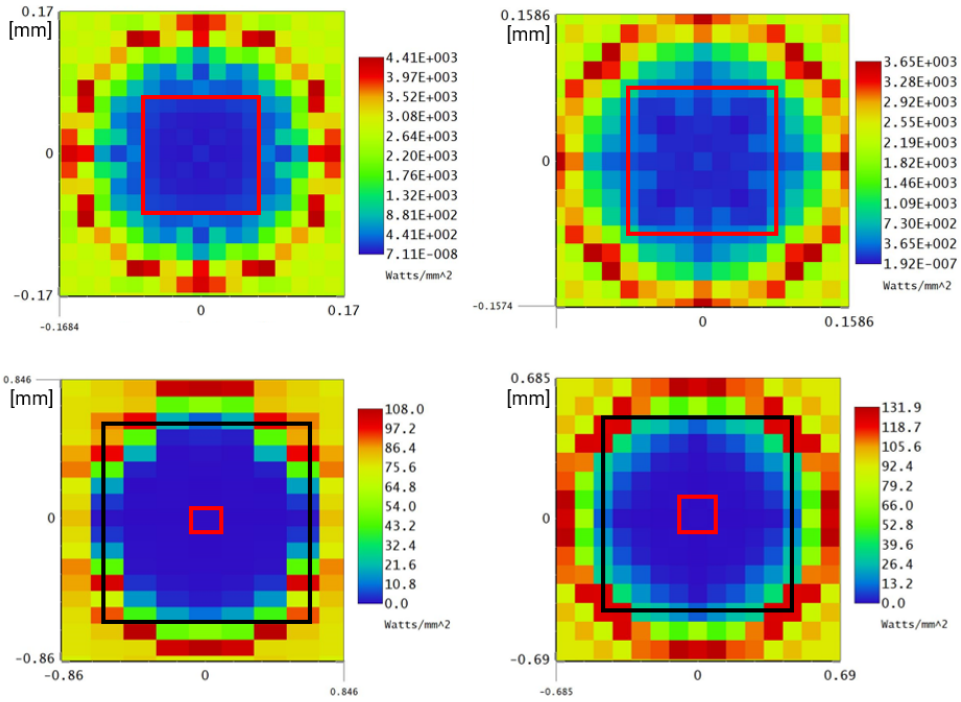

Figure 4.9: Irradiance distribution of laser pulses reflected from the second lens of the telescope (AL75150-A) on the detector. The red squares represent the nominal size and position of the detector, while the black squares represent the maximum extension of the pixel array in the case of active position adjustment for misalignment correction. From the top left, in an anticlockwise order: direct laser beam, 60° deflected laser beam, 90° deflected laser beam with single optical plane, 45° double deflected laser beam.

Table 4.5: Peak irradiance levels after reflection on the lens LD2297-A for each design option, with the corresponding score. This result contributes to half of the final score in this category.

Design Option	Maximum Irradiance at the detector (nominal position) [W/mm^2]	Maximum Irradiance at the detector (maximum extension) [W/mm^2]	Score (50%)
Direct	1024	2490	4
60°	505.9	1360	6
90°	925.5	2140	4
45° d.d.	16.6	16.6	10

Table 4.6: Peak irradiance levels after reflection on the lens AL75150-A for each design option, with the corresponding score. This result contributes to half of the final score in this category, reported in the last column.

Design Option	Maximum Irradiance at the detector (nominal position) [W/mm^2]	Maximum Irradiance at the detector (maximum extension) [W/mm^2]	Score (50%)	Previous Score (50%)	Final Score
Direct	882	4406	4	4	4
60°	915	3648	4	6	5
90°	0.4554	123.9	10	4	7
45° d.d.	0	102	10	10	10

4.2.3. Footprint size

Combining the results presented in Table 4.3, Figure 4.10 overlaps the footprint size of each candidate. All the design options fulfil the minimum footprint size requirement of a 6 m radius. However, the straight and the 60° deflected laser beam configurations exceed the 10% threshold for the maximum

footprint size. An insufficient score reflects their noncompliance with the requirement. The 90° deflected laser beam is just above the threshold, but the margin can still be considered inside the computational uncertainties of the simulation and, therefore, is negligible.

Table 4.7 exposes the percentage margins on the nominal value and the corresponding score for this criterion.

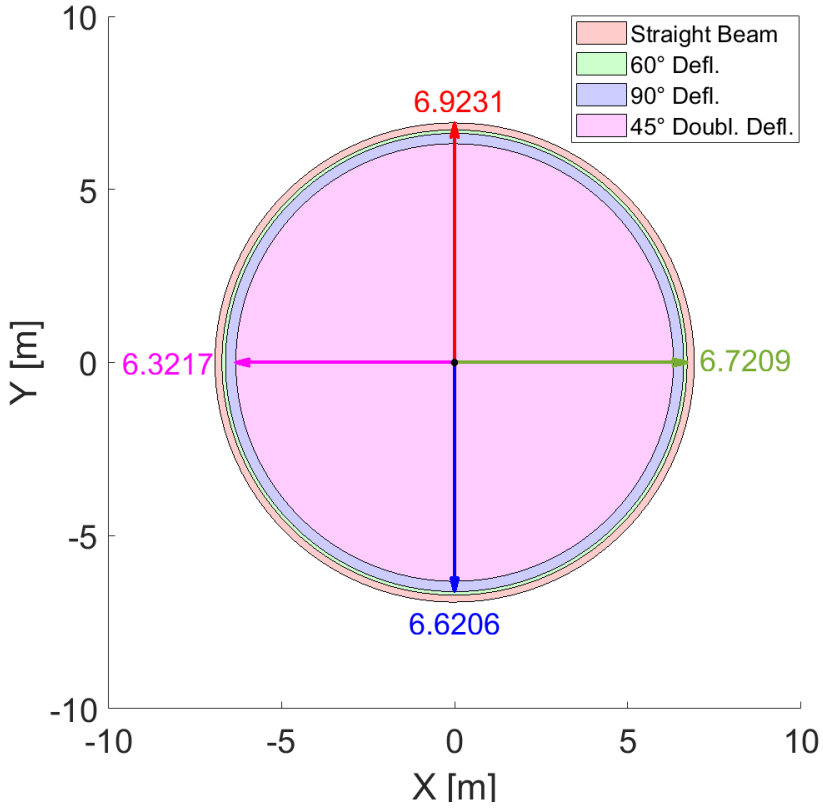

Figure 4.10: Footprint size at 40 km distance for the different candidates.

Table 4.7: Footprint size for the different design candidates.

Design Option	Margin from nominal radius value	Final Score
Direct	15.4%	4
60°	12.0%	4
90°	10.3%	6
45° d.d.	2.1%	10

4.2.4. Tx-Rx coalignment

The evaluation of this criterion required two different steps:

- Perform a tolerance analysis on the design options to calculate a possible offset between the centre of the instrument's FoV and the centre of the footprint on the 40 km distance target;
- Perform a second tolerance analysis on the design options to identify the signal power lost at the detector plane due to the previously calculated offset with the transmitted signal.

Both the processes required Monte Carlo simulations to combine possible tilting (0.001 deg), centring (0.2 mm), and distancing (0.2 mm) errors of the optical elements. These tolerances were picked from the limitations of the institute's manufacturing facilities. Moreover, to reduce the simulations' computational time, the offset was evaluated as the total distance from the centre without considering its

orthogonal components. Consequently, it's the most conservative scenario, intended as the maximum possible offset with which the signal can reach the target.

For the first part of the assessing process, 200 Monte Carlo simulations gave back the mean deviation from the centre and the RMS uncertainties that are displayed in Figure 4.11. These results, in addition to the maximum expected value from the 90% of the Monte Carlo simulations and a normalised deviation from the total footprint size in each case, are resumed in Table 4.8.

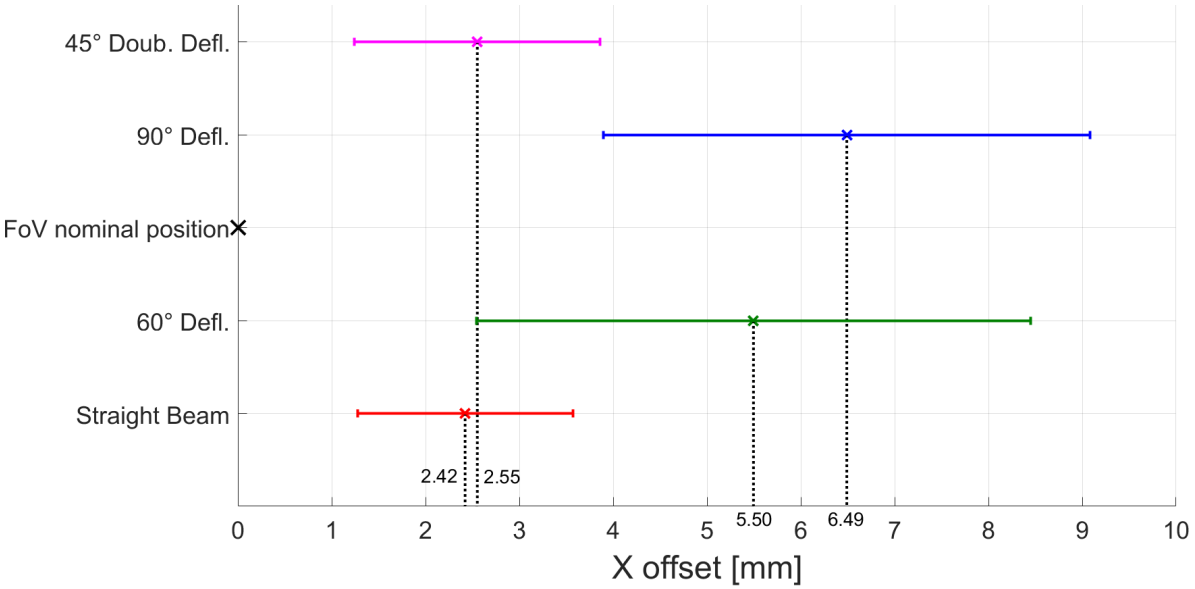

Figure 4.11: Offset in the coalignment between the FoV of the instrument and the footprint of the laser beam generated by the different transmitter iterations. Please note that the vertical offset is not significant for the plot and was used just to spread the results over the graph.

Table 4.8: Resumed results from the Monte Carlo simulations addressing the possible offsets at the target.

Design Option	Expected Offset (Mean) [mm]	RMS margin [mm]	Expected Offset (90%) [mm]	Normalised Variation [%]	Score (50%)
Direct	2.42	1.15	3.96	0.06	10
60°	5.5	2.9	9.6	0.1	7
90°	6.5	2.6	10.9	0.2	6
45° d.d.	2.6	1.3	4.4	0.07	10

For the second part of the assessing process, 1000 Monte Carlo simulations were performed. As initial input, it was added an angular offset to the centre of the signal received by the instrument equal to the maximum expected value from the 90% of the Monte Carlo simulations of the first phase. This value permits the assessment of the worst-case scenario and is more conservative.
However, even with a perfectly centred footprint, the receiver design has an intrinsic inclination to misalignment that must be considered. This implies the possibility of an offset in the signal position on the detector plane with respect to the centre of the detector (the black dot in Figure 4.12), even in an ideal case where no errors were performed while sending the signal. For this reason, a preliminary simulation was conducted to evaluate the positioning boundaries of the detector, shown in Figure 4.12 within the red lines. These boundaries (valid only on the horizontal axis for the same assumption applied in the previous case) were used to identify the maximum detector extension also used in Figures 4.8 and 4.9.

The final results, derived from the percentages of signal power dissipated at the detector plane, are presented in Table 4.9. The reference results are the mean of all the Monte-Carlo simulations, but also the worst-case value enclosing the 98% of the simulations was included for completeness. The dissipated signal power was computed based on the fraction of the area that is expected to go outside the maximum positioning boundaries of the detector, namely the sum of the blue line (central position

plus RMS error) and the pink line (half of the detector array, extending from the centre).

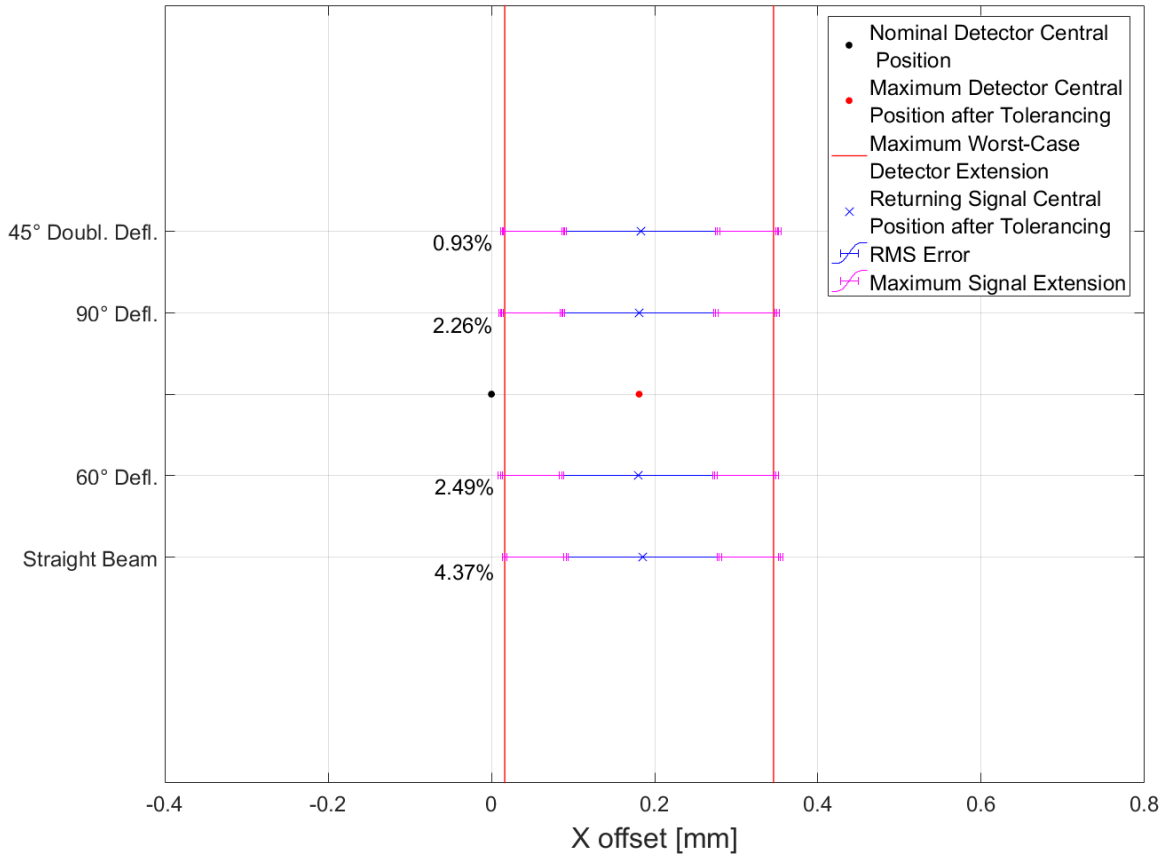

Figure 4.12: Coalignment budget of each design option. The percentage values represent the total signal power dissipated at the detector plane.

Table 4.9: Resumed results from the Monte Carlo simulations addressing the possible offsets at the detector. The final score for this criterion is also reported.

Design Option	Expected Offset (Mean) [μm]	RMS margin [μm]	Maximum dissipated signal power [%]	Score (50%)	Previous Score (50%)	Final Score
Direct	185.2	96.7	4.37	6	10	8
60°	179.9	93.7	2.49	9	7	8
90°	180.6	94.3	2.26	9	6	7
45° d.d.	182.7	91.2	0.94	10	10	10

The final score is based on the previous results at the target (distance from the centre of the FoV and width of the uncertainty bar) and the final results at the detector (amount of energy lost outside the pixel array).

This criterion does not directly respond to a performance requirement, but it's meant to reflect the interconnection between transmitter and receiver regarding error propagation in a transceiver design. Additionally, the few percentage points of signal losses may seem insignificant. Still, they must be contextualised into the detector's single-photon sensitivity, where every single photon contributes to confirming the detection of the actual laser pulse. Indeed, this kind of detector uses comparative (or voting) algorithms, where detection is assumed genuine only when more than a certain threshold of SPADs is triggered. It is, therefore, critical that as many photons as possible fall inside the detector.

4.2.5. Transmittance losses

Most of the optical elements used for this design exercise are shared among the different design options. There are slight variations in the number of elements and also in the dimension of the borehole in the first deflecting mirror of the receiver, and these will be the parameters that will influence the difference in scoring for this criterion.
To find the transmittance of the lenses, data from the Schott datasheet of N-BK7 [63] and N-SF11 [64] at the working wavelength of 532 nm are retrieved. However, these data are based on a reference thickness, which is not necessarily the same as the used lenses. For this reason, the correct transmittance was calculated using the following equation [65]:

$$\tau_{i2} = \tau_{i1}^{(d2/d1)}$$

where τ_{i2} and τ_{i1} refer to the transmittance through the lens substrate at the new and at the reference thickness, respectively reported as $d2$ and $d1$. In addition, the transmittance of the Thorlabs coating was taken into account and multiplied twice, once for side, with the transmittance of the substrate. The results of these calculations are reported in Table 4.10.

Table 4.10: Transmittance of the optical elements implemented in the design.

Element	Substrate Transmittance	Coating Transmittance	Total
AL75150-A	0.997	0.995	0.9870
LD2297-A	0.9973	0.995	0.9873
AL2550G-A	0.9988	0.995	0.9887
LB1014-A	0.9993	0.995	0.9893
PF07-03-P01	0.978	-	0.978
NB05-K12	0.999	-	0.999
Band-Pass Filter	0.5945	-	0.5945

Regarding the other optical components, such as the mirrors, the reflectance value at 532 nm indicated in the Thorlabs catalogue is applied. In this case, NB05-K12 is the mirror specialised in reflecting the 532 nm Nd:YAG laser implemented in the transmitters with deflections.

An additional element, a band-pass filter, must also be inserted in the optical arrangement to cut off the background noise and let only the light in a narrow range reach the detector.

The final transmittance for each design option, computed by multiplying all the required contributions from above, is reported in Table 4.11, along with the score for this category. A last contribution was also included: it is the amount of surface available on mirror PF07-03-P01 for each design option due to the presence of the borehole.

Table 4.11: Final results for the transmittance of each design option.

Design Option	Borehole Transmittance	Final Transmittance	Score
Direct	0.9935	0.5508	10
60°	0.9935	0.5502	10
90°	0.9935	0.5502	10
45° d.d.	0.9923	0.5490	10

The candidates' transmittance differences are negligible and must be scored equally. Still, the assessment of this criterion permitted the identification of a critical component, namely the band-pass filter. Since this part is also a COTS, the band is not exactly centred at the precise wavelength of the laser available in the lab, 532.05 nm, but at 532.135 nm. This explains the low value reported in Table 4.10, which does not meet the instrument's transmittance requirements. Nevertheless, this value must be considered provisional until laboratory tests, when it will be possible to tune the tilting of the filter to increase its transmittance at the specific wavelength.

4.3. Trade-Off Results

At the end of the trade-off analysis, a Pugh matrix (Table 4.12) was populated to summarise the results and identify the most suitable candidate.
Considering that the straight and 60° deflected laser beams didn't match the required footprint size range, they cannot be considered for the final choice. The winning design option, therefore, is the one with the overall better performance between the 90° and the 45° double deflected laser beams. In this case, the latter configuration for the transmitter is identified as the best for this case study.
This outcome is surprising if one thinks about a system with more components, which should be more prone to errors and losses. Nonetheless, this particular configuration could have performed better for a bunch of reasons:

- The presence of two mirrors to steer the laser beam compensates for possible coalignment errors. This happens because the misalignment in one element is likely attenuated by an opposing misalignment in the other, causing a better performance in the Monte Carlo simulations. When implementing a single mirror for redirecting the laser beam, this behaviour doesn't manifest, resulting in increased offset at the target.
- Due to the volume constraint of the instrument and the implementation of COTS elements, the capabilities of the laser beam expansion are limited. The 45° double-deflected setup adapted better to these limitations, providing a footprint size at the target that is extremely close to the requirements, with a low 2.1 % margin accounting for the misalignment errors. This value ensures low power losses while maintaining a safety margin during operations.
- The laser beam expansion also influenced the internal reflections of each configuration. Indeed, depending on the size of the beam at each lens of the telescope, the back reflection was different. Consequently, the diffraction effect gained by passing through the borehole was also different. In this sense, the slightly larger borehole in the 45° double-deflected configuration and the lower distance between the shared mirror and the last lens of the telescope contributed to a shallower irradiance level at the detector, minimising the chance for accumulated damage to the SPAD.

Table 4.12: Resultant Pugh Matrix after the Trade-Off Analysis. The coloured boxes indicate some key performance: green boxes underline the outstanding candidate in some of the criteria, while the yellow and orange ones identify, respectively, barely sufficient and critical results. The absence of red boxes, namely insufficient performance, shows that none of the candidates failed to satisfy the requirements.

	Straight Beam	60° Deflection	90° Deflection	45° Double Deflected	Weight
Compactness	10	9	8	8	10
Cross-coupling	4	5	7	10	9
Footprint	4	4	6	10	8
Coalignment	8	8	7	10	7
Transmittance	10	10	10	10	6
TOTAL SCORE	284	283	300	380	
RESULT	3rd	4th	2nd	1st	

Even if the scoring process has been conducted objectively, the method applied during this research may present some limitations.

One example may be the cross-coupling simulations. In the 45° double-deflected configuration, the shorter distance between the last lens of the telescope and the shared mirror is due to the additional space required for accommodating the laser fibre. This shorter distance may have affected the internal reflections, shifting their focus further from the detector plane and improving the candidate's performance in this criterion. In contrast, the other configurations, which allowed for a larger distance to simplify implementation, may have underperformed. However, reducing this distance in those candidates also decreases their compactness scores, balancing with the lower result of the 45° configuration in that category.

Nonetheless, the final score underlines a marked gap between the first-placed design and the other configurations. Unless critical showstoppers are identified in the test campaign, further iterations of this trade-off will not be required at this development phase.

The 45° double-deflected configuration will be developed in the next chapter in a prototype to be tested in the lab using a CAD (Computer Aided Design) software.

5

Test Campaign Preparation

This part of the report shows how the laboratory setup was prepared to assess the performance of the optical design, focusing on the CAD models developed in CATIA to manufacture the instrument's case.

5.1. Overview

After identifying an optimal optical design for the instrument, it's time to assemble it.

It is essential to provide a structure where the optical elements can be fitted to first characterise the performance of such a prototype. The mounting structures for the different parts of the instrument were developed in CATIA, a professional CAD environment usually used by the department in all its primary missions. The design was tailored to the arrangement of the optical components as taken from Zemax, with minor adjustments to the mirrors. Indeed, in Zemax, it is impossible to implement a thickness for mirror elements, which are just seen as bidimensional surfaces. Therefore, the first step was to assign them their actual thickness, equal to 6 mm, to model the mounting according to the exact space occupied.

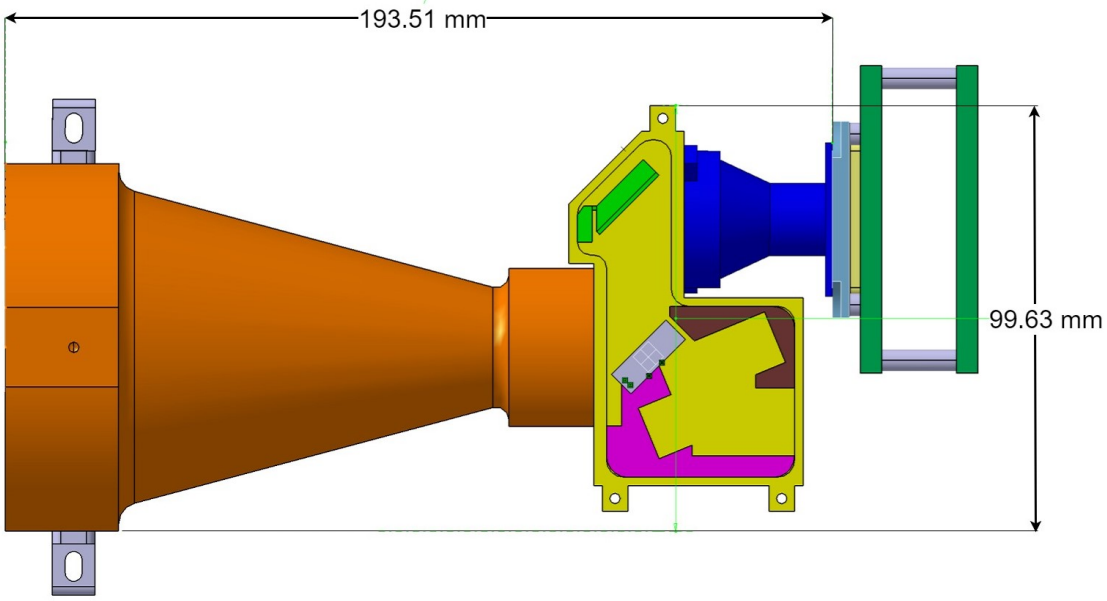

Figure 5.1: Final CAD model of the prototype with dimensions. Orange: Main Telescope Tube; Yellow: Transceiver Box; Blue: Receiver Tube; Green, circuit board for the SPAD array.

The final setup is presented in Figure 5.1. It's composed of three main sections:

- In orange, the Main Telescope Tube (MTT). It holds the two primary lenses of the instrument,

AL75150-A and LD2297-A, shared between the transmitter and the receiver paths. This part works, therefore, as a laser beam expander and as the first leg of the focusing optics.

- In yellow, the Transceiver Box (TB). It contains all the mirrors of the instrument, in particular, two PF07-03-P01 (the shared borehole mirror and the second receiver mirror) and two NB05-K12, the special mirrors optimised for the reflection of Nd:YAG lasers at 532 nm. In this capture, however, only the shared mirror is depicted.
- In blue, the final Receiver Tube (RT). It holds the last two lenses of the instrument, namely AL2550G-A and LB1014-A, before interfacing with the detector headboard.
- In green, the Printed Circuit Board (PCB) mounting the SPAD detector array. It is a COTS component procured from Fraunhofer IMS; therefore, its dimension is not optimised for the current setup.

Overall, the prototype, excluding the laser source and the detector board, succeeds in fitting within the desired 2 U, even though this is not crucial at this development stage.

Some important features of each part will now be presented.

5.2. Main Telescope Tube

The MTT is mounted on the breadboard through three supports, two in the front and one in the rear. These three will hold the entire weight of the prototype, considering that the rest of the instrument has no other support points. Consequently, the interface between the MTT and the TB is extremely delicate: it must guarantee enough stiffness to hold the rest of the instrument and ensure a precise alignment of the optical paths throughout the passage between one section and the other.

The identified solution is represented by the double-purpose interface on the MTT shown in Figure 5.2. It has a thin bump to allow for clearance centration of the MTT with the TB and a flange with six threaded holes to fix the two components together. Theoretically, only three of them are required for an isostatic positioning. Still, the redundancy may help in the case of unexpected effects or difficulties with the mounting procedures due to the limited size of the instrument.

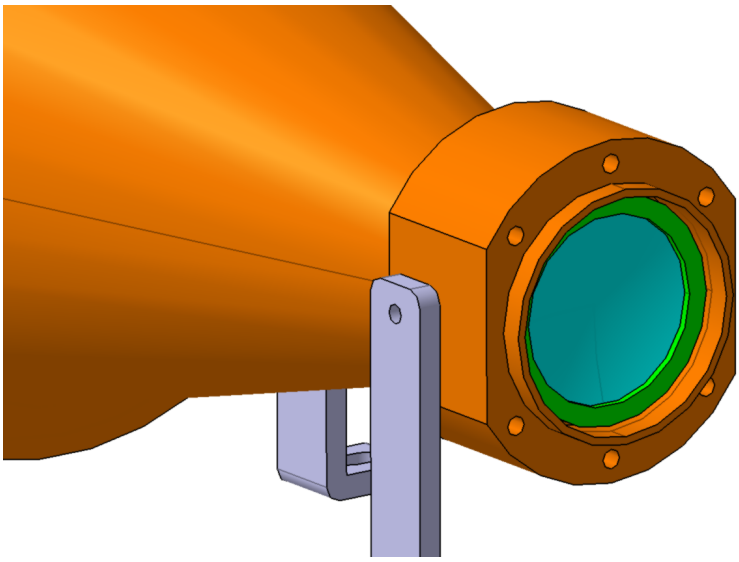

Figure 5.2: Rear end of the Main Telescope Tube, or MTT. The centration bump and the flange with threaded holes represent a double-purpose interface to align and fix the component to the rest of the instrument.

Another peculiarity of this component that must be cited is the mounting of the lenses. The chosen approach involves flat bumps on the inner walls of the MTT, clearly visible in Figure 5.3, to support the rear surface of the lenses and place them at the correct distance. Successively, retaining rings are screwed on the front surface of the lenses to fix their position. This is a common and simple practice for mounting lenses in optical systems and does not reduce the available FoV of the instrument below the level investigated with the numerical simulations.

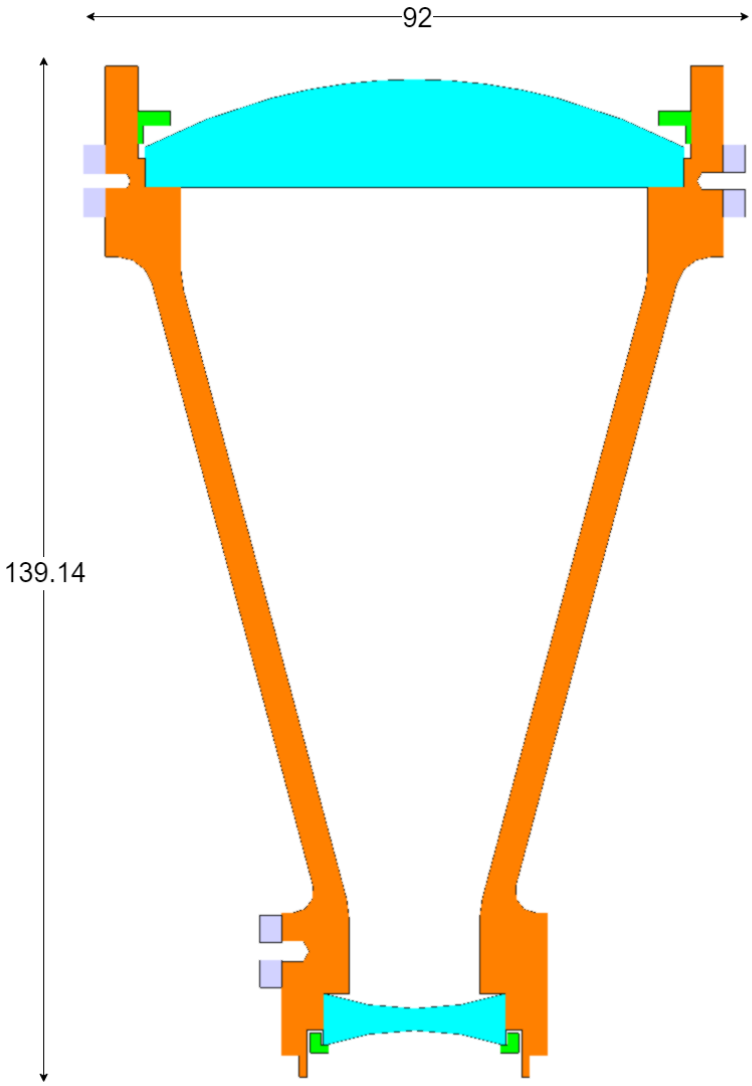

Figure 5.3: Longitudinal section of the Main Telescope Tube and respective size (in mm). Each part is highlighted in different colours: in orange, the main case; in light blue, the two lenses; in grey, the mounting legs; in green, the retaining rings.

Lastly, on the top of the front surface, it is possible to see a planar cut with a screw. This space can be used to implement an alignment cube and indicate the pointing direction of the instrument for future tests, e.g. for mounting procedures during the expected flight campaigns.

5.3. Transceiver Box

Moving forward, the TB is the core of the prototype, acting as a combiner between the main transmitter part, the MTT, and the main receiver part, the RT. It contains the supports for positioning the instrument's four mirrors, as visible in Figure 5.4.
These parts are tailored to the geometry of the system and the size of the mirrors and are screwed inside the box separately. In particular, the two supports on the left are entirely fixed, and the mirrors are glued in the dedicated spots without the capability to tune their orientation for alignment purposes. Although this choice may seem contradictory to the explanations provided in Chapter 4, the motivation comes from reducing the number of variables in the system. Indeed, since the manufacturing tolerances for the alignment angles match those used as input for the Monte-Carlo simulations, an alignment by manufacturing tolerances is enough to ensure the wanted error compensation for the transmission. The possibility of adjusting the orientation of the laser source, inserted by the hole on the bottom left, also

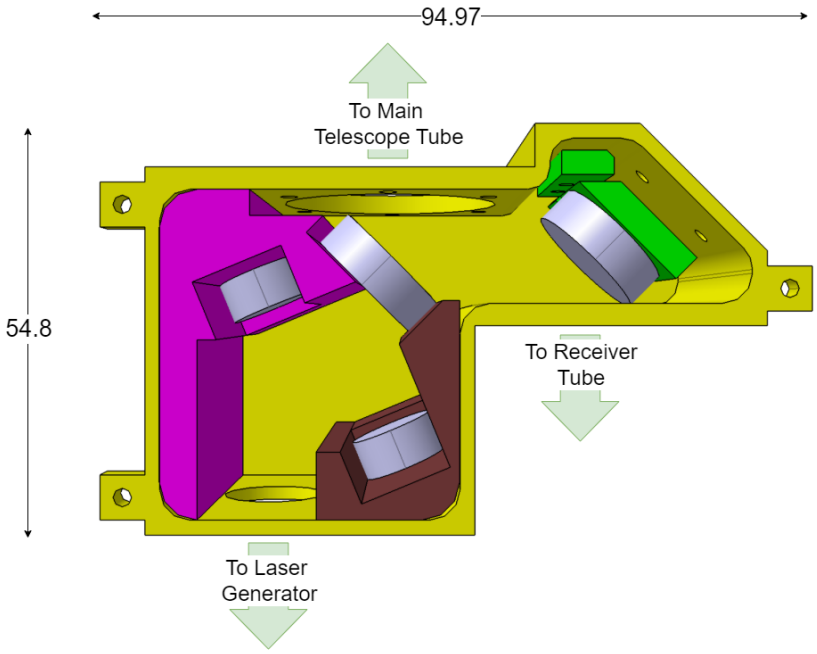

Figure 5.4: Details on the interior of the Transceiver Box and overall size of the component (in mm). The pink and brown supports are fixed to the walls, while the green one is flexible and can be adjusted by pushing some screws from the back holes (three in total, with the third in the lower right not visible from this perspective). Please note that the pink support was shaped to guarantee enough space in the upper part to handle and place the screws needed to fix the TB with the MTT.

allows for further flexibility to correct unforeseen problems.

Instead, this may not be enough for the receiver path, especially considering the limited size of the detector's pixel array. Therefore, the mirror mounting on the right is an adjustable solution. It has a thinning, visible in the details in Figure 5.5, that makes it flexible enough to change inclination into two different orientations. By inserting some screws from the back, it is possible to push them against the support, apply force on this thin arm and exploit the mirror to direct the signal toward the wanted pixel.

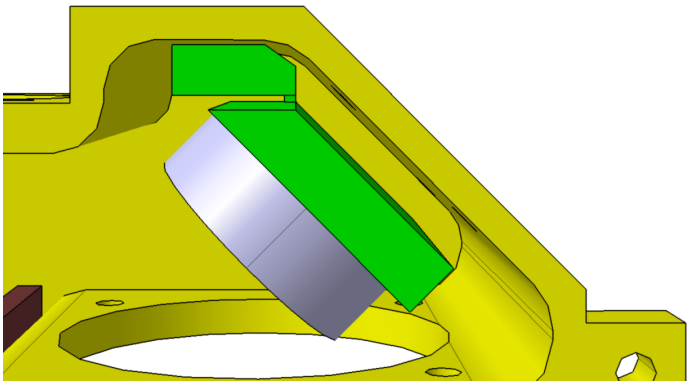

Figure 5.5: Details on the structure of the adjustable support. The thinning extends only for a few millimetres from the base of the box, giving enough flexibility to push the support with screws (one in the upper left, one in the lower right) and apply controlled momentum in two different directions. By doing so, the pointing of the mirror can be adjusted accordingly to the coalignment needs. Please note that the thread on the upper right was included only to increase the system's stability but will not be used as an active control mechanism since it would act in two different planes.

5.4. Receiver Tube

The last component is the RT, highlighted in Figure 5.6. In a few words, it is a smaller version of the MTT: it also presents a centration bump and some flanges to connect with the TB, and the same mounting scheme for the lenses, combining flat bumps and retaining rings.

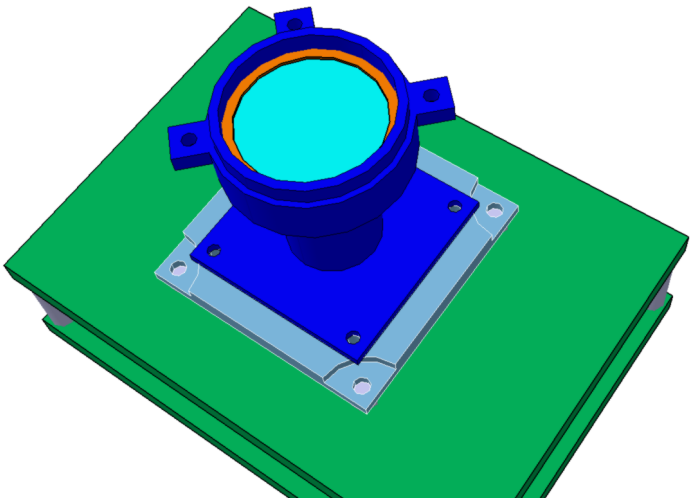

Figure 5.6: Details on the Receiver Tube and the detector headboard.

However, as visible in Figure 5.7, it required some variations, not only linked to the aspect ratio. Indeed, during the mechanical design process, it was decided to allocate the band-pass filter in the same accommodation as the first lens of the receiver path. This is where the rays are collimated, and the narrow band-pass filter performs best according to its specifications. Additionally, considering that the 25.4 mm diameter of the filter is almost the same as the lens AL2550G-A, this strategy provides the most compact arrangement possible without additional major mounting components.

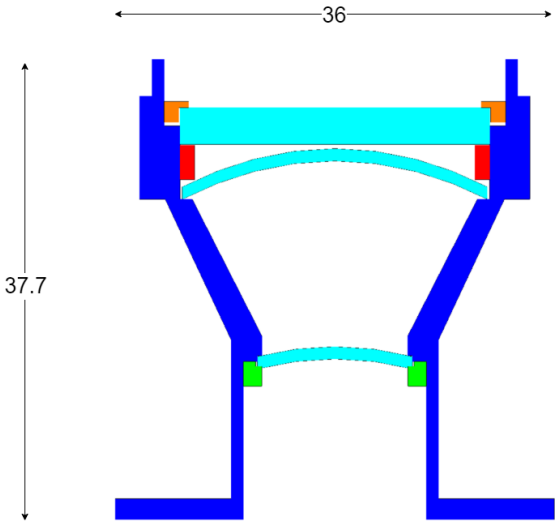

Figure 5.7: Longitudinal section of the Receiver Tube and respective size (in mm). In blue, the main case with the centration bump on the top and the plate interfacing with the detector plane on the bottom; in light blue, the two lenses and the band-pass filter; in orange and green, the retaining rings; in red, the spacer.

The only variation regards the type of rings implemented: in this case, the combination of a spacer (red element) to separate the two optical components and a proper retaining ring (orange element) to constrain their position. This solution also allows quick and simple filter tilting to maximise the transmission at the system reference wavelength, as explained later.

Concerning the interface with the detector, this project's experimental plan involves using the SPADeye2 single-photon counting CMOS detector with a double linear pixel array provided by Fraunhofer IMS [66]. As visible in Figure 5.8, the detector (pixel size: 40.56 x 52.4 μ m^2, fill factor: 5.32%) is mounted on a dedicated PCB and is accessible through a protective mask. This mask provides the mechanical connection with the RT: the Receiver Tube is centred on the mask, focusing the incoming signal in the middle of the detector, specifically on the first of the two lines. In the prototype configuration, however, the lines are placed vertically, and the signal will be focused on the left line.

This arrangement differs from the 3x3 pixel array required for the mission, for which squared pixels of 50 x 50 μm^2 and a higher fill factor are assumed. However, it is still sufficient to verify the functioning principle behind the detection of lateral variations on the target. The size of the spot diagram shown in Chapter 4, indeed, is sufficient to spread the photons on two adjacent pixels and test their response.

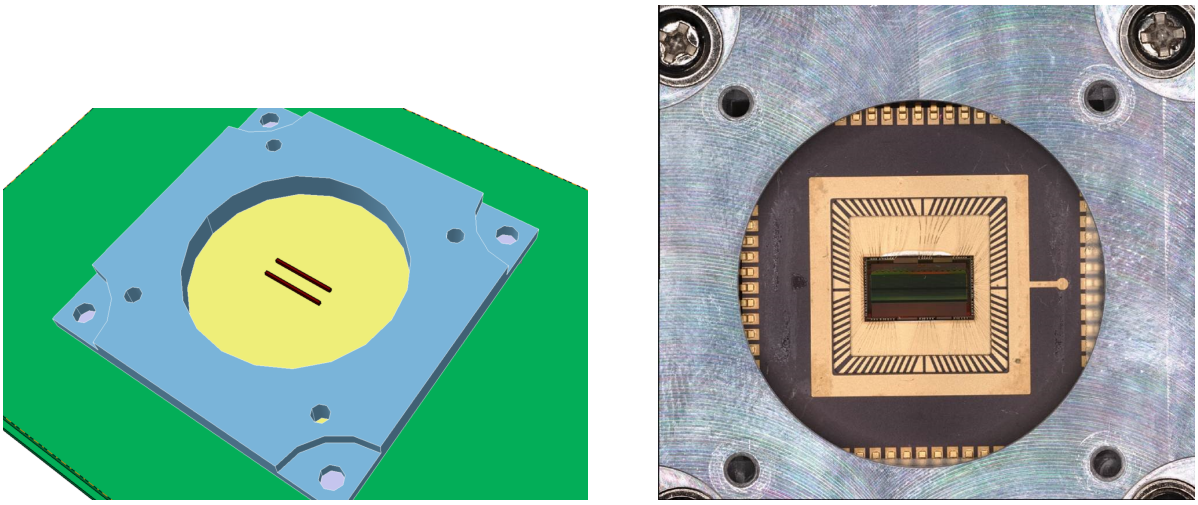

(a) SPADeye2 CAD design.

(b) SPADeye2 mounted in the mechanical interface.

Figure 5.8: On the left: Simplified CAD of the detector headboard implemented in the experiments of this project. The red lines and the yellow area represent the double linear pixel array and the corresponding substrate; the green area is the dedicated PCB connecting the detector to the input power and the PC; the light blue component is a mechanical mask used to protect the detector and interface with other equipment. On the right: Microscope capture of the detector array behind the mechanical mask.

5.5. Manufacturing the prototype

Each prototype section was manufactured at the in-house mechanical workshop, which exploited a Computer Numerical Control (CNC) machine to obtain the desired shapes. The process required an iterative approach to account for the manufacturability of the components. Nonetheless, the CAD renders shown in this chapter represent the final version of each prototype section.

The delivery pipeline of the final product also represented a constraint for the test campaign, which will be the main focus of the next chapter. Several configurations have been explored to permit the characterisation of the optical design's performance while waiting to receive the rest of the mounting. Some of them are reported in Figures 5.9 and 5.10.

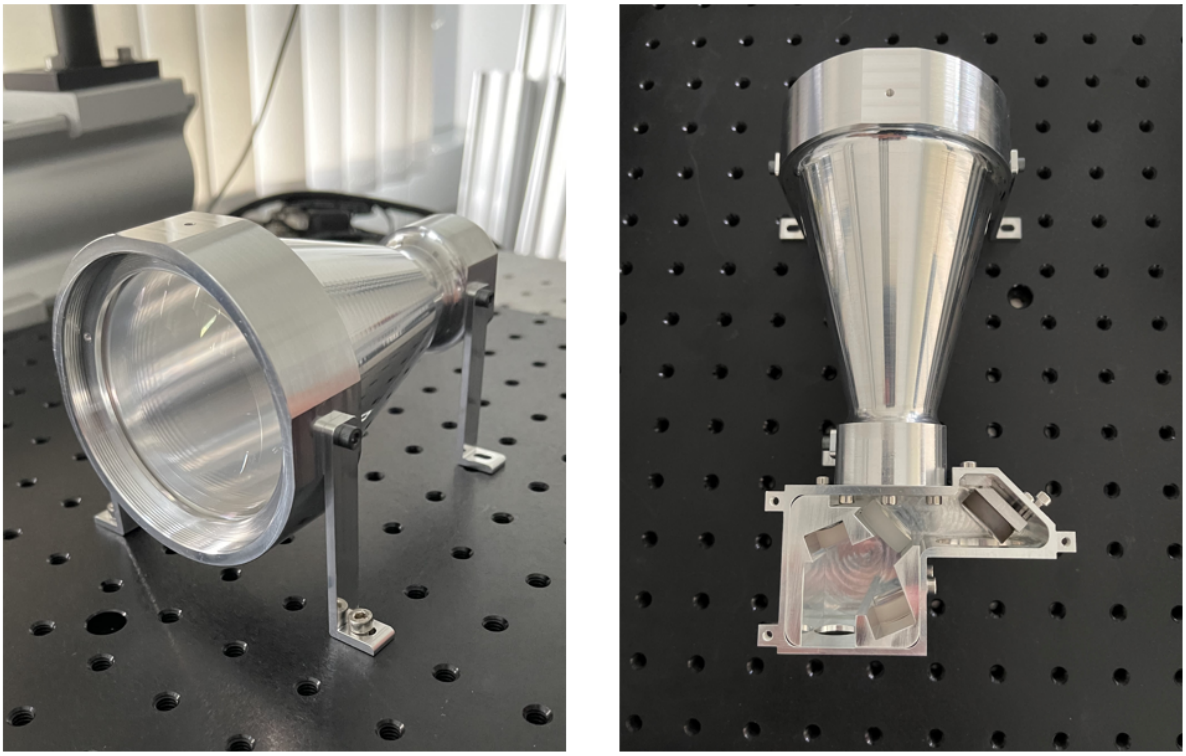

Figure 5.9: On the left, the Receiver Tube integrated with the lenses. On the right, the Main Telescope Tube and the Transceiver Box integrated with the mirrors.

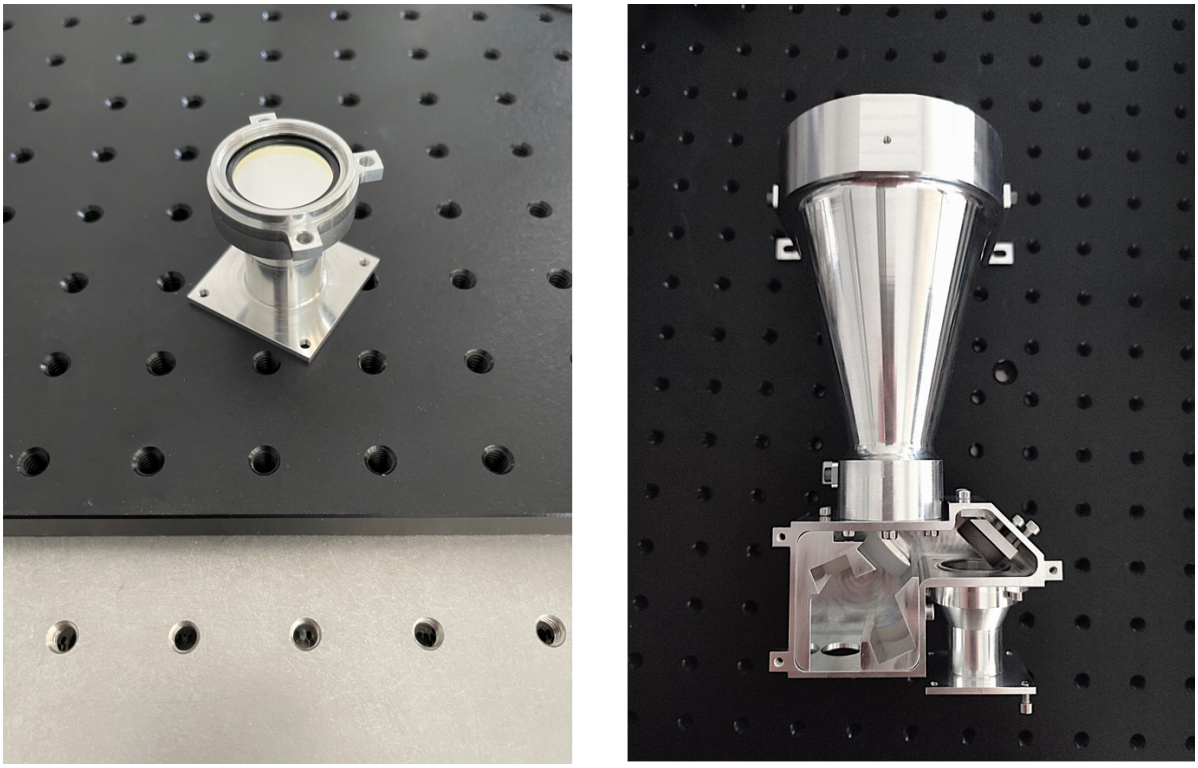

Figure 5.10: On the left, the Receiver Tube integrated with the lens and the band-pass filter. On the right, the full-mounted prototype (missing only the upper cover).

6

Performance Characterisation

This chapter reports the test campaign conducted on the prototype to assess its optical performance. It evaluates the main components of the prototype, namely the transmitter and the receiver, firstly on their own and then in synergy in the final configuration of the transceiver instrument. The aim is to assess the maximum transmission of the band-pass filter, the predictability of the expansion performance, and the feasibility of an effective ranging measurement.

6.1. Experimental Plan

The experimental plan to conduct the tests on the prototype involves a long procedure both in preparing the equipment and evaluating the performance. In particular, it is possible to identify the following steps:

1. **Procuring of the COTS optical components.** All the lenses, the mirrors, and the band-pass filter need to be purchased from the manufacturers. Due to administrative aspects and delivery times, this process usually requires a few weeks. Therefore, it was done during the CAD design manufacturing phases to optimise the precious time for the lab work.
2. **Mounting of the different sections of the prototype.** This step naturally evolves slowly because of the long time needed by the technicians to deliver the components according to the required specifics and respecting tight tolerances. The waiting time was optimised by providing a priority list for the manufacturing: the first delivered part was the MTT, followed by the TB and, lastly, the RT. By doing so, it was possible to follow the schedule illustrated below.
3. **Assessing the transmittance of the band-pass filter.** In parallel with the manufacturing of the MTT, the first lab test involves the characterisation of the transmittance of the band-pass filter when changing the angle of incidence of the light. By doing so, the aim is to maximise its transmission and reduce the losses below the level specified by the requirement.
4. **Evaluating the optical performance of the transmitter.** With the MTT ready and waiting for the manufacturing of the TB, it is possible to assess the optical performance of the expansion. The main aspects to consider are possible aberrations induced on the laser wavefront during the lens propagation and the variations in the laser beam features, namely divergence θ and M^2 factor.
5. **Evaluating the optical performance of the receiver.** When the RT is completed, the prototype can be fully assembled. Again, looking for aberrations, this time induced by the receiver optics, is possible.
6. **Aligning the receiver optical axis to the transmitter optical axis.** The last effort in integrating the prototype and making it fully operative is to adequately co-align the transmitter and the receiver optical axes. The SPAD lines array must be mounted to the RT, ensuring enough stray light suppression.
7. **Performing demonstration measurement with a target.** All this done, the final measurement proves that the prototype can discriminate between the starting pulse and the receiving pulse of the laser source unambiguously, providing a ranging measurement.

Points from 3 to 7 will be evaluated in this chapter.

6.2. Band-pass filter characterisation

As introduced in Chapter 2, a laser altimeter usually works at one predefined wavelength, depending on the choice of the laser. In the case of this project, 532 nanometers. However, the scene the receiver collects is not limited to the laser signal; it also includes the background light coming with unpredictable wavelengths. In a delicate application implementing single-photon counting detection, limiting the amount of light reaching the photodiodes is paramount because every false event is a noise source imposing a dead time, which can impede the collection of the actual signal. A band-pass filter with a narrow bandwidth must be implemented to limit this effect.

In a space mission, the design of such a filter would be tailored to the precise wavelength of the laser source. However, in prototype testing in the lab, the implementation of COTS components makes it impossible to have a perfect match in the performance of every piece of equipment. As introduced during the trade-off analysis in Chapter 4, the primary wavelength of the laser source and the Central Wavelength (CWL) of the band-pass filter are slightly off, implying a transmittance through the filter around 60%. The detailed specifics of the two are resumed in Tables 6.1 and 6.2. Going into more detail, Table 6.1 shows some measurements done in the lab to assess the wavelength variations of the laser source when varying the repetition rate. Indeed, the increase in repetition rate implies slightly higher temperatures inside the laser cavity; consequently, the particles are more excited by thermal energy and dissipate more through collisions. The macroscopic effect is a reduction of laser energy that translates into longer wavelengths. As visible, the actual fluctuation in the range of interest for the mission (135-275 Hz) is negligible and demonstrates the stability of the laser source, but the same does not apply at 1000 Hz. Table 6.2, instead, introduces some of the main properties of the band-pass filter as provided by the manufacturer, and at 0° AOI.

Table 6.1: Main wavelength of the laser source when varying the repetition rate. The uncertainty on each measurement is below 4 fm.

Repetition Rate [Hz]	Laser Generator Wavelength [nm]
135	532.0536
275	532.0534
1000	532.0742

Table 6.2: Central wavelength, bandwidth and maximum transmittance of the band-pass filter as provided by the manufacturer. The precision of the measurements is not known.

Property	Value
Central Wavelength [nm]	532.1346
Bandwidth [nm]	0.1696
Maximum Transmittance	0.8885

Nonetheless, the spectral range between the wavelength of the laser and the CWL of the filter is not so drastic, and simple strategies can be implemented to minimise the energy loss. Indeed, a band-pass filter's central wavelength depends on the AOI of the incoming light according to the following formula:

$$\lambda_c(\phi) = \lambda_{c0}\sqrt{1 - \left(\frac{\sin(\phi)}{n}\right)^2} \tag{6.1}$$

Where λ_c and λ_{c0} are the central wavelengths of the filter at the studied angle of incidence and with 0° incidence, respectively, ϕ is the angle of incidence of the light, and n the effective refractive index of the filter. This parameter depends on the design of the cavities and material used for the layers of the coating [67]. Setting the filter tilting to a specific value makes it possible to fill the gap between initial and actual CWL and maximise the transmittance. The formula is, however, valid only up to tens of degrees, after which polarisation effects appear.

Figure 6.1, retrieved from the filter manufacturer, shows the expected behaviour of a similar filter when increasing the light's incidence angle. Following the formula, the central wavelength decreases at higher AOIs, provoking an advantageous shift in this project's case.

The lab testing, therefore, aims to measure the amount of energy passing through the filter at different angles of incidence. The setup for this test, shown in Figure 6.2, involves:

1. 532 nm Nd:YAG Laser source, operated at 500 Hz;
2. Neutral density filters to attenuate the laser energy hitting the detector;

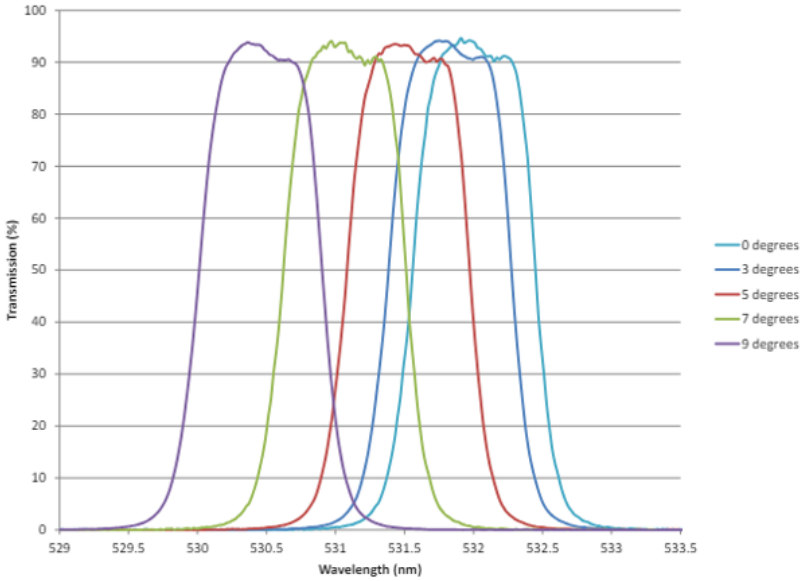

Figure 6.1: Transmittance patterns of a narrow band-pass filter for different angles of incidence. Figure from Alluxa [67].

3. First band-pass filter (bandwidth of 4 nm) to cut off the residual energy coming from higher wavelengths inside the laser source (the laser is firstly generated at 1064 nm by excitation through an 808 nm laser source and then converted to 532 nm);
4. Beam expander, required to enlarge the beam and collimate on the detector only a homogeneous part of the section;
5. band-pass filter in examination, in a kinematic mount that permits the tuning of the tilting;
6. Focusing lens, to concentrate the laser on the pixel array of the detector;
7. Energy detector (CMOS) linked to an energy meter;
8. Mechanical stage to precisely align the detector to the optical path of the laser.

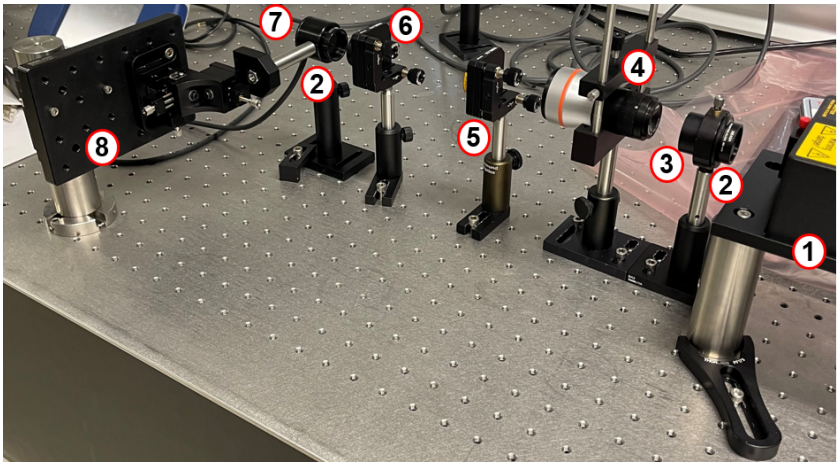

Figure 6.2: Experimental setup for the characterisation of the transmittance performance of the band-pass filter at different angles of incidence. It included: 1) Laser source; 2) Neutral density filters; 3) First band-pass filter; 4) Beam expander; 5) band-pass filter in examination; 6) Focusing lens; 7) Energy detector; 8) Mechanical stage.

An autocollimator assisted in aligning the band-pass filter with the laser source (Figure 6.3).

Considering the narrow bandwidth of the filter and the closeness of the two reference wavelengths, the evaluated range is limited to $\pm$ 3° with steps of $0.25°$. The results are given in Figure 6.4 and resumed in Table 6.3. As expected, the transmittance is maximised at angles of incidence different

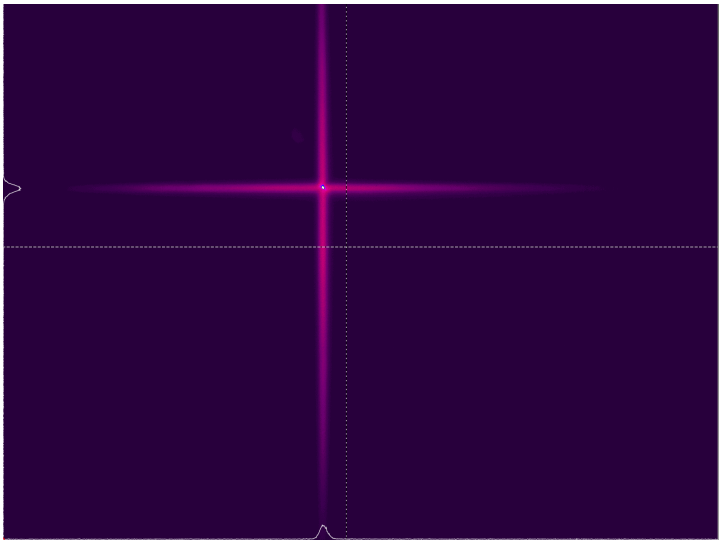

Figure 6.3: Image captured from the autocollimator. The cross-shaped signal and the very bright dot of the laser beam are centred. This means that the transmitted signal and the reflected signal of the band-pass filter are aligned on the same optical axis.

from zero, in this case $\pm$ 1.5°. The effect is almost symmetrical, with peak-to-peak variation limited to 2% of total transmittance, meaning that the filter's orientation is not critical for the blocking performance.

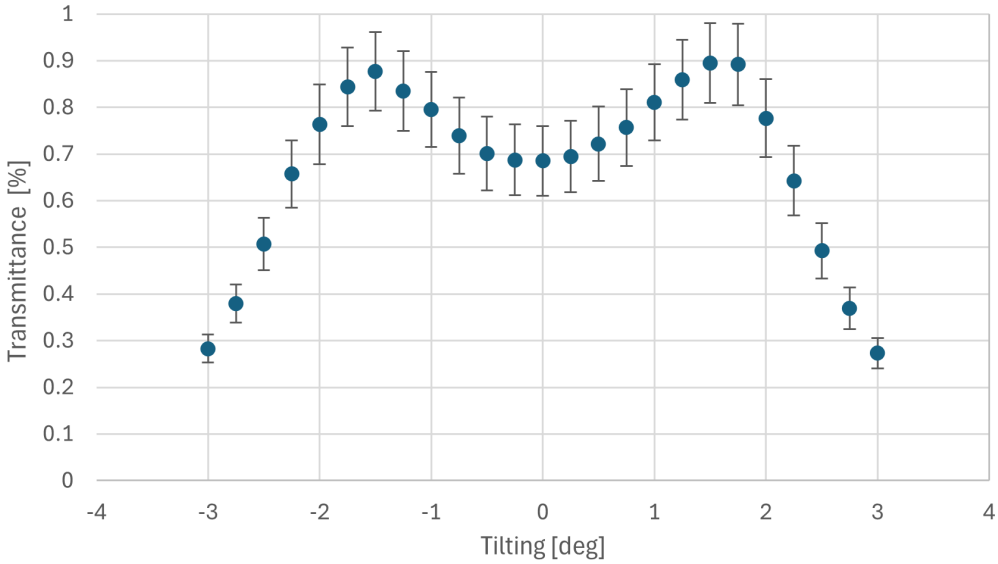

Figure 6.4: Transmittance of the band-pass filter at different tilting angles. The behaviour is almost symmetrical in both directions. The error bars indicate the RMS stability of the measurements over the total number of samples (10000 for all the data points) collected by the energy meter.

Table 6.3: Measured transmittance of the band-pass filter at the maximising tilting angles and for different repetition rates.

Angle of Incidence [°]	+1.5	-1.5	+1.5	-1.5	+1.5	0	-1.5
Repetition Rate [Hz]	135		275		500		
Transmittance [%]	85.13 $\pm$ 4.9	87.36 $\pm$ 4.6	91.8 $\pm$ 5.7	88.66 $\pm$ 5.7	89.5 $\pm$ 8.6	68.52 $\pm$ 7.4	87.7 $\pm$ 8.4

The complete curve is derived for the laser operating at a repetition rate of 500 Hz. Still, other measurements were conducted at the mission's reference repetition rates (135 and 275 Hz) to validate the results. Apart from slight variations in the absolute values linked to the laser's wavelength variations, the pattern is maintained and permits to get, once inserted as input in Table 4.10, a total transmittance above the required 80%.

As a last remark, the effective refractive index of the band-pass filter was retrieved from the experiments to provide a general characterisation in case of future changes in the laser source for the actual mission. Indeed, by inserting the measured wavelength of the laser at 275 Hz and the maximising AOI in Equation 6.1, it is possible to obtain an effective index of 1.4985. By plotting the pattern of the formula as in Figure 6.5, one can directly estimate the best tilting of the filter, knowing the wavelength of the laser. This strategy could avoid the need to procure a tailored filter, reducing costs and time for the preparation of the mission. Still, it must be compromised with the deflection effects generated by this kind of filter.

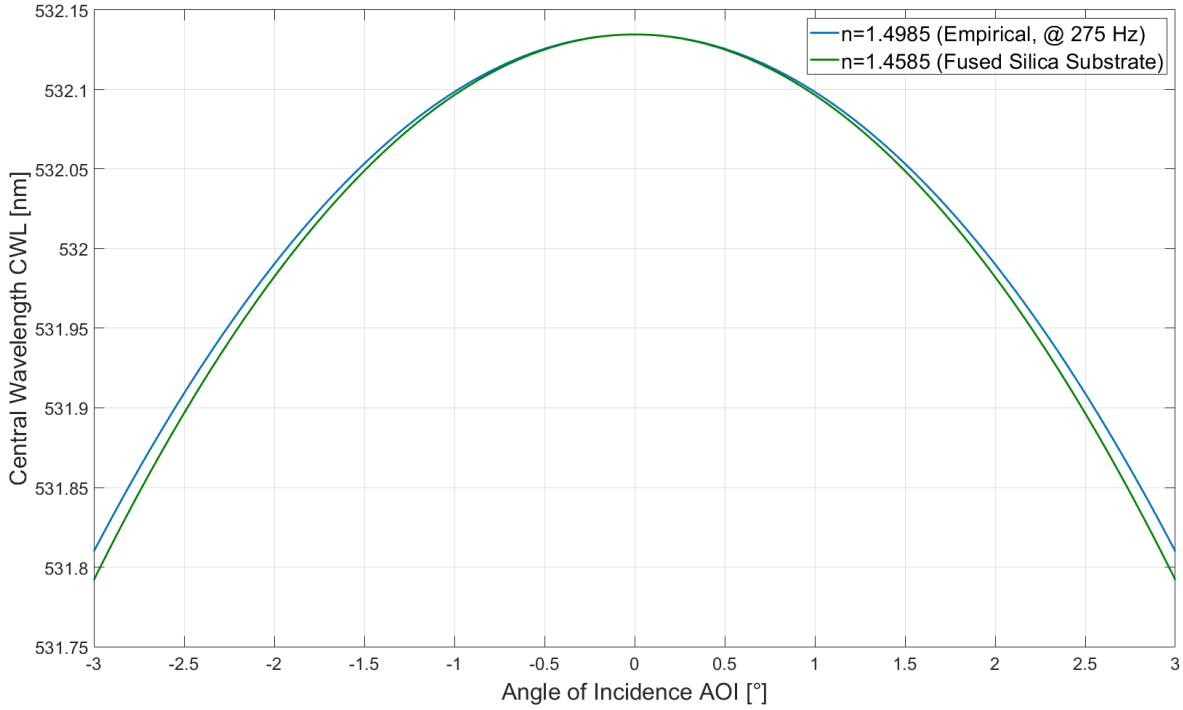

Figure 6.5: Central wavelength shift of the band-pass filter at different angles of incidence of the light, using the measured effective refractive index and the fused silica substrate refractive index.

6.3. Expansion performance

The verification process to demonstrate the prototype's compliance with the performance simulated for the trade-off analysis requires considerable effort in preparing scores of lab setups. However, not all of them can fit within the limited time frame of this thesis.

Considering this, as well as the delivery timeline of the components (in order: MTT, TB, and RT), the most compelling and straightforward parameter to assess is the transmitter's expansion performance.

This is compelling because demonstrating that the expansion ratio provided by the instrument is predictable through relevant simulations permits to confirm that the footprint size at the target will satisfy the requirements, enabling the mission's relevant scientific measurements.

On the other hand, the assessment of this parameter is direct because it requires only the Main Telescope Tube, which holds the optical elements that contribute to expanding the laser beam. Therefore, the test setup implements a simplified system directly coupling a 532 nm microchip laser at the input of the MTT. Even if the beam's position, configuration, or initial properties are not the same as in the nominal design, it is still possible to measure the variations induced by the MTT and compare it with the expected theoretical behaviour of an analogous simulation.

Figure 6.6 depicts the mentioned setup, which involves:

1. The 532 nm microchip laser source, mounted on a vertical plate;
2. The MTT under examination;
3. A lens with a focal length of 150 mm;
4. A specialised camera to capture laser beams, connected to the lab computer and protected by neutral density filters.

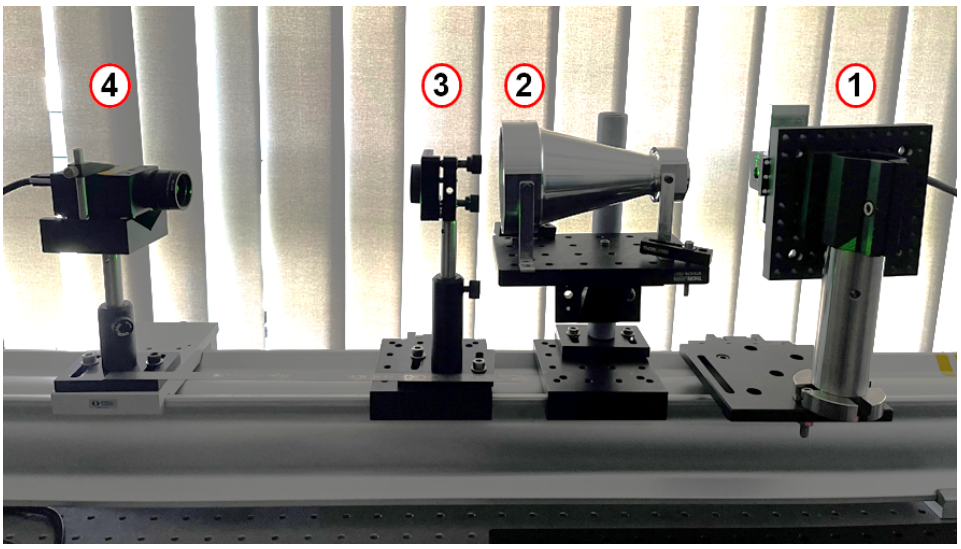

Figure 6.6: Experimental setup to test the expansion quality of the MTT. 1) 532-nm microchip laser; 2) Main Telescope Tube; 3) Focusing lens; 4) Laser-beam detector with neutral density filters.

The applied procedure is the same as in Chapter 2, and Table 6.4 reports the measurements of the beam sections after the control lens in both the x and y directions.

Table 6.4: Beam section diameters at different distances from the focusing lens. According to the manufacturer, beam size measurements with and without calibration have an accuracy threshold of 3 and 1% of the measured value, respectively. Since the exact uncertainties are not available for this experiment, a conservative 3% will be accounted for in the next steps.

Distance [mm]	Diameter$_x$ [mm]	Diameter$_y$ [mm]	Distance [mm]	Diameter$_x$ [mm]	Diameter$_y$ [mm]
65.0 $\pm$ 0.5	3.245	3.443	145.0 $\pm$ 0.5	0.495	0.536
75.0 $\pm$ 0.5	2.900	3.062	155.0 $\pm$ 0.5	0.107	0.145
85.0 $\pm$ 0.5	2.539	2.671	165.0 $\pm$ 0.5	0.247	0.235
95.0 $\pm$ 0.5	2.200	2.369	175.0 $\pm$ 0.5	0.611	0.626
105.0 $\pm$ 0.5	1.874	2.019	185.0 $\pm$ 0.5	0.964	1.007
115.0 $\pm$ 0.5	1.518	1.632	195.0 $\pm$ 0.5	1.328	1.401
125.0 $\pm$ 0.5	1.181	1.270	205.0 $\pm$ 0.5	1.649	1.756
135.0 $\pm$ 0.5	0.839	0.906	220.0 $\pm$ 0.5	2.235	2.375

The captures are provided in Appendix A. Each image was tuned to avoid camera saturation by implementing neutral density filters, used to scale the intensity of the laser, or by varying the exposure time of the detector. Additionally, each image was corrected for a reference flat field captured without laser illumination. The software BeamGage helped visualise the images on the PC and compute the size of each beam section following the ISO standard procedure.

The final interpolations are shown in Figure 6.7. They were derived by minimising the sum of the squared relative deviations of the diameters at each reference distance. The calculated coefficient makes it possible to compute all the geometrical features for the beam after and before the control lens, obtaining more insight into the expansion induced by the MTT.

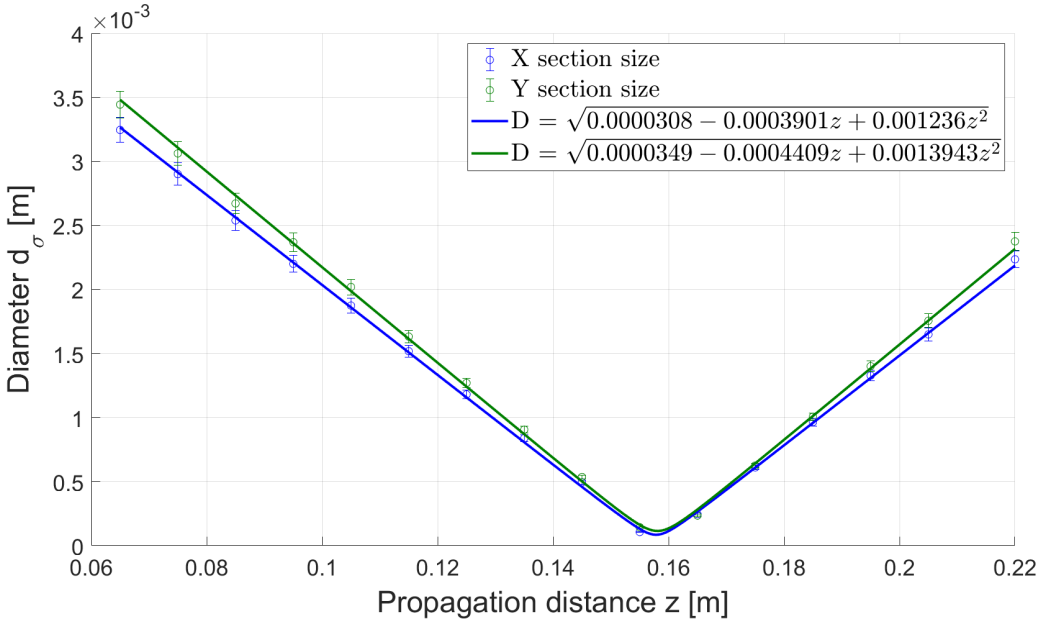

Figure 6.7: Hyperbolic interpolations of the longitudinal section of the laser beam after the focusing lens. The x and y sections are slightly asymmetric as a propagation of the features of the original laser beam.

Table 6.5 reports the coefficient values and respective standard deviations in more detail, while Table 6.6 lists the mentioned results. Unfortunately, due to a lack of data points in the Rayleigh range of the beam, it was not possible to compute reasonable uncertainties using Gaussian error propagation. Nevertheless, a minimum and maximum worst-case approach still permitted the identification of some boundaries for the measured values.

Table 6.5: Hyperbolic coefficients for the laser beam fit and respective uncertainties.

Coefficient	Value	Std. Deviation	Coefficient	Value	Std. Deviation
a_x [m^2]	$3.079 \cdot 10^{-5}$	$6 \cdot 10^{-8}$	a_y [m^2]	$3.491 \cdot 10^{-5}$	$1 \cdot 10^{-7}$
b_x [m]	$-3.901 \cdot 10^{-4}$	$6 \cdot 10^{-7}$	b_y [m]	$-4.41 \cdot 10^{-4}$	$1 \cdot 10^{-6}$
c_x [-]	$1.236 \cdot 10^{-3}$	$3 \cdot 10^{-6}$	c_y [-]	$1.396 \cdot 10^{-3}$	$6 \cdot 10^{-6}$

Table 6.6: Geometrical parameters for the laser beam, derived from the hyperbolic coefficients, after and before the lens and in the two radial coordinates x and y. In the proposed order, each trio of values corresponds to the fitting's minimum, mean, and maximum results. Due to the lack of data points, the minimum values often get to zero. In those cases, the lower boundary is not reliable.

Feature	Value after the lens	Value before the lens	Feature	Value after the lens	Value before the lens
$z_{0,x}$ [mm]	1572 1578 1584	-1702 -2770 -6240	$z_{0,y}$ [mm]	1569 1581 1593	-1370 -2580 -7968
$d_{\sigma 0,x}$ [μm]	0 85 312	0 1555 6493	$d_{\sigma 0,y}$ [μm]	0 115 496	0 1993 10815
θ_x [mrad]	35.11 35.15 35.20	1.31 1.92 2.40	θ_y [mrad]	37.29 37.37 37.45	1.29 2.15 2.81
M_x^2	0 4.42 10.42		M_y^2	0 6.34 13.00	

Despite the high uncertainties, it is still possible to check whether confirming the results with the simulations is possible. Since the laser source differs from the one used in the trade-off simulations, as first step, it is necessary to know the characteristics of the plain laser without passing through any optical element. For this reason, a simple capture of the 532 nm microchip laser is taken with the wavefront sensor, providing the main features of the beam resumed in Table 6.7.

The measured parameters are then input for a simple Zemax simulation reproducing the experiment setup. This allows one to compare the software's theoretical results with the empirical data and refine the confidence interval.

Table 6.7: Measured parameters for the plain 532 nm microchip laser. The waist position is negative because it's opposite to the direction of light propagation. According to similar tests from the manufacturer [68], the accuracy on $d_{\sigma 0}$ is close to 0.03%, on z_0 to 0.04%, and on M^2 to 1%. Since the software calculates z_R similarly, the same accuracy of z_0 is assumed.

Feature	$d_{\sigma 0}$ [μm]	z_0 [m]	M^2
x-value	491	- 0.671	3.858
y-value	508	- 0.669	4.442

Figure 6.8 shows the simulation setup. It involves a laser source placed at a distance and with characteristics similar to the one used in reality and the two lenses of the MTT. In particular, the beam waist is placed around 0.44 m back from the laser source, subtracting from the measured z_0 the gap between the laser source and the wavefront sensor at the moment of the measurement. Additionally, the laser is assumed to be symmetrical.

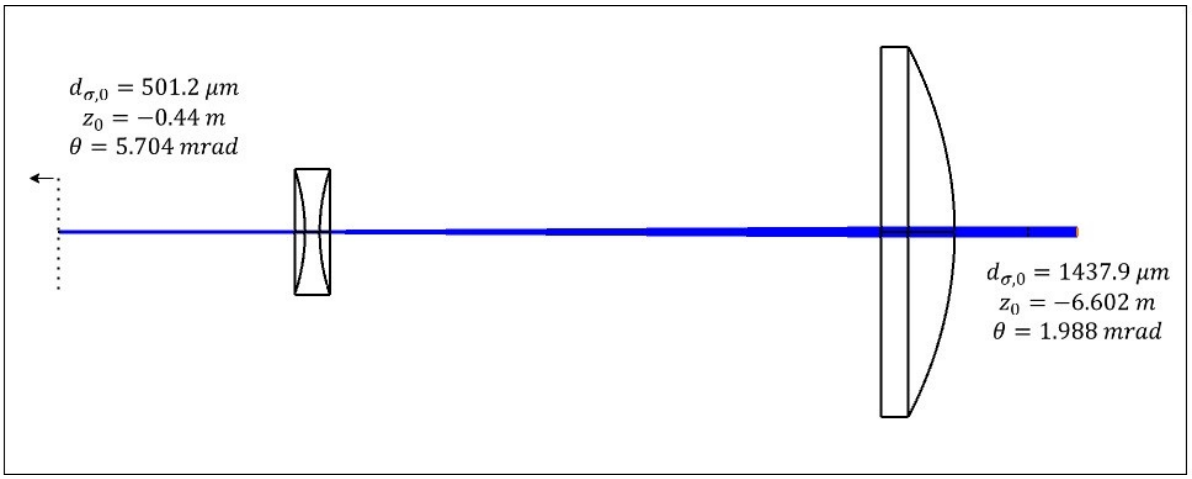

Figure 6.8: Sketch from the Zemax simulations used to validate the hyperbolic fit results. The annotations provide the results from the simulation before the first lens and after the last lens of the MTT.

Given only the waist size, its position, and the M^2 as input, the simulation returns the initially expected divergence and geometrical parameters after the last lens of the MTT.

Compared with the calculations from the hyperbolic fitting, the latter's results are more reliable than the width of the confidential intervals suggests. The divergence and beam size simulated values are close to the measured mean values, while the beam position is slightly off the interval.

The comparison indicates that the hyperbolic fitting reliably represents the laser beam exiting the MTT and demonstrates the telescope's predictable expansion behaviour. However, one parameter requiring further testing is the M^2 quality factor, which the Zemax simulation cannot constrain. The fit suggests a slight degradation in laser quality after passing through the optics, which could impact the quality of the returning signal and must, therefore, be assessed in future experiments.

6.4. Wavefront distortion

As introduced in Chapter 2, verifying that the optical system can handle the starting and returning signal, producing as few artefacts as possible in the wavefront, is paramount. This verification demonstrates the design's capability to perform a timing measurement with appreciable lateral variations, which can then be linked to topographic features on the target.

The implemented test procedure for the transmitter uses the setup in Figure 6.9. It consists of:

1. A laser source, operating at 520 nm, collimated by a commercial expander. This component is necessary to guarantee that the wavefront is planar when approaching the MTT.
2. The MTT under examination.
3. A Shack-Hartmann wavefront sensor, equipped with a microlens array to discretise the different sections of the wavefront and focus them on a CMOS detector. By doing so, it computes the wavefront's shape by determining the local shifts of the centroids formed by the microlenses.

It is essential to specify the ideal wavelength of the laser source implemented for such tests would be 532 nm, but 520 nm is close enough to provide relevant results for the prototype's performance.

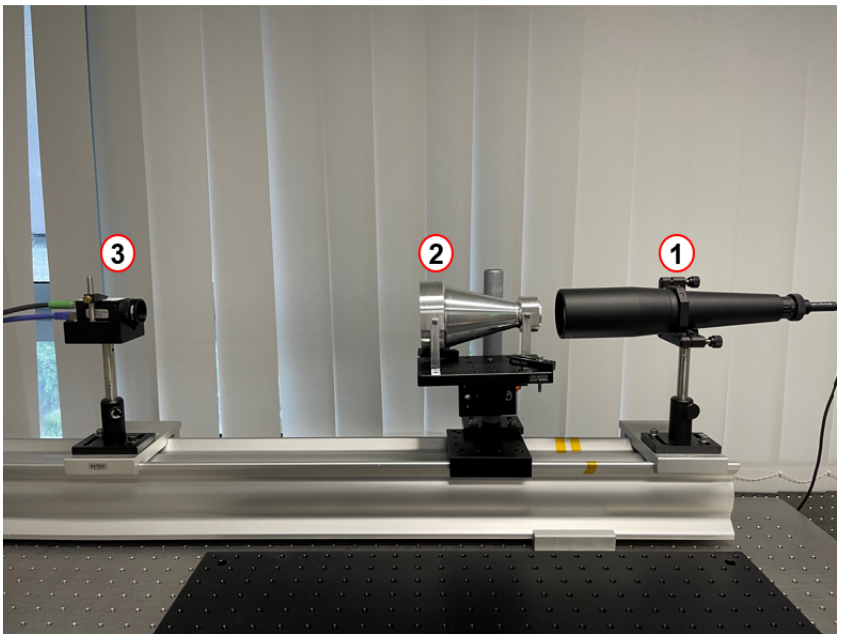

Figure 6.9: Experimental setup to test the wavefront distortion induced by the MTT. 1) 520-nm collimated laser source; 2) Main Telescope Tube; 3) Shack-Hartmann wavefront sensor with neutral density filters.

The capture with the sensor was performed first without the MTT to collect a reference, then integrating the tube to assess the induced variation. The result, already corrected by subtracting the reference, is resumed in Table 6.8 and shown in 2D and 3D in Figure 6.10.

Table 6.8: Results from the wavefront characterisation of the signal passing through the MTT. The P-V (Peak-to-Valley) variation is the range between the maximum and minimum distortion of the wavefront, while the RMS error represents the deviation averaged over the entire wavefront. The values are expressed in a fraction of the wavelength (520 nm). According to the manufacturer, the expected error on the measurements varies between $\lambda/15$ and $\lambda/20$ [69].

Property	P-V	RMS Error	Max Value	Min Value
Value	0.484	0.0746	0.228	-0.255

As visible in Figure 6.11, when evaluating these results with the Mahajan expression, the corresponding value of the Strehl Ratio for the RMS error resulting from the MTT test is precisely above the aberration-free threshold ($S = 0.8$ or RMS error < 0.075).

This result was not required by the optical design specifications, but it is still beneficial. Indeed, it indicates that the starting signal will reach the target with a high-quality wavefront, enhancing the capability to capture the relevant topographic features on the returning signal.

The same procedure can now be applied to the receiver with an identical setup, except, as visible in Figure 6.12, for the orientation of the prototype. In this case, indeed, it is the main, aspheric lens of the telescope tube that faces the laser beam first. The passage through the other lenses, channelled by the mirrors, completes the focusing of the signal beyond the Receiver Tube, in the gap with the Shack-Hartmann sensor, positioned with a slight offset from the focus to appreciate the actual deformation of the wavefront, which would otherwise be planar.

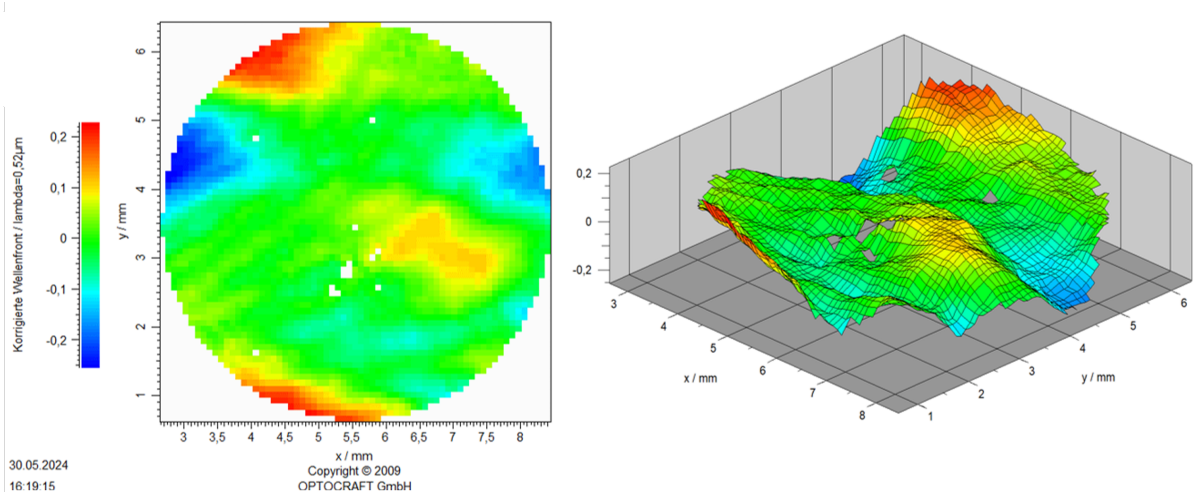

Figure 6.10: Wavefront of the transmitter beam path. On the left, the 2D representation, on the right, the 3D map. The colour map is expressed in a fraction of the wavelength (520 nm).

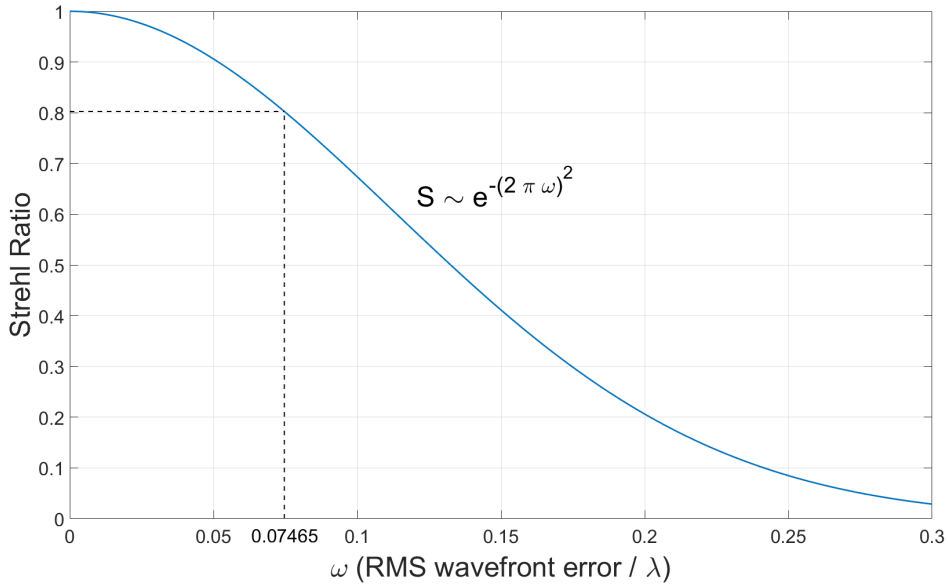

Figure 6.11: Result for the MTT Strehl ratio computed with the Mahajan approximation.

Two elements in the prototype differ from the prototype's nominal configuration. In particular:

- The borehole mirror inside the TB, which is replaced by a full mirror because it was not possible to drill the silica substrate in time for the experiment;
- The band-pass filter, which is missing because of its incompatibility with the wavelength of the collimated laser generator.

Surely, these limitations preclude the assessment of the diffraction generated by the hole and the distortion caused by the passage through the filter, which remains paramount for future studies.

Considering that the receiver path presents far more optical elements than the telescope tube, including the telescope tube itself, the overall performance is not expected to match the transmitter's diffraction-limited result. Indeed, from the results in Table 6.9 and the same Mahajan's approximation approach shown in Figure 6.15, the overall Strehl ratio computed for the receiver is limited to 0.4753, almost half of the solid 0.8 achieved by the transmitter (without mirrors).

This worsening is not a showstopper for the prototype's performance, but still, it indicates a possible degradation in the data quality. During the experiment, the subtraction of the reference from the measurements showed little to no variations in the result, meaning that the effect is generated inside the

prototype and can be mitigated by: 1) refining the tilting of the lenses in their accommodation, especially concerning the aspheric lens in the Receiver Tube that was not strictly blocked due to the absence of the band-pass filter; 2) implementing the customised lenses in the Receiver Tube.

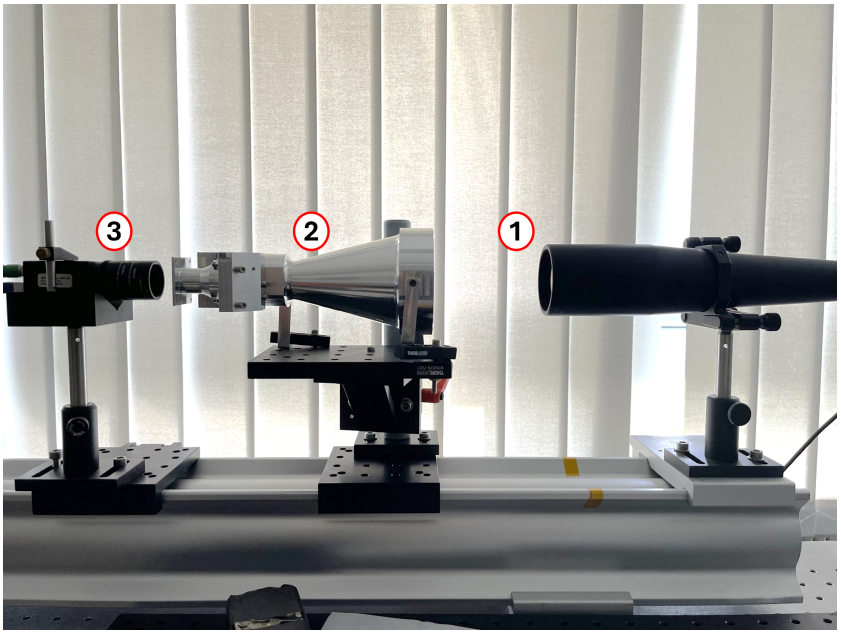

Figure 6.12: Setup for wavefront testing of the receiver optics. 1) 520-nm collimated laser source; 2) Tested prototype, with the telescope directed toward the laser source; 3) Shack-Hartmann wavefront sensor with neutral density filters.

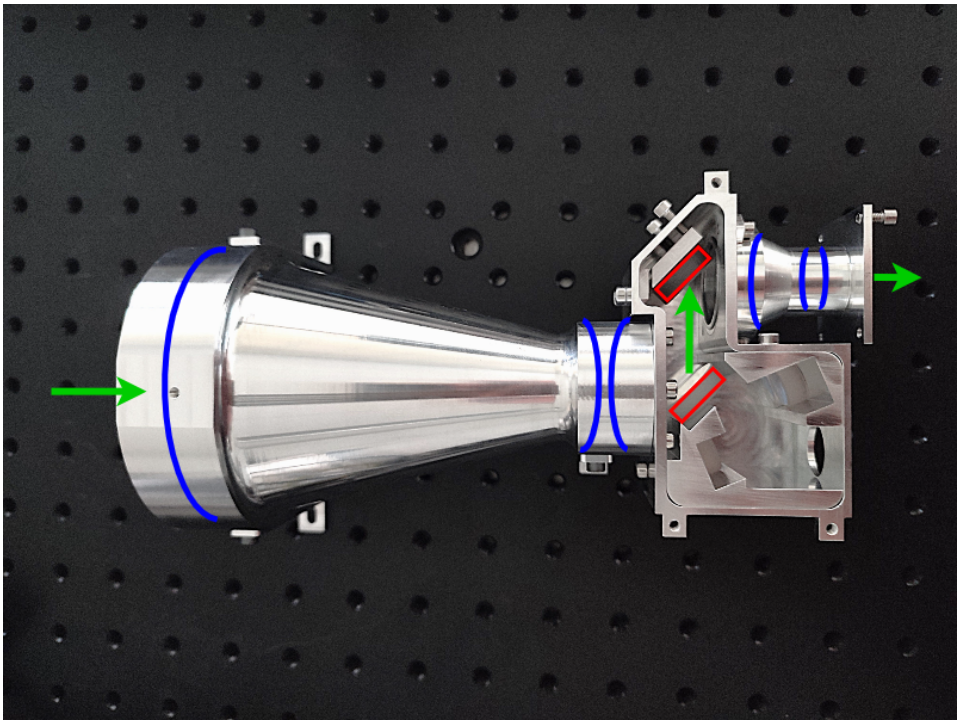

Figure 6.13: Internal arrangement of the prototype for the wavefront test of the receiver. In blue, the main optical surfaces of the lenses; in red, the outline of the two folding mirrors. The green arrow indicates the direction of the incoming laser beam.

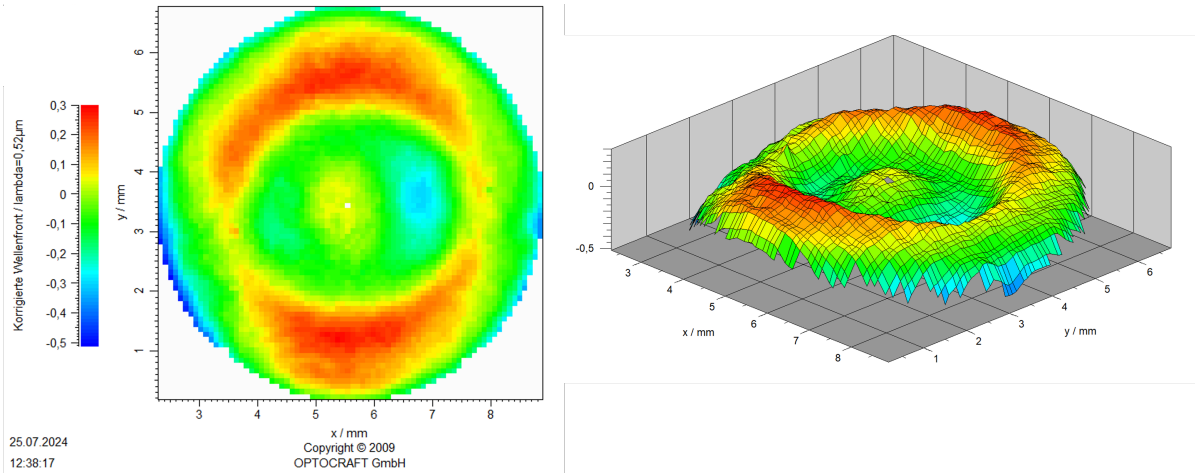

Figure 6.14: Wavefront of the receiver beam path, corrected for the reference without optical elements between the laser source and the detector. On the left, the 2D section, on the right, the 3D map. The colour map is expressed in a fraction of the wavelength (520 nm).

Table 6.9: Results from the wavefront characterisation of the signal passing through the receiver. The values are expressed in a fraction of the wavelength (520 nm). According to the manufacturer, the expected error on the measurements varies between $\lambda/15$ and $\lambda/20$ [69].

Property	P-V	RMS Error	Max Value	Min Value
Value	0.814	0.137	0.300	-0.514

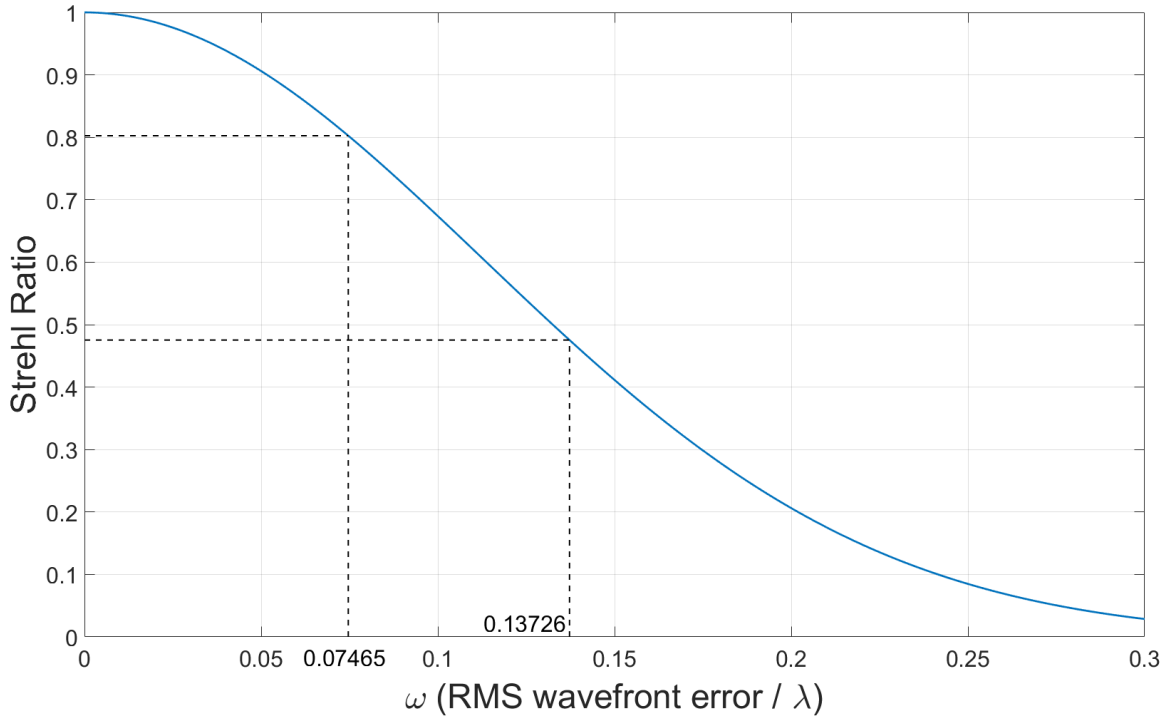

Figure 6.15: Strehl ratio - RMS wavefront error relationship showing the MTT and RT performance obtained by applying the Mahajan approximation.

6.5. Timing Measurement

The last check on the prototype's performance involves the feasibility of a timing measurement, i.e., obtaining the range from a target by evaluating the signal's time of flight. This experiment requires implementing the transceiver configuration, aligning all the relevant surfaces, and organising the experimental setups.

These steps are described in this section.

6.5.1. Transceiver implementation

As pointed out in the first place, performing the borehole in the shared mirror is the most critical passage in making the prototype a functional transceiver design.

The first choice for such a component was implementing a metallic substrate mirror, which is easy to drill with no specialised tools. However, the available COTS on the market had a too-large diameter and, therefore, were incompatible with the mechanical arrangement.

For this reason, the optical design shown in Chapter 4 presents a silica substrate shared mirror. Unfortunately, several attempts have been made after its procurement to drill the hole in the substrate, but they were all unsuccessful due to its high hardness.

A 'Plan C' has been identified and implemented to permit a timing experiment within the project's time frame: a D-shaped mirror. It has a semicircular reflective surface, as visible in Figure 6.16a, and a diagonal, longitudinal cut that makes it thin and highly versatile. By implementing this 'half' mirror, it is possible to leave enough space for the laser to pass and a partial surface for the deflection of the returning signal. Unfortunately, the only component with a suitable size had a 12.7 mm diameter, a bit shorter than the expected 16 mm spot size of the signal at that surface. This means that the practical portion of the incoming signal that will reach the detector is expected to be limited (Figure 6.16b, reducing the optical power of the returning signal. Apart from these geometrical considerations, the D-shaped mirror is covered by the exact silver coating as the nominal mirror, guaranteeing an unchanged reflectance.

The reduced dimension of the D-shaped mirror is still okay when testing the prototype on Earth at this early stage, considering the absence of limitations in the power consumption of the laser source. However, it is not preferable for future flight campaigns, where the operational concept of the prototype will be tested in a challenging environment. Therefore, the cited metallic (aluminium) mirror was procured to provide a more realistic solution. It will then be machined to reduce its diameter and perform the borehole as requested by the nominal design, permitting the integration in the Transceiver Box.

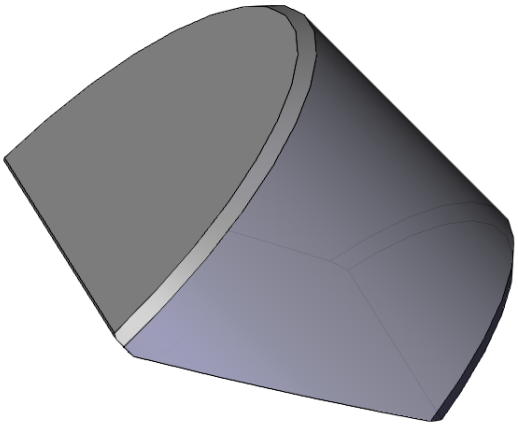

(a) ϕ12.7 mm D-shaped mirror. Figure from the Thorlabs catalogue.

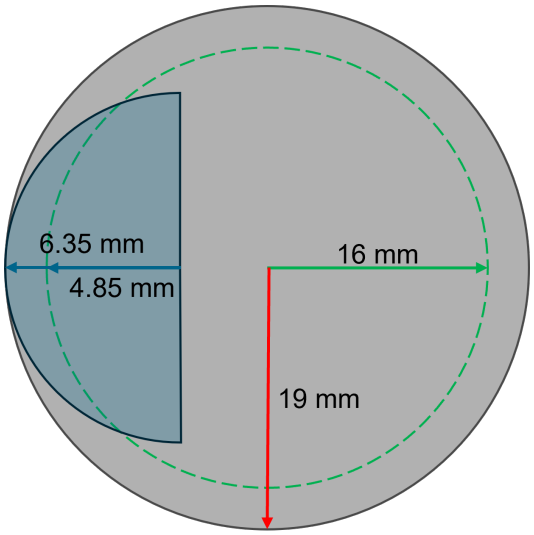

(b) Sketch of the positioning and coverage provided by nominal (grey) vs D-shaped (blue) mirror on the returning signal (green).

Figure 6.16: D-shaped mirror arrangement.

Lastly, Figure 6.17 outlines the positioning of the D-shaped mirror in the Transceiver Box.

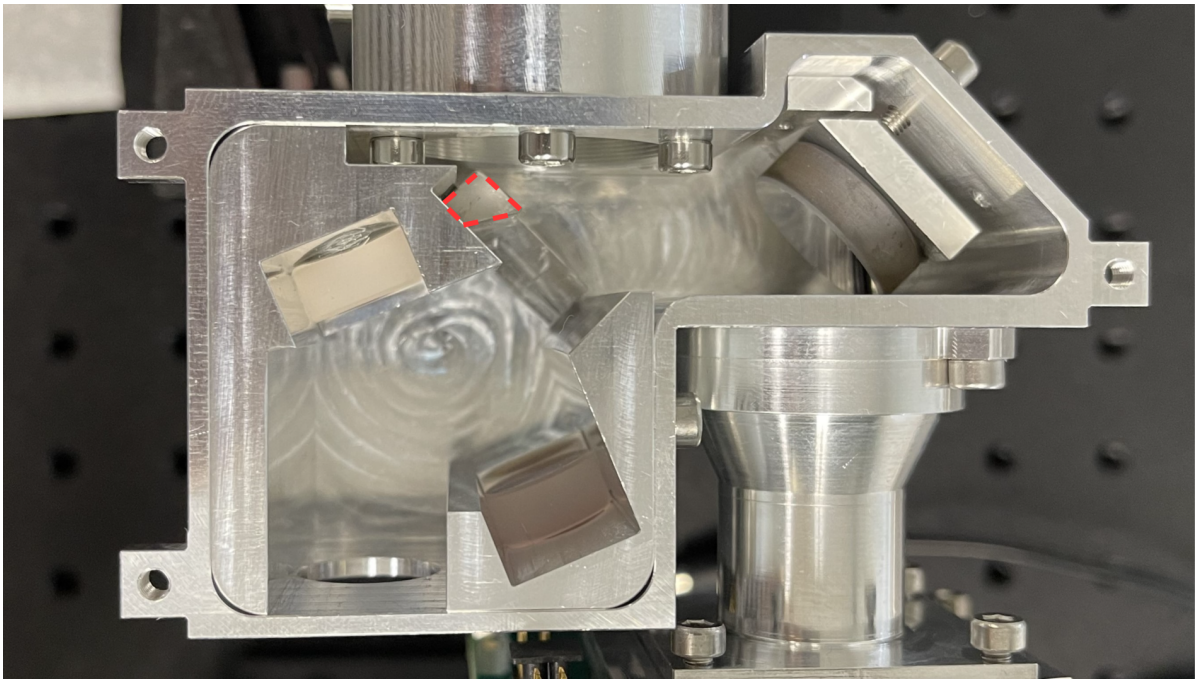

Figure 6.17: Final setup for the Transceiver Box, with an outline of the D-shaped mirror (red dotted line).

6.5.2. Transmitter-Receiver co-alignment

Now that the MTT, the TB, and the RT are mounted in their respective positions, the final step to having an operative prototype is integrating the relevant laser source and detector with the correct orientation. In other words, the transmitter and receiver sections of the prototype must be aligned with respect to the same reference to guarantee that the transmitted signal reaches the target, is captured by the receiver optics, and then focused on the active area of the detector.

The setup for this delicate part of the test campaign is shown in Figure 6.18. It is composed of:

1. 532 nm microchip laser power source;
2. Microchip laser head mounted on a precision mechanical stage;
3. Full prototype mounted on an adjustable stage to tune the height and the tilting;
4. Neutral density filters to attenuate the energy density of the laser;
5. Autocollimator (not in the picture);
6. Single-photon counting detector with two linear pixel arrays.

In addition, the picture outlines the three crucial surfaces that must be tuned to achieve the wanted alignment:

A. Front surface of the main aspheric lens of the MTT;
B. Exit surface of the laser beam;
C. Reflective surface of the adjustable mirror.

This is also the order in which the surfaces have been aligned.

Nevertheless, considering the heterogeneity of the control surfaces, the setup requires slight modifications to allow for the best alignment conditions for all of them. For example, the reflection from control surface A is faint and difficult to capture with the current arrangement. Therefore, 1) the neutral density filters are removed since the laser is not required during this process, and 2) a mirror is implemented at the centre of the lens to amplify the reflection. Figure 6.19a shows the cross-shaped signal reflected by the telescope's lens on the autocollimator's detector.

The centre of the cross is now the reference point for aligning control surfaces B and C. By implementing the neutral density filters again and removing the mirror, it is now possible to operate the laser and refine the orientation of the laser head. Nonetheless, due to the difference in magnitude between

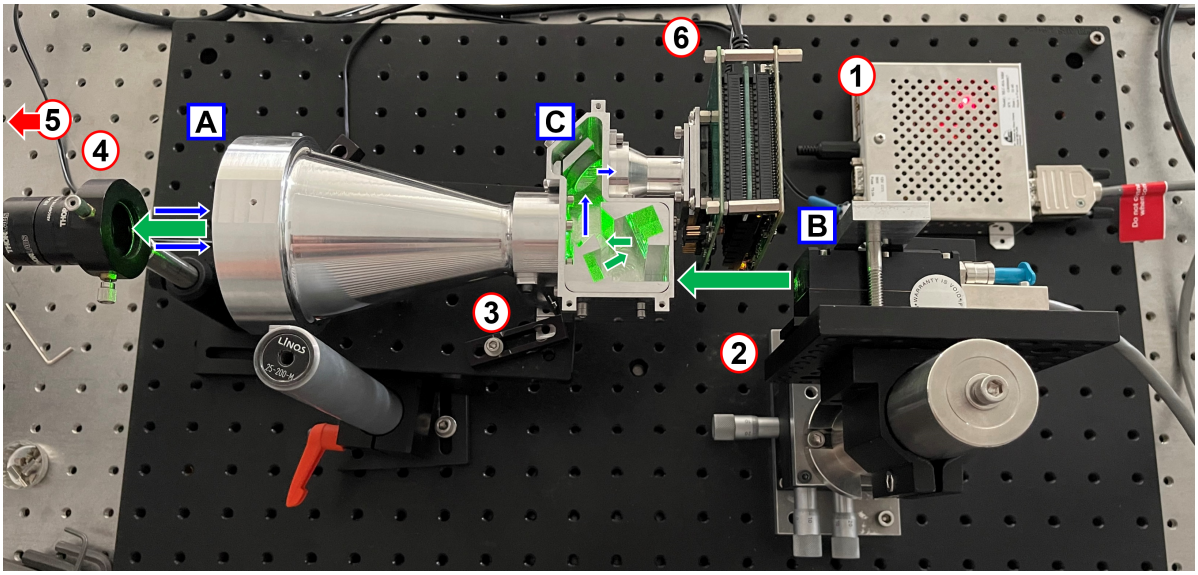

Figure 6.18: Test setup for the alignment of the prototype. Components: 1) 532-nm microchip laser power source; 2) Microchip laser head on mechanical stage; 3) Prototype; 4) Neutral density filters; 5) Autocollimator (not visible); 6) Single-photon detector. Control surfaces: A) Laser beam exit surface; B) Front surface of the main lens of MTT; C) Reflective surface of the adjustable mirror. The green arrows help visualise the propagation of the laser beam toward the target (in this case, the autocollimator); the blue arrows indicate the path of the returning signal.

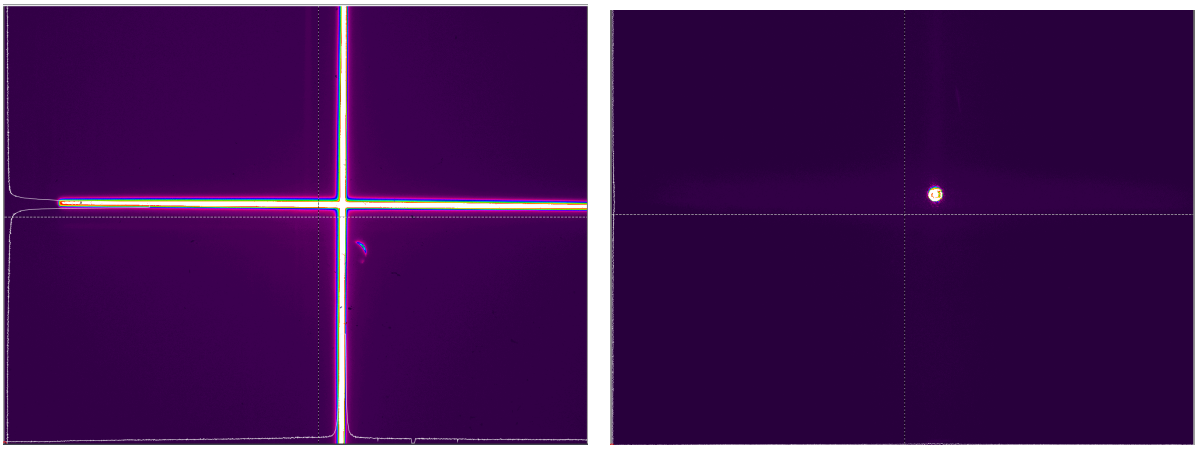

(a) Back reflection coming from the MTT integrated with the mirror. The centring of the signal on the detector is irrelevant for alignment purposes.

(b) Laser beam footprint on the autocollimator's detector. The faint cross-signal on the background comes from the back reflection of the neutral density filters.

Figure 6.19: Autocollimator signals from the MTT lens (left) and the laser head (right). The two signals overlap with sufficient precision.

the signals coming from the reflection of the plain surface A and the laser beam from surface B, it is not possible to capture an overlap like the one obtained during the band-pass filter tests (Figure 6.3).

Figure 6.19b illustrates the best alignment obtained for the laser source, where the footprint of the laser beam appears almost coincident with the cross centre from Figure 6.19a.

The adjustable mirror is the last control surface missing. As mentioned in Chapter 4, the screws behind the adjustable support act on its orientation by exerting force on the thin arm at the bottom. The top left screw modifies the tilting around the horizontal axis parallel to the reflective surface. In contrast, the other screw in the bottom right (not visible in the picture) rotates the support around the vertical axis. These two control points create momentum around a single, known axis, making the process controllable. The missing screw in the top right can be integrated at later stages to increase the stability of the support. Still, using it for alignment is not preferable because it would act on two different axes simultaneously.

The first step is to check that the adjustable mirror reflects the cross signal to the autocollimator's detector. Hence, the neutral density filters are removed again from the test setup to avoid detrimental attenuations. Figure 6.20 demonstrates the process: blocking the receiver path intermittently makes it possible to look for faint signals that appear and disappear coherently from the autocollimator's detector. Then, by regulating the screws, it is possible to refine the orientation of the adjustable mirror until the faint signal overlaps with the primary reflection from the other lenses. However, due to the disparity in magnitude of the two signals, it is impossible to show this final condition.

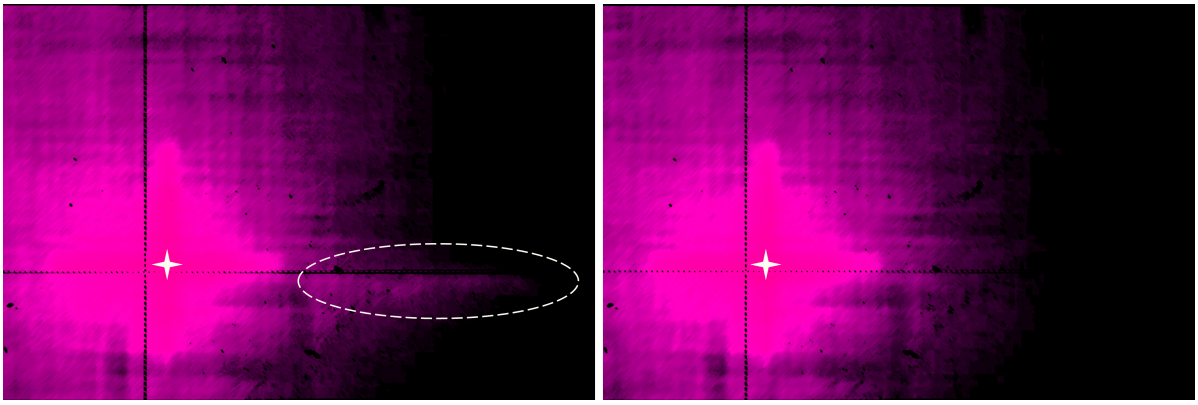

Figure 6.20: On the left: capture from the autocollimator's detector, showing the reflection coming from the telescope lenses (centred in the white star), and a faint signal apart on the right (in the dashed ellipse). On the right, a capture of the same scene but covering the adjustable mirror in the TB. The faint signal has disappeared, meaning it comes from the receiver path and is the one to align. Please note that a false-colour filter was applied to enhance the contrast.

Since it is impossible to confirm the alignment of the receiver path only with the autocollimator's detector, another strategy must be identified. The solution is to use the sensor mounted on the prototype: if it gets the signal from the autocollimator, there must be some variations when blocking the incoming light. By accessing the Graphical User Interface (GUI) of the SPAD array, it is possible to get some measurements (Figure 6.21).

The 384 vertical pixels come from the combination of the two linear arrays placed adjacent to each other. On the bottom of the picture, on the first pixel linear array, a bright row propagates over the measurements, disappearing at some point and reappearing later. These variations are observed coherently with the autocollimator's cross signal obscured and cleared again, leaving no doubts about the signal's source and the receiver's proper alignment.

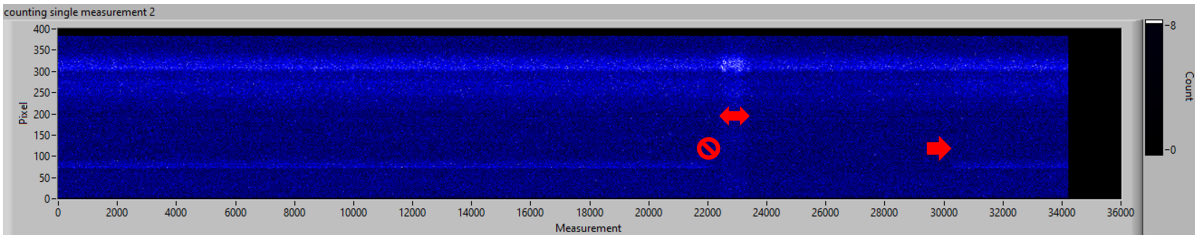

Figure 6.21: Signal coming from the SPAD arrays during the receiver alignment. The brighter spot in the bottom half propagates over the measurements until the autocollimator signal is stopped. After an auto-calibration of the software due to the variation in illumination conditions, the signal reappears once the light path is cleared.

Referring back to the same picture, some clarifications are still needed. 1) The top line seems brighter than the first one for the entire duration of the measurements. This signal is background noise from apertures in the mountings of the detector interface with the prototype; therefore, it is irrelevant. 2) Immediately after the obscuration, the signal seems brighter in the entire region. This transition is caused by the software's auto-calibration and adaptation to the new light levels on the array.

Now that the different actors are placed and aligned on the breadboard, the prototype performance in getting an actual measurement can yield some final results.

6.5.3. Detector variations and measurements

The initial plan for this test campaign was to perform a timing measurement integrating a SPAD array, in this case the SPADEye2 procured from Fraunhofer IMS. As shown in the previous section, the detector was successfully interfaced and aligned with the rest of the prototype.

However, this component is a technology demonstrator for generic purposes, and unfortunately, the GUI is not optimised to get a timing measurement as intended for the mission. After several attempts to tune the settings and obtain an unambiguous correlation between starting and returning pulses in the same measurement window, it was clear that such an experiment would not have been possible without customised software commanding the sensor.

Since such implementation is not feasible in this project's time frame, simpler detectors have been used to demonstrate the prototype's functionality.

The first attempt involves the following setup (Figure 6.22):

1. 532 nm laser source;
2. Deflecting mirror to channel the light source to the prototype;
3. Fully-mounted prototype;
4. Target, i.e. a white paper sheet not visible because at a 2.05 m distance. The range is measured by counting the borehole in the optical bench: every hole is 25.4 mm distant from the others.
5. Mechanical stage coupling a fibre at the focus of the returning signal;
6. Single-pixel APD detector;
7. Oscilloscope.

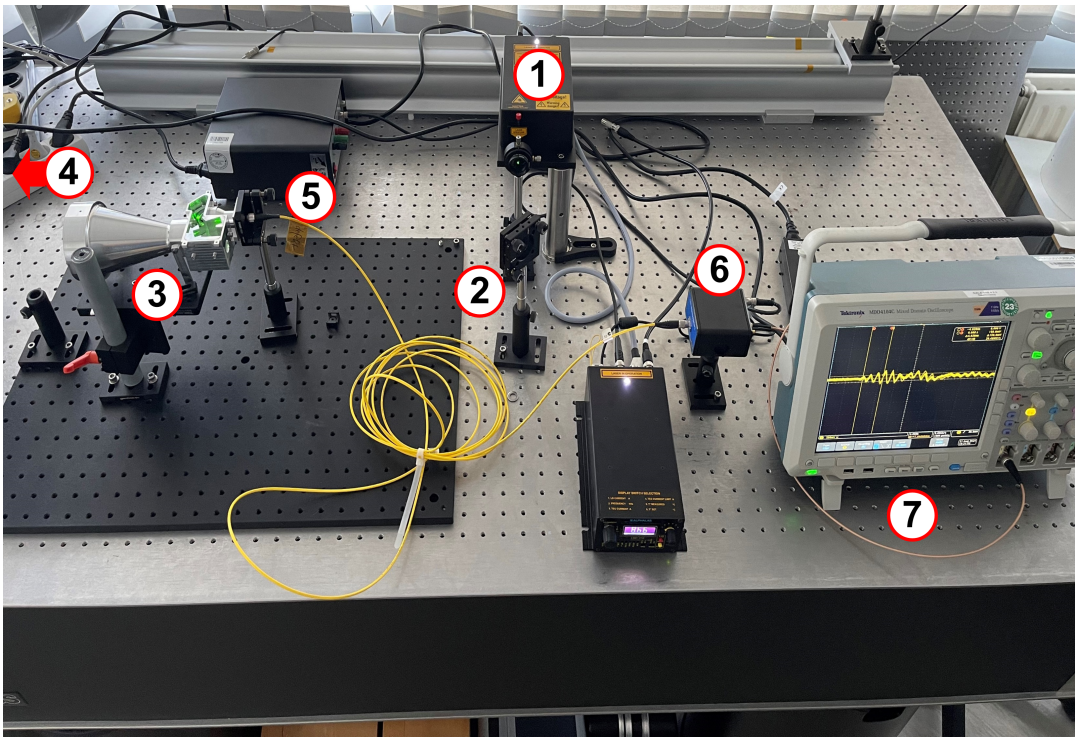

Figure 6.22: Setup for the first timing measurement. 1) 532 nm laser source; 2) Deflecting mirror; 3) Prototype; 4) White paper sheet target; 5) Optical fibre coupled with the prototype; 6) Single-pixel APD detector; 7) Oscilloscope.

The result, visible on the oscilloscope (Figure 6.23), demonstrates the possibility of collecting both starting and returning pulse, the former through the internal reflections on the prototype's structure, the latter directly reflected from the target. By measuring the period of the two signals over a score of measurements, a mean time difference of 13.65 $\pm$ 0.05 ns is retrieved. Inputting it in Equation 2.28, it is possible to get a range between the prototype and the target of:

$$H = \frac{c \cdot 13.70\ ns}{2} = 2.06\ m \tag{6.2}$$

The result is close enough to the expected value to be considered valid. In any case, the precision of the measurement is irrelevant to this project since it is linked to the detector's performance and not the prototype's. The crucial outcome is that the prototype's arrangement allows for a timing measurement, demonstrating the functionality of the altimeter.

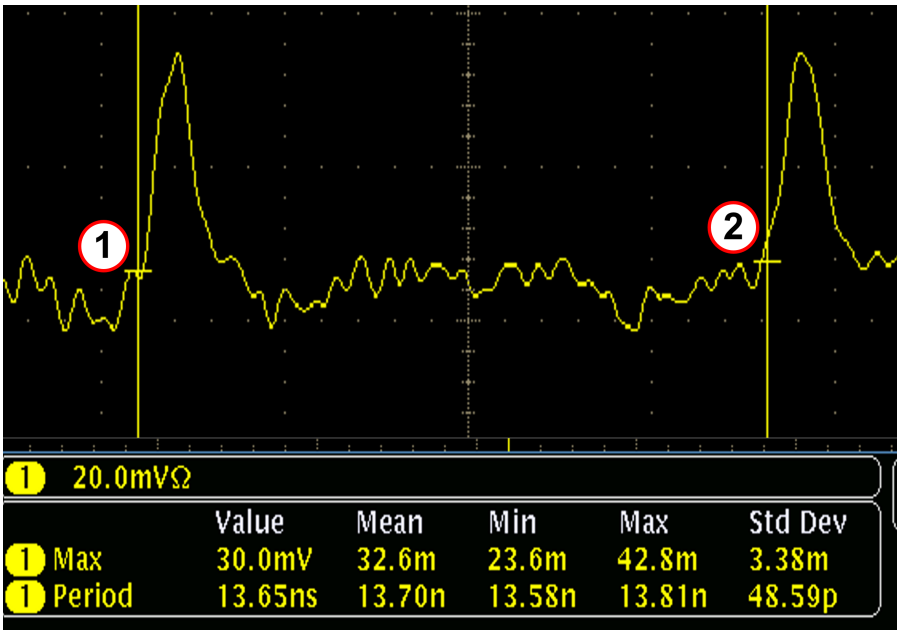

Figure 6.23: Oscilloscope capture from the APD measurements. The period between the two peaks permits the computation of the range from the target, demonstrating the functionality of the altimeter.

The same experiment is repeated with a single-pixel SPAD and a more compact laser source to prepare the prototype for a future flight campaign relevant to the mission preparation. The setup is shown in Figure 6.24, including:

1. 532 nm microchip laser power source;
2. APD to find the starting pulse (provided by a beamsplitter);
3. Fully-mounted prototype;
4. Target, i.e. a white wall further away with respect to the previous white paper sheet;
5. Single-pixel SPAD mounted on a precision mechanical stage;
6. Oscilloscope.

In this scenario, the APD plays a crucial role in determining the timing of the starting signal on the oscilloscope, which serves as a reference for the SPAD. Without this, the number of false detections would make it impossible to uniquely identify the signal from the SPAD alone.

Another consideration for this measurement is that the previous target is no longer suitable due to its proximity to the prototype, placing it within the single photon pixel's dead time. As a result, a new target, a white wall, has been selected.

The measurement results are presented in Figure 6.25. Using the green peak (1) from the APD as a reference, two additional frequent signals from the SPAD (2 and 3) are identified, which can be attributed to the starting and returning pulses from the measurements. The delay between peaks 1 and 3 is due to the difference in the light path: the APD is directly coupled with the input laser beam, while the SPAD captures the signal from internal reflections at the prototype's exit.

Taking the rising edges as a reference, it is possible to calculate the range from the target as done before:

$$H = \frac{c \cdot 28.97\ ns}{2} = 4.35\ m \tag{6.3}$$

As expected, the time difference is higher and provides a good range estimate. In this case, however, measuring the distance with another method was not possible. Again, it is irrelevant to the experiment, which still demonstrates the feasibility of collecting starting and returning pulses with the prototype.

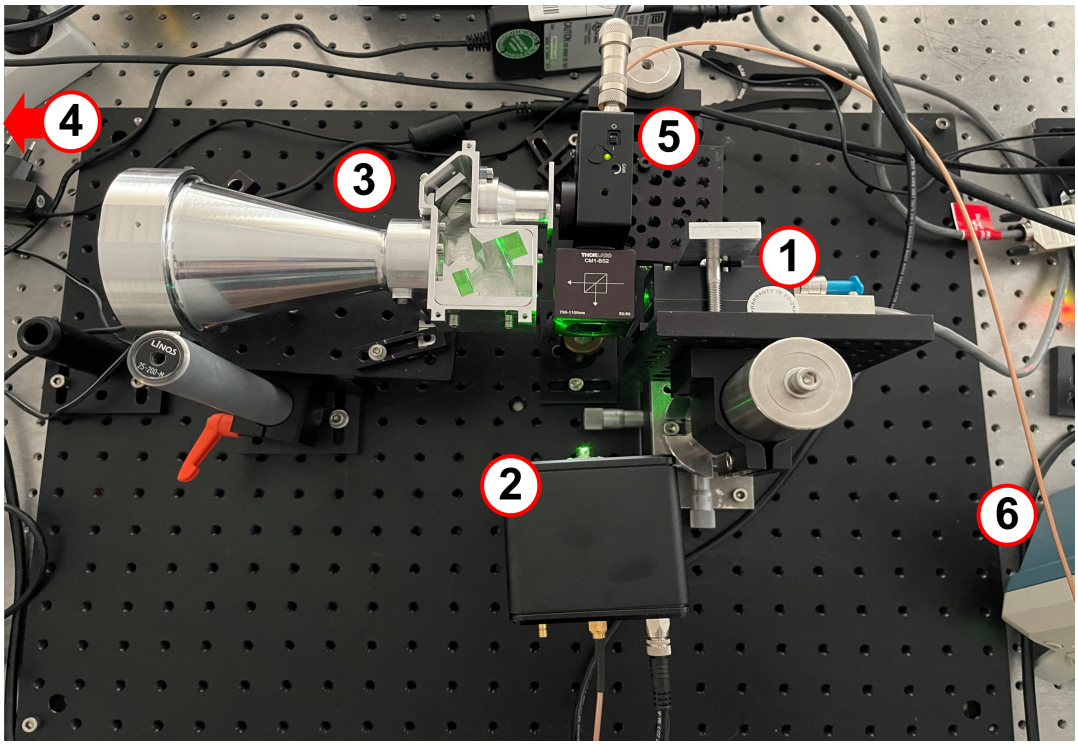

Figure 6.24: Setup for the timing measurement to prepare the flight campaign. 1) 532 nm microchip laser; 2) APD, coupled through a beamsplitter, to find a reference for the starting measurement on the oscilloscope; 3) Prototype; 4) White wall target; 5) Single-pixel SPAD; 6) Oscilloscope.

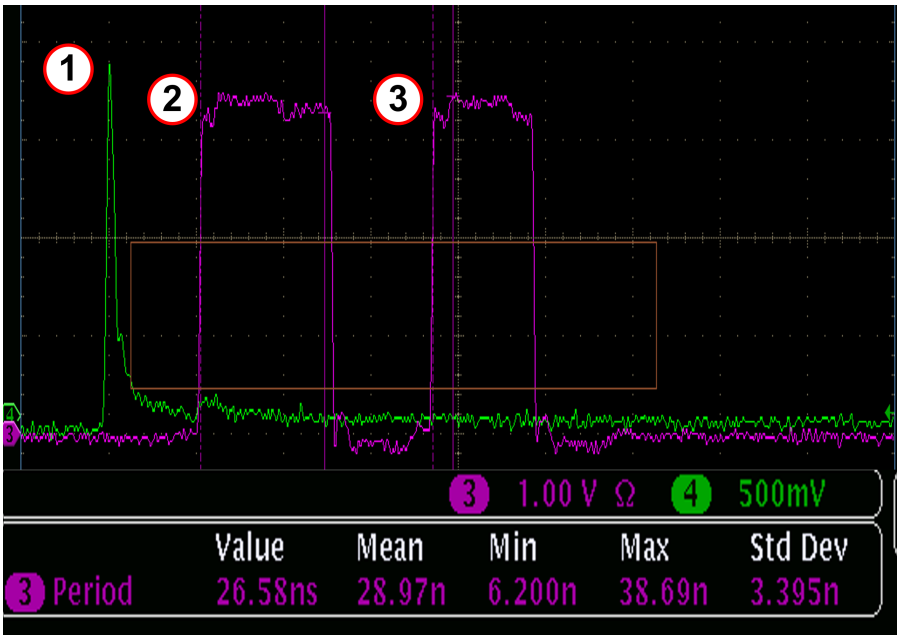

Figure 6.25: Oscilloscope capture from the SPAD measurements. The period between the two purple peaks (2 and 3) permits the computation of the range from the target, demonstrating the functionality of the altimeter with relevant equipment for the future flight campaign. The green peak (1) comes from the APD.

7

Conclusion and Next Steps

NLA is the next evolutionary step for laser altimetry in the European space scenario. Proposed by the DLR Institute of Planetary Research for the SER3N3 mission proposal, following the path paved by BELA and GALA, this conceptual miniaturised instrument aims to combine the indispensable role played by laser altimeters over the past decades in mapping the topography of rocky bodies with the urgent need for the space industry to adapt to new challenging SWaP levels of both commercial and scientific satellites.

The first mission scenario for which this instrument was designed falls within the context of an ESA OSIP call for small missions to ”address primarily exploration and science aspects” of the Moon, serving as an ideal technological demonstrator in preparation for journeys to the outer worlds of the Solar System. To successfully meet the mission requirements, NLA will need to improve the precision of topographic data provided by LOLA fitting within a 3 U volume.

This chapter exposes the achievements reached in this thesis in the effort to give NLA its first concrete shape by exploring the technologies required for its development and preparing a prototype to characterise them in the laboratory preliminarily. Additionally, it recommends the most compelling future steps to be addressed to enhance the Technology Readiness Level (TRL) of the instrument and bring it closer to a possible launch.

7.1. Results

This thesis explored the miniaturisation of laser altimeters for CubeSat missions, a challenge that required adapting existing technologies and developing new strategies to meet stringent SWaP constraints. The research and testing conducted have made significant progress in paving the technological roadmap for this evolution. In particular, the leitmotiv feeding this study is the research question posed at the beginning of this project, i.e.:

To what extent can a Laser Altimeter be miniaturised for use in CubeSat missions aimed at topographic mapping?

which the thesis attempted to answer from the perspectives of the various subquestions.

1. *Which technologies are necessary to adapt classical laser altimetry techniques to CubeSats?*
   The thesis aimed at exploring the basic principles behind the working processes of laser altimeters, namely the transmission of a laser pulse through optical elements and its consequent reception using a photon detector, and identifying the most compelling strategies needed to fit an instrument with the constraints for a small mission.

   The introduction of single photon-counting detectors, equipped with SPADs, represents a groundbreaking advancement for such miniaturised instruments because of the savings in power and consequent reduction in weight and size granted by the need for a lower number of pixels and data rate for the detector, and energy levels of the laser source.

However, this is not enough on its own. Additional measures like implementing a transceiver design, where the optical elements of the transmitter and receiver sections are partly shared, are required to shrink the instrument in less than 3 U.

These enhancements will guarantee a never-so-advantageous compromise between the size performance and the power performance of a laser altimeter dedicated to topographic ranging.

2. *Which can be a functional optical design choice for a miniaturised laser altimeter for topographic mapping?*
The first step to prove the feasibility of such technology in ranging applications and increase its TRL is to identify a suitable optical design for the instrument. This includes the optical elements required to expand the laser beam according to the geometrical specifications of the orbits and focus it on the detector plane once bounced back, as well as their arrangement, which must fit within the limited space allocated in the microsatellite.

   In this thesis, a 2 U transceiver design has been identified through a trade-off analysis. The process was approached from two different ends: on the one hand, identifying the critical mission requirements with which to evaluate the candidates. The final scoring criteria encompassed the optics arrangement, the laser-detector cross-coupling, the footprint size, the transmitter-receiver co-alignment, and the transmittance losses. On the other hand, by proposing several optical designs and narrowing down the selection according to the mission constraints and the limitations of this project.

   In the end, the selected design, which presents an iteration of the transmitter path with two 45° inclined mirrors, stood out in providing a footprint size in the range allowed by the requirements, reducing the probability of damage to the detector due to internal reflections from the laser, and guaranteeing a more stable co-alignment between the transmitter and receiver paths.

   The proposed optimum design is then integrated into the CATIA environment to shape a prototype around it. The proposed modular arrangement, which has the advantage of being easier to change in case of future improvements, has three main components: the Main Telescope Tube (MTT), holding the principal lenses, the Transceiver Box (TB), carrying the mirror for both receiver and transmitter and the Receiver Tube (RT), containing the band-pass filter and the last lenses required to suppress the background noise and focus the returning signal on the sensor, respectively. The in-house workshop manufactured the design.

3. *What are the preliminary performance parameters of such a design choice?*
A test campaign has been conducted on the prototype to demonstrate its performance.

   First, a possible tilting of the band-pass filter was evaluated to increase the total transmittance of the optics, which was demonstrated below the mission's requirements during the trade-off analysis. By changing the angle of incidence to $\pm$ 1.5°, it was possible to enhance the transmittance above 90% for the specific laser wavelength, which is expected to be used also during the mission.

   Then, the test campaign aimed to demonstrate compliance with some of the performance from the trade-off analysis. In the time frame of this project, the most important and straightforward criterion was the footprint, which was assessed by evaluating the predictability of the transmitter's expansion performance. An artificial waist was induced after the exiting beam to obtain a hyperbolic fitting, from which it was possible to get the geometrical features of the exiting beam. Despite the lack of measurements in the Rayleigh range, relevant simulations on Zemax demonstrated the coherence of measured and simulated results, proving that the optical arrangement will induce the wanted expansion once the nominal laser source is implemented.

   Lastly, the final focus of the experiments was to assess the prototype's functionality, evaluating the feasibility of a timing measurement and the corresponding signal quality. For the latter, waveform distortions were investigated for both transmitter and receiver. The transmitter is aberration-free, while the receiver presents a slightly decreased but acceptable performance. For the timing measurement, the prototype was accurately aligned with an autocollimator and then used to get the range on a single-pixel APD first, and on a single-pixel SPAD then. Without looking at the accuracy of such measurements, the prototype managed to impress on the detectors both starting and returning pulses, demonstrating its functionality as a miniaturised laser altimeter.

The final answer this thesis can provide to the overarching research question is that topographic laser altimeters are on the verge of reaching their next evolutionary stage. With targeted advancements in critical technologies, the coming years will be pivotal for bringing these essential instruments into the spotlight of the space industry, including their potential use in smaller satellites. NLA and SER3NE, with a launch planned by the end of this decade, could mark the first steps in this direction. Although the developed prototype is just one of many possible configurations for a functional instrument, the demonstration of its functionality was successful, effectively showcasing its capabilities while integrating the necessary innovative technologies. This work accelerated the process of flying a miniaturised laser altimeter for topographic mapping in the future.

7.2. Future Recommendations

During the time of this project, SER3NE has been selected by ESA as one of the five candidates (out of sixty) for pre-phase A studies. This achievement translates into a strict development schedule for the mission's payload, including NLA, that will take place over the months after the conclusion of this thesis.

Therefore, the contribution of this work will immediately be beneficial for advancing the knowledge about photon-counting altimeters and increasing the TRL of the instrument. Many aspects have been covered, but a score of questions and required verifications remain at the margins of the provided answers. A summary of the current status is visible with the compliance matrix presented in Table 7.1.

Some of the mentioned improvements will already be implemented in preparation for the flight campaign expected in November 2024, like the metallic drilled mirror; others, like the implementation of the SPAD array, the development of a customised laser source, and the modification of the receiver's lenses (mentioned in Chapter 4), will be investigated in collaboration with industries throughout the pre-phase A.

In any case, the DLR Institute of Planetary Research shall explore the benefit that such a miniaturised instrument could bring to the future of space exploration. With such limited demands, NLA can represent not only a technology demonstrator to characterise future landing sites on the Moon but also an agile, ready-to-go instrument to load on flagship missions for the icy moons of the outer Solar System, autonomous microsatellites, or piggyback CubeSats for larger missions. It can represent the springboard for the imminent revolution in laser altimetry and a milestone for the future of the space industry.

Table 7.1: Compliance matrix for the prototype studied in this project. A green level means that the parameter has been investigated successfully and with enough precision; a yellow level implies further studies to refine the investigation; an orange level delivers the urge to assess the parameter because it has not been explored during the test campaign.

Performance parameter	Level	Comment
Compactness		The compactness has been demonstrated by fitting the prototype in 2 U. The compliance with the assessment criteria in the trade-off analysis is not relevant at this stage, where the mounting is rudimental and unsuitable for a flying instrument. The next step will improve the interface with the relevant subsystems to better understand the arrangement inside the actual instrument.
Tx-Rx Cross-Coupling		To verify the performance in such criterion, it is required to implement a laser source, a detector, and a shared mirror more coherent with the simulations. This was not possible during this project, but it is paramount for the future stages.
Footprint Size		The expansion performance has been proven during the current test campaign. Refining the experiment, including more measurements in the Rayleigh range and implementing the actual laser source, could be beneficial to improve reliability.
Tx-Rx Co-alignment		To verify the performance in such criterion, it is required to implement a laser source, a detector, and a shared mirror more coherent with the simulations. This was not possible during this project, but it is paramount for the future stages.
Transmittance Losses		The transmittance is compliant with the requirement after tilting the band-pass filter. For future stages, the filter can be inclined or replaced with a customised one to reduce complexity. Implementing the drilled shared mirror would permit an estimate of the actual optical design's transmittance.
Functionality		The instrument has been demonstrated functional as laser altimeter with the current optical design. The same must be done in a relevant measurement environment, e.g. during a flight campaign, and with a customised laser source and detector.
Single photon counting		The possibility of using single photon counting detection was demonstrated for a single-pixel detector, which does not enable topographic measurements at the same level as the current technology. The implementation of a SPAD array is required for future studies

Bibliography

[1] Kay Lingenauber et al. “Miniaturized Laser Altimeter for Small Satellite Applications”. In: *Deutscher Luft- und Raumfahrtkongress 2023*. Sept. 2023. URL: https://elib.dlr.de/200264/.

[2] Hui Zhou et al. “An overview of the Laser Ranging Method of space laser altimeter”. In: *Infrared Physics & Technology* 86 (2017), pp. 147–158. DOI: 10.1016/j.infrared.2017.09.011.

[3] William M. Kaula et al. “Apollo laser altimetry and inferences as to lunar structure”. In: *Lunar Science Conference, 5th, Houston, Tex., March 18-22, 1974, Proceedings*. Vol. 3. Pergamon Press, Inc. New York, 1974, pp. 3049–3058.

[4] NASA. *Clementine Laser Image Detection and Ranging (LIDAR) System*. Retrevied on 21.01.2024. URL: https://nssdc.gsfc.nasa.gov/nmc/experiment/display.action?id=1994-004A-04.

[5] JAXA. *KAGUYA (SELENE) Laser Altimeter*. Retrevied on 21.01.2024. URL: https://www.selene.jaxa.jp/en/equipment/lalt_e.htm.

[6] NASA. *Topography of Mars*. Retrieved on 31.05.2024. URL: https://science.nasa.gov/resource/topography-of-mars/.

[7] Indian Space Research Organization. *Chandrayaan-1*. Retrevied on 21.01.2024. URL: https://www.isro.gov.in/Chandrayaan_1.html.

[8] NASA Goddard. *The LRO instruments*. Retrevied on 21.01.2024. URL: https://lunar.gsfc.nasa.gov/instruments.html.

[9] NASA. *MESSENGER - MErcury Surface, Space ENvironment, GEochemistry, and Ranging*. Retrevied on 21.01.2024. URL: https://science.nasa.gov/mission/messenger/.

[10] ESA. *BepiColombo*. Retrevied on 21.01.2024. URL: https://www.esa.int/Science_Exploration/Space_Science/BepiColombo.

[11] NASA - Jet Propulsion Laboratory. *Mars Global Surveyor*. Retrevied on 22.01.2024. URL: https://www.jpl.nasa.gov/missions/mars-global-surveyor.

[12] DLR. *The GALA altimeter*. Retrevied on 22.01.2024. URL: https://www.dlr.de/en/research-and-transfer/projects-and-missions/juice/the-gala-altimeter.

[13] NASA. *NEAR Shoemaker*. Retrevied on 22.01.2024. URL: https://science.nasa.gov/mission/near-shoemaker/.

[14] Takahide Mizuno et al. “Development of LIDAR for deep space mission HAYABUSA”. In: *JAXA* (2005). URL: https://laser-sensing.jp/ilrc23_CD1a2b3c/ILRC23/90-14.pdf.

[15] Takahide Mizuno et al. “Development of the Laser Altimeter (LIDAR) for Hayabusa2”. In: *Space Science Reviews* 208.1–4 (2016), pp. 33–47. DOI: 10.1007/s11214-015-0231-2.

[16] Michael G. Daly et al. “The OSIRIS-Rex Laser Altimeter (OLA) investigation and Instrument”. In: *Space Science Reviews* 212.1–2 (2017), pp. 899–924. DOI: 10.1007/s11214-017-0375-3.

[17] Observatoire Côte d’Azur. *HERA mission*. Retrevied on 22.01.2024. URL: https://www.hera-mission.space/.

[18] Robert S. Afzal et al. “The geoscience laser altimeter system (GLAS) laser transmitter”. In: *IEEE Journal of Selected Topics in Quantum Electronics* 13.3 (2007), pp. 511–536. DOI: 10.1109/jstqe.2007.896051.

[19] NASA. *ICESat-2 Mission*. Retrevied on 25.01.2024. URL: https://icesat-2.gsfc.nasa.gov/mission.

[20] ESA. *ALADIN overview*. Retrevied on 25.01.2024. URL: https://earth.esa.int/eogateway/instruments/aladin/description.

[21] Damian H. Evans et al. “Uncovering archaeological landscapes at Angkor using Lidar”. In: *Proceedings of the National Academy of Sciences* 110.31 (July 2013), pp. 12595–12600. DOI: 10.1073/pnas.1306539110.

[22] Emily Clements et al. “Nanosatellite Optical Downlink Experiment: Design, simulation, and Prototyping”. In: *Optical Engineering* 55.11 (Sept. 2016), p. 111610. DOI: 10.1117/1.oe.55.11.111610.

[23] John Cavanaugh. “The Advanced Topographic Laser Altimeter System (ATLAS) for NASA’s Ice Cloud and Land Elevation Satellite-2 (ICESat-2). Design, Development, and On-Orbit Performance”. In: *MSS Active E-O Systems Electro-Optical Infrared Countermeasures (IRCM)Conference*. 2019. URL: https://ntrs.nasa.gov/api/citations/20190014038/downloads/20190014038.pdf.

[24] eoPortal. *ICESat (Ice, Cloud and Land Elevation Satellite)*. Retrieved on 13.03.2024. URL: https://www.eoportal.org/satellite-missions/icesat#glas-geoscience-laser-altimeter-system.

[25] NASA. *ICESat-2 Technical Specs*. Retrieved on 03.06.2024. URL: https://icesat-2.gsfc.nasa.gov/science/specs.

[26] Kay Lingenauber et al. “The Ganymede Laser Altimeter (GALA) on ESA’s JUICE Mission: Overview of the Instrument Design”. In: Nov. 2014.

[27] ESA. *Juice, Exploring the emergence of habitable worlds around gas giants, Definition Study Report*. Retrieved on 15.01.2024. URL: https://sci.esa.int/documents/33960/35865/1567260128466-JUICE_Red_Book_i1.0.pdf.

[28] Nicholas Thomas et al. “The BepiColombo Laser Altimeter”. In: *Space Science Reviews* 217.1 (Feb. 2021). DOI: 10.1007/s11214-021-00794-y.

[29] Haris Riris et al. “The Lunar Orbiter Laser Altimeter (LOLA) on NASA’s Lunar Reconnaissance Orbiter (LRO) mission”. In: *ICSO 2010 International Conference on Space Optics*. 2010.

[30] Hiroshi Araki et al. “Lunar Global Shape and Polar Topography Derived from Kaguya-LALT Laser Altimetry”. In: *Science* 323 (2009), pp. 897–900. DOI: 0.1126/science.1164146.

[31] Teiji Kase. *100mJ,1Hz Nd:YAG laser using Laser ALTimeter (LALT) for SELENE lunar orbiter*. Retrieved on 19.01.2024. URL: https://photonics.gsfc.nasa.gov/tva/meldoc/ESA-NASA/2006/WEDNESDAY/NEC-T-KASE.pdf.

[32] Keigo Enya et al. “The Ganymede Laser Altimeter (GALA) for the Jupiter Icy Moons Explorer (JUICE): Mission, science, and instrumentation of its receiver modules”. In: *Advances in Space Research* 69 (2022), pp. 2283–2304. DOI: https://doi.org/10.1016/j.asr.2021.11.036.

[33] Anthony W. Yu et al. “THE LUNAR ORBITER LASER ALTIMETER (LOLA) LASER TRANSMITTER”. In: *Nasa Goddard Space Flight Center* (2008). Retrieved on 03.06.2024.

[34] Hiroshi Araki et al. “Present Status and Preliminary Results of the Lunar Topography by KAGUYA-LALT Mission”. In: *Lunar and Planetary Science XXXIX*. 2008.

[35] Hannah Goldberg et al. “The ESA HERA Mission and Its Planetary Altimeter — Learning to Deflect Asteroids”. In: *Space-based Lidar Remote Sensing Techniques and Emerging Technologies. LIDAR 2023.* 2024. DOI: https://doi-org.tudelft.idm.oclc.org/10.1007/978-3-031-53618-2_12.

[36] Nicole G. Dias et al. “HERA Mission LIDAR Altimeter Implementation”. In: *10th EASN 2020, Material Science and Engineering*. 2020. DOI: doi:10.1088/1757-899X/1024/1/012112.

[37] Paulo Gordo et al. “HELENA - HERA LIDAR ENGINEERING MODEL ALTIMETER DESIGN”. In: *6th IAA Planetary Defense Conference*. Poster. 2019.

[38] Roger Walker. *CubeSats: State-of-the-art and future potential for small low-cost science missions*. 2018. URL: https://www.cosmos.esa.int/documents/13627/1820136/1520_CubeSats%20ESA%20SCI%20Workshop%20Nov%202018.pdf/a78870f2-837c-5fb9-289a-b9378fa9609f.

[39] BRYCE TECH. *Smallsats by the Numbers 2023*. Retrevied on 25.01.2024. URL: https://brycetech.com/reports/report-documents/Bryce_Smallsats_2023.pdf.

[40] Daniel Selva and David Krejci. “A survey and assessment of the capabilities of Cubesats for Earth Observation”. In: *Acta Astronautica* 74 (May 2012), pp. 50–68. DOI: 10.1016/j.actaastro.2011.12.014.

[41] Jonathan Bruzzi et al. “A Compact Laser Altimeter for Spacecraft Landing Applications”. In: *Johns Hopkins APL Technical Digest (Applied Physics Laboratory)* 30 (Jan. 2012), pp. 331–345.

[42] Patricia Martín Pimentel et al. “Cube Laser Communication Terminal (cubelct) state of the art”. In: *Acta Astronautica* 211 (Oct. 2023), pp. 326–332. DOI: 10.1016/j.actaastro.2023.06.026.

[43] NASA Jet Propulsion Laboratory. *Lunar Flashlight*. Retrevied on 26.01.2024. URL: https://www.jpl.nasa.gov/missions/lunar-flashlight.

[44] Guangning Yang et al. “Adaptive Wavelength Scanning Lidar (AWSL) for 3D mapping from space”. In: *IGARSS 2022 - 2022 IEEE International Geoscience and Remote Sensing Symposium* (July 2022). DOI: 10.1109/igarss46834.2022.9884418.

[45] Mark Storm et al. “Cubesat Lidar Concepts for Ranging, Topology, Sample Capture, Surface, and Atmospheric Science”. In: 2017. URL: https://digitalcommons.usu.edu/smallsat/2017/all2017/250/.

[46] Kay Lingenauber et al. “A miniaturized single-photon counting laser altimeters for space applications”. In: *SPIE Optics and Photonics*. 2024.

[47] Gartner. *Information Technology Glossary: Laser*. Retrevied on 02.02.2024. URL: https://www.gartner.com/en/information-technology/glossary/laser#:~:text=A%20device%20that%20emits%20a,directions%20for%20the%20emitted%20light..

[48] CVI Melles Griot. “Gaussian Beam Optics”. In: *Technical Guide* (2009).

[49] Rudolf Saathof. *Laser Satellite Communications I*. Lecture slides, Academic Year 2023/2024.

[50] Sidney A. Self. “Focusing of spherical gaussian beams”. In: *Applied Optics* 22.5 (Mar. 1983), p. 658. DOI: 10.1364/ao.22.000658.

[51] Koji Sugioka. *Handbook of Laser Micro- and Nano-Engineering*. Springer, 2021. DOI: https://doi.org/10.1007/978-3-030-63647-0.

[52] Telescopeoptics.net. *Strehl Ratio*. Retrieved on 02.07.2024. URL: https://www.telescope-optics.net/Strehl.htm.

[53] Vivek Gualani. *Design and Development of a LISA photoreceiver and Optical Ground Support Equipment (OGSE)*. 2020.

[54] Nicholas Tsoulfanidis. *Measurements and Detection Radiation*. 2nd edition. Taylor Francis, 1995.

[55] Andreas Ulrich and Martin Pfennigbauer. “Linear Lidar versus Geiger-mode lidar: Impact on data properties and data quality”. In: *SPIE Proceedings* (May 2016). DOI: 10.1117/12.2223586.

[56] Binhao Wang and Jifang Mu. “High-speed Si-Ge Avalanche Photodiodes”. In: *PhotoniX* 3.1 (2022). DOI: 10.1186/s43074-022-00052-6.

[57] Yuri Musienko. “Advances in Avalanche Photodiodes”. In: *Proceedings of the Workshop of the INFN ELOISATRON Project: Innovative Detectors for Supercolliders, Erice, Italy*. 2003, p. 427.

[58] Sergio Cova et al. “Avalanche photodiodes and quenching circuits for single-photon detection”. In: *Applied Optics* 35.12 (Apr. 1996), p. 1956. DOI: 10.1364/ao.35.001956.

[59] Stella Meiré. *Experimental Laboratory Setup for Single-Photon Counting Laser Altimetry in Planetary Research*. 2023.

[60] ESA. *Small Missions for Exploration – Destination the Moon*. 2023. URL: https://ideas.esa.int/servlet/hype/IMT?documentId=9904aa3d71cbae0c8d3d86503095f607&userAction=Browse&templateName=.

[61] Hamid Hemmadi et al. *Deep Space Optical Communications*. Transceiver Design. John Wiley and Sons, Inc., 2005. Chap. 5. URL: https://descanso.jpl.nasa.gov/monograph/series7/Descanso_7_Full_Version_rev.pdf.

[62] Bastian Schwarz et al. “Laser-induced damage threshold of camera sensors and micro - optoelectromechanical systems”. In: *Optical Engineering* 56 (2017). DOI: 10.1117/1.OE.56.3.034108.

[63] Schott Advanced Optics. *N-BK7*. Retrieved on 06.05.2024. URL: https://www.schott.com/shop/advanced-optics/en/Optical-Glass/N-BK7/c/glass-N-BK7.

[64] Schott Advanced Optics. *N-SF11*. Retrieved on 06.05.2024. URL: https://www.schott.com/shop/advanced-optics/en/Optical-Glass/N-SF11/c/glass-N-SF11.

[65] Schott Advanced Optics. *TIE-35: Transmittance of optical glass*. Retrieved on 06.05.2024. URL: https://www.schott.com/shop/medias/schott-tie-35-transmittance-of-optical-glass-eng.pdf?context=bWFzdGVyfHJvb3R8NzYxOTY3fGFwcGxpY2F0aW9uL3BkZnxoM2MvaGQ1Lzg4MTc0MDk5MTY5NTgucGRmfGY0ZWVlNWRmMDczYjliNjA0MWJiMDg3NTlkMDZhODRmZmNmNGNiOTNjOTg0Y2ZiMjY1YmMwNDUwZWU2NjU4NGE.

[66] Fraunhofer Institute for Microelectronic circuits and Systems IMS. *SPADEYE2 – CMOS LIDAR SENSOR*. Retrieved on 29.07.2024. URL: https://www.ims.fraunhofer.de/content/dam/ims/de/documents/Downloads/SPADeye2.pdf.

[67] Alluxa. *Flat top, Ultra-Narrow Band Pass Optical Filters Using Plasma Deposited Hard Oxide Coatings*. Retrieved on 13.06.2024. URL: https://www.lasercomponents.com/fileadmin/user_upload/home/Datasheets/alluxa/ultra-narrow-bandpass-filter.pdf.

[68] Optocraft. *Laser beam characterization using a SHSLab wave-front sensor*. Retrieved on 01.08.2024. URL: https://www.optocraft.de/wp-content/uploads/2021/08/AppNote-SHSLab-Laser-beam-characterization.pdf.

[69] Optocraft. *SHSInspect for multi-functional optics testing*. Retrieved on 30.07.2024. URL: https://www.optocraft.de/wp-content/uploads/2021/08/AppNote-SHSInspect-Multifunctional-optics-testing.pdf.

A

Beam Expansion Test Captures

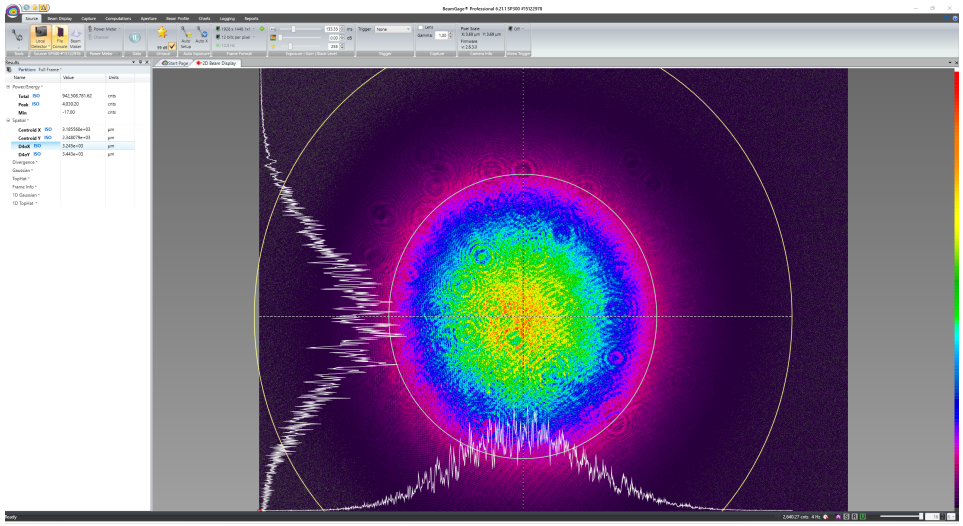

Figure A.1: Beam section captured at 65 mm from the focusing lens surface.

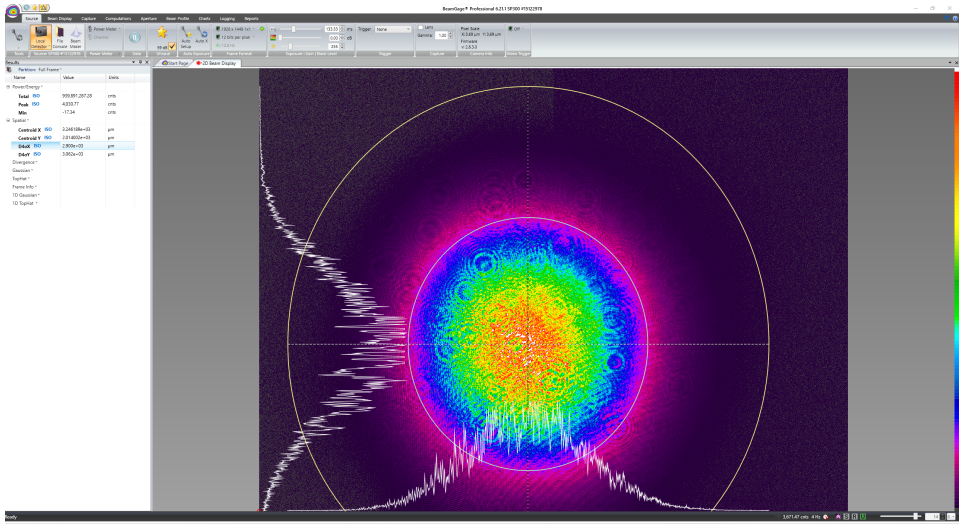

Figure A.2: Beam section captured at 75 mm from the focusing lens surface.

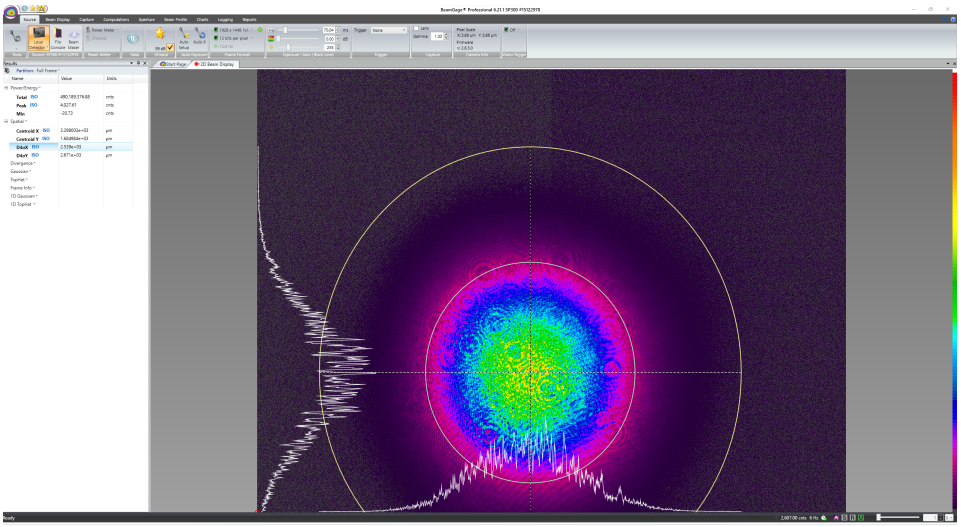

Figure A.3: Beam section captured at 85 mm from the focusing lens surface.

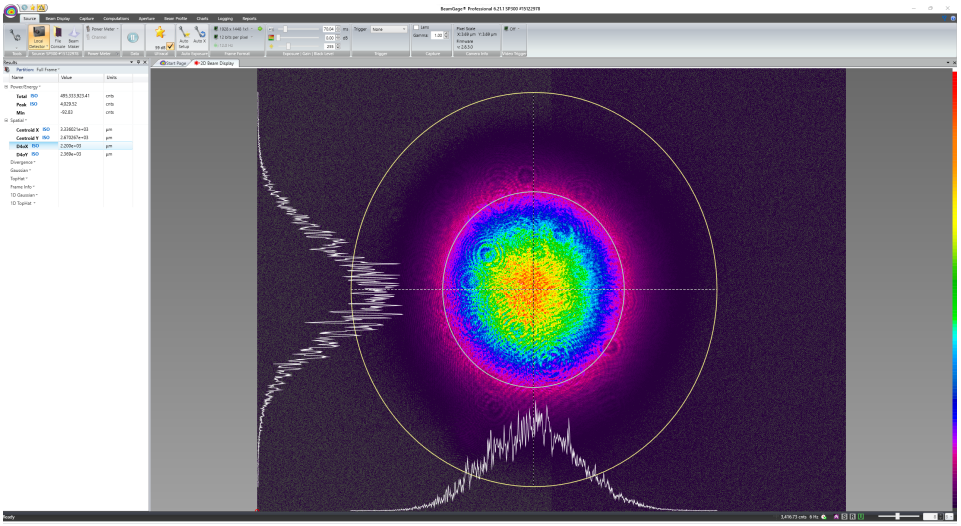

Figure A.4: Beam section captured at 95 mm from the focusing lens surface.

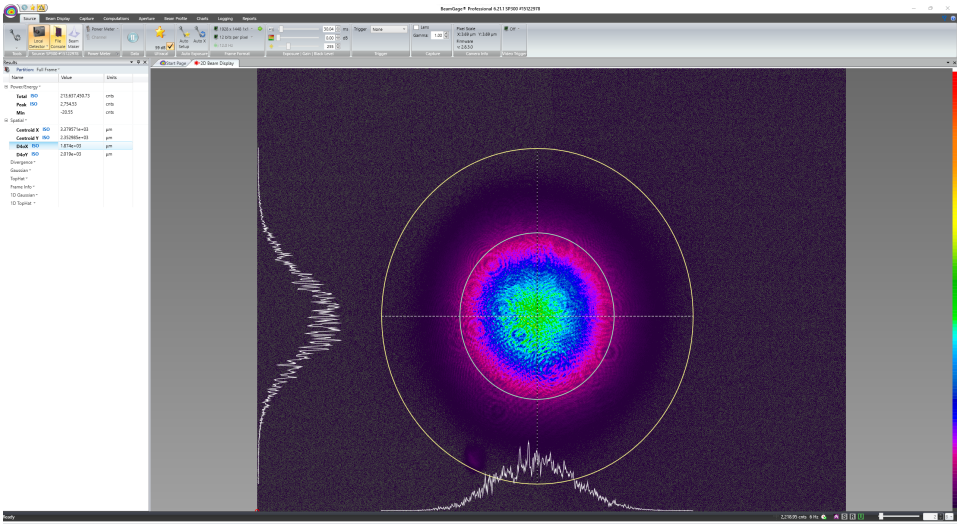

Figure A.5: Beam section captured at 105 mm from the focusing lens surface.

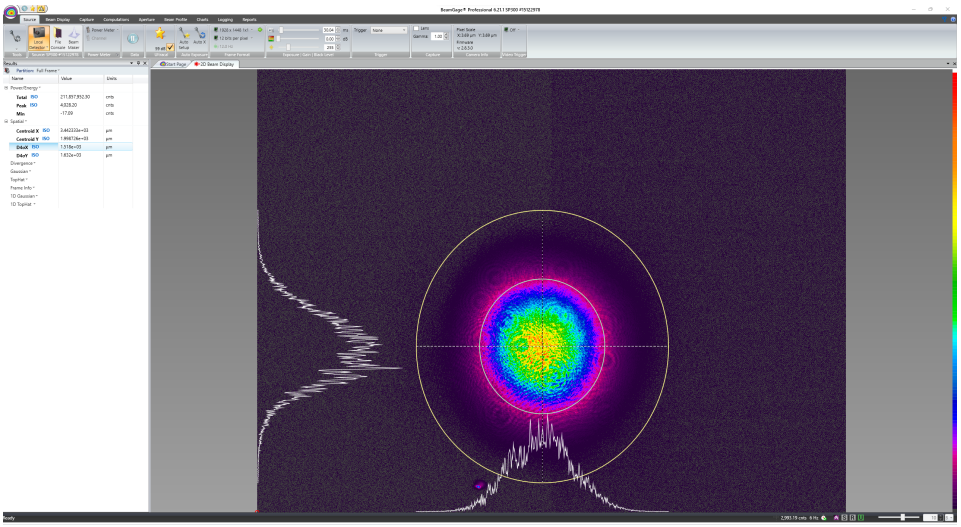

Figure A.6: Beam section captured at 115 mm from the focusing lens surface.

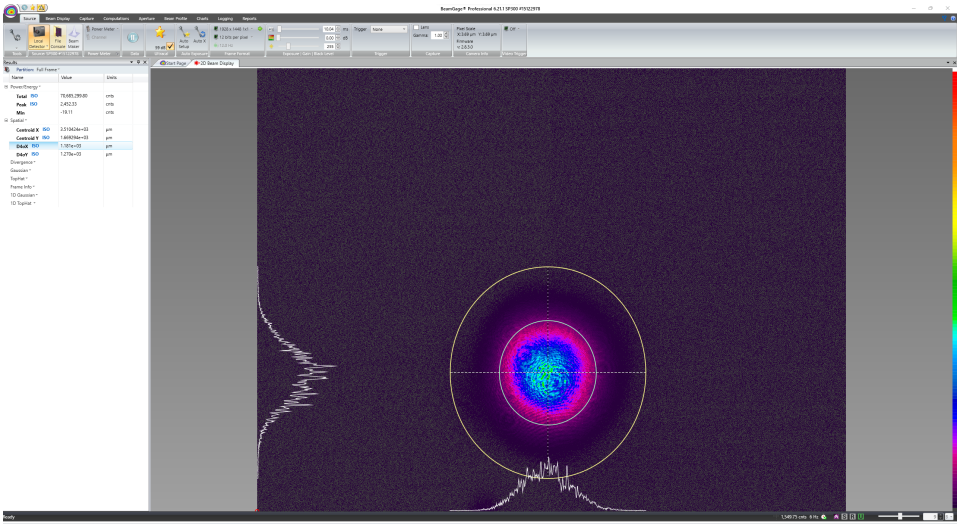

Figure A.7: Beam section captured at 125 mm from the focusing lens surface.

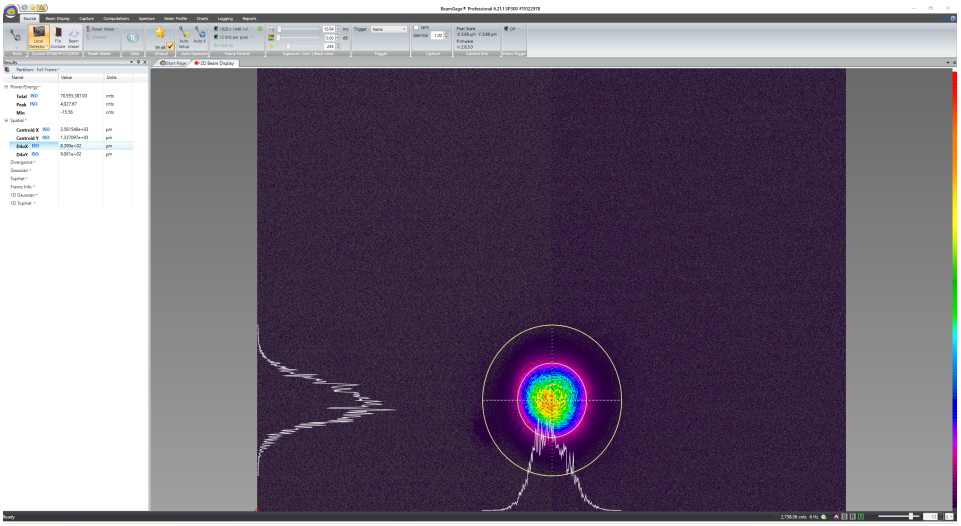

Figure A.8: Beam section captured at 135 mm from the focusing lens surface.

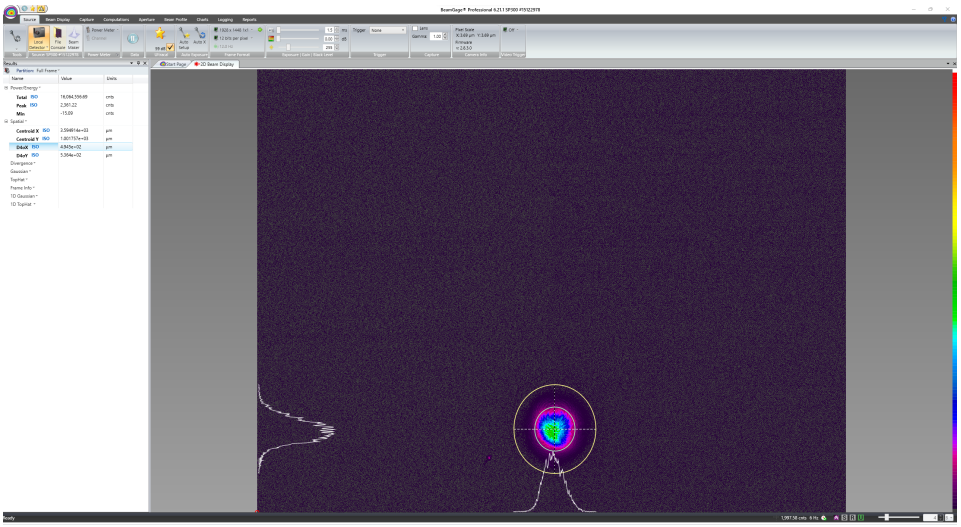

Figure A.9: Beam section captured at 145 mm from the focusing lens surface.

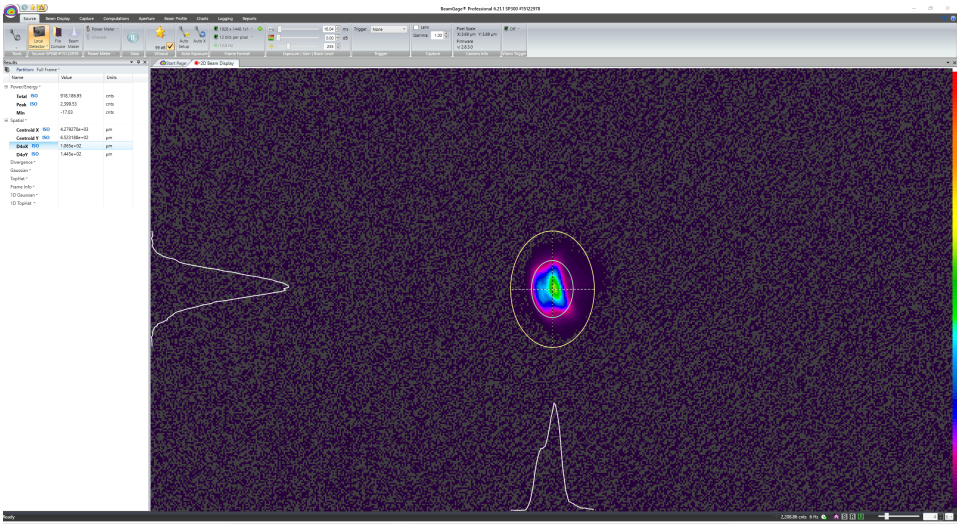

Figure A.10: Beam section captured at 155 mm from the focusing lens surface.

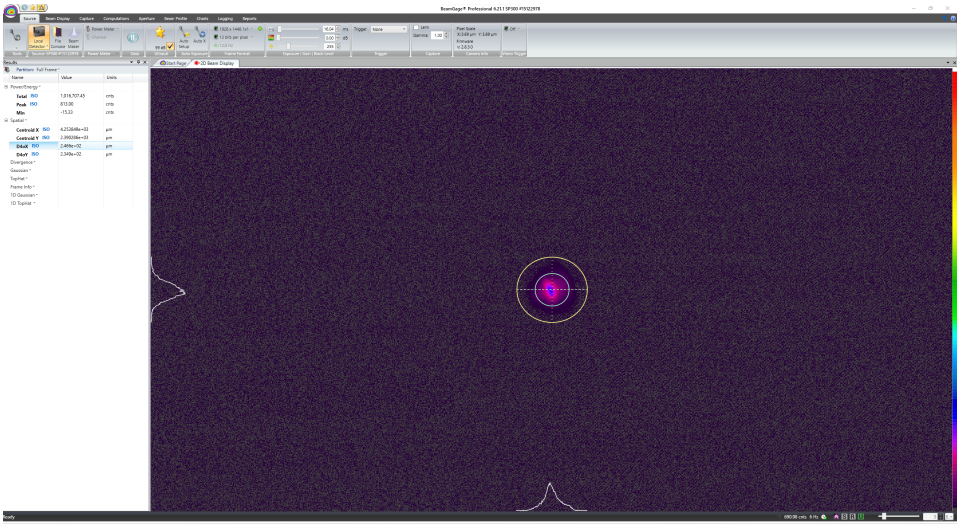

Figure A.11: Beam section captured at 165 mm from the focusing lens surface.

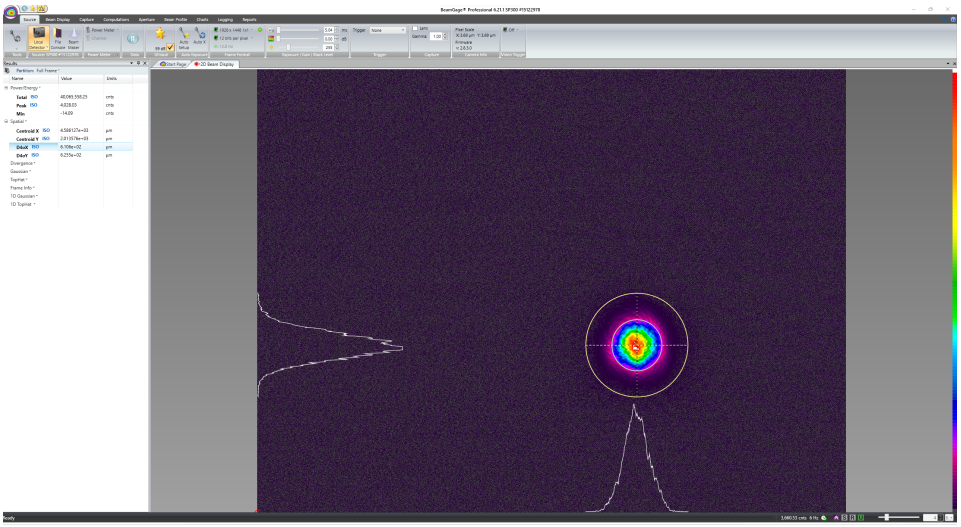

Figure A.12: Beam section captured at 175 mm from the focusing lens surface.

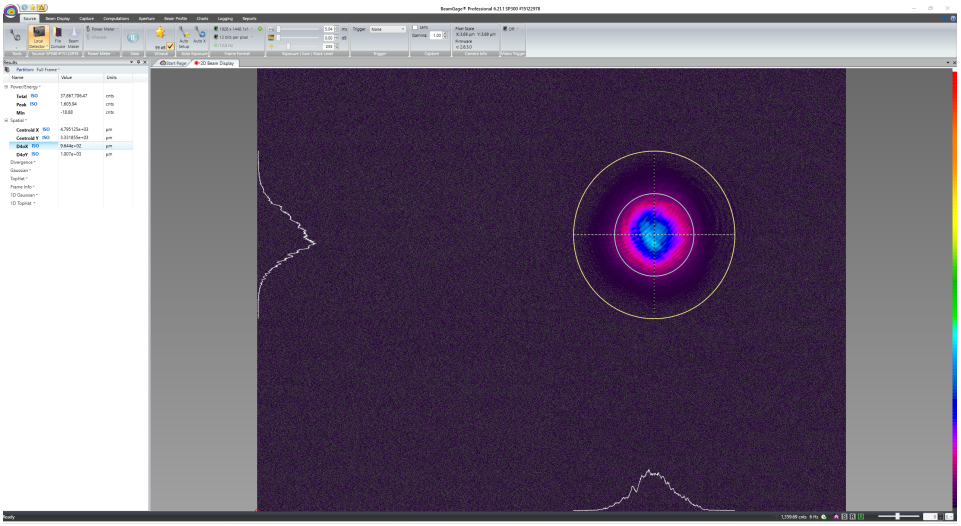

Figure A.13: Beam section captured at 185 mm from the focusing lens surface.

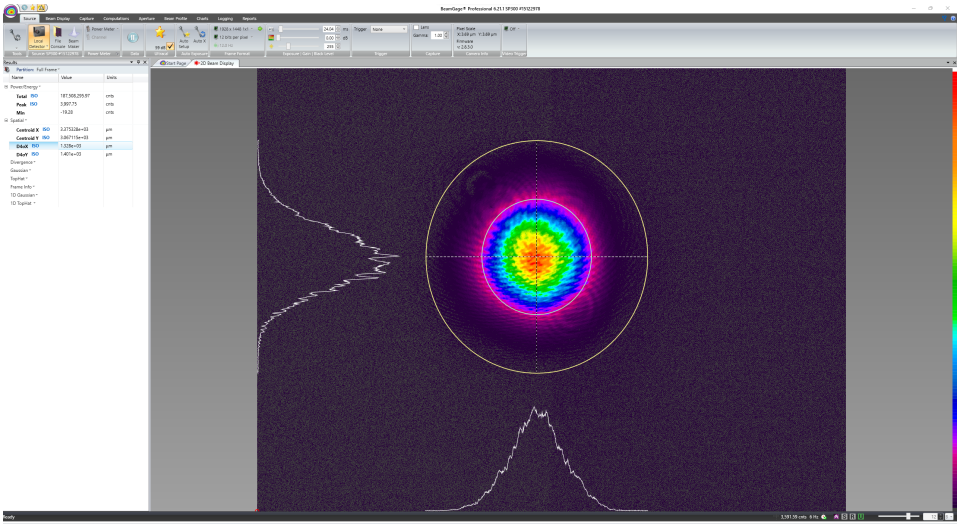

Figure A.14: Beam section captured at 195 mm from the focusing lens surface.

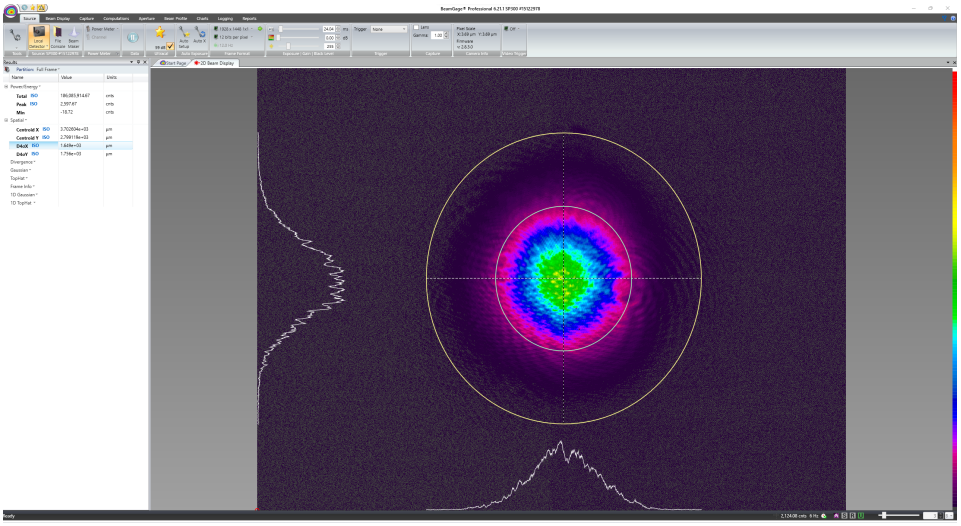

Figure A.15: Beam section captured at 205 mm from the focusing lens surface.

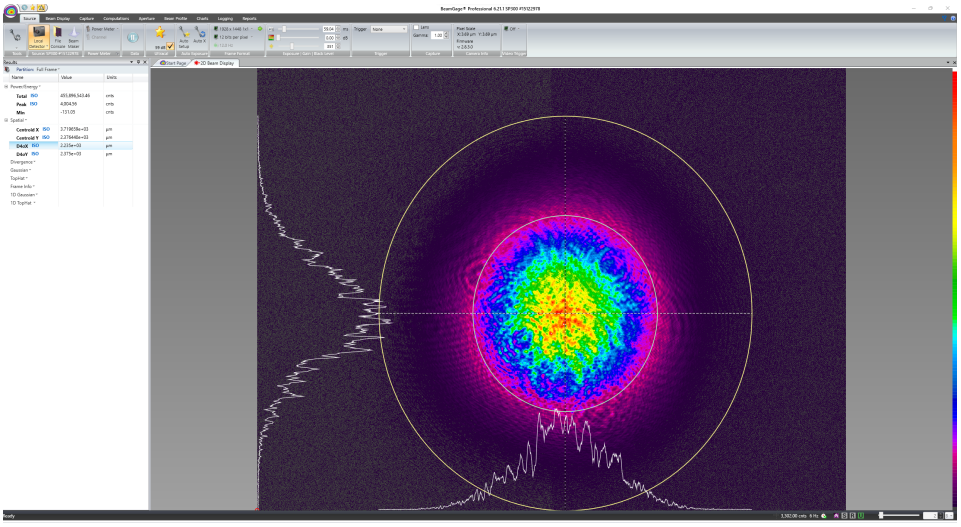

Figure A.16: Beam section captured at 220 mm from the focusing lens surface.

B

Contacts

If you are interested in more insights into this work, don’t hesitate to get in touch with me or my supervisors from TU Delft. I can provide you with a data package with the simulations, CAD files, and codes used for this thesis.